Multi-element Superconducting Nanowire Single Photon Detectors

by

Eric Dauler

Submitted to the
Department of Electrical Engineering and Computer Science
in partial fulfillment of the requirements for the degree of

Doctor of Philosophy in Electrical Engineering

at the

MASSACHUSETTS INSTITUTE OF TECHNOLOGY

February 2009

Author . . . . . .

Department of Electrical Engineering and Computer Science
January 30, 2009

Certified by. . . . . .

Karl K. Berggren
Associate Professor
Thesis Supervisor

Accepted by . . . . . .

Terry P. Orlando
Chairman, Department Committee on Graduate Students

Multi-element Superconducting Nanowire Single Photon Detectors

by

Eric Dauler

Submitted to the Department of Electrical Engineering and Computer Science
on January 30, 2009, in partial fulfillment of the requirements for the degree of
Doctor of Philosophy in Electrical Engineering

ABSTRACT

Single-photon-detector arrays can provide unparalleled performance and detailed information in applications that require precise timing and single photon sensitivity. Such arrays have been demonstrated using a number of single-photon-detector technologies, but the high performance of superconducting nanowire single photon detectors (SNSPDs) and the unavoidable overhead of cryogenic cooling make SNSPDs particularly likely to be used in applications that require detectors with the highest performance available. These applications are also the most likely to benefit from and fully utilize the large amount of information and performance advantages provided by a single-photon-detector array.

Although the performance advantages of individual superconducting nanowire single photon detectors (SNSPDs) have been investigated since their first demonstration in 2001, the advantages gained by building arrays of multiple SNSPDs may be even more unique among single photon detector technologies. First, the simplicity and nanoscale dimensions of these detectors make it possible to easily operate multiple elements and to closely space these elements such that the active area of an array is essentially identical to that of a single element. This ability to eliminate seam-loss between elements, as well as the performance advantages gained by using multiple smaller elements, makes the multi-element approach an attractive way to increase the general detector performance (detection efficiency and maximum counting rate) as well as to provide new capabilities (photon-number, spatial, and spectral resolution). Additionally, in contrast to semiconductor-based single-photon detectors, SNSPDs have a negligible probability of spontaneously emitting photons during the detection process, eliminating a potential source of crosstalk between array elements. However, the SNSPD can be susceptible to other forms of crosstalk, such as thermal or electromagnetic interactions between elements, so it was important to investigate the operation and limitations of multi-element SNSPDs. This thesis will introduce the concept of a multi-element SNSPD with a continuous active area and will investigate its performance advantages, its potential drawbacks and finally its application to intensity correlation measurements.

This work is sponsored by the United States Air Force under Contract #FA8721-05-C-0002. Opinions, interpretations, recommendations and conclusions are those of the authors and are not necessarily endorsed by the United States Government.

Thesis supervisor: Karl K. Berggren
Title: Associate Professor of Electrical Engineering and Computer Science

Acknowledgements

This thesis would not have been possible without the encouragement, advice and contributions of many people. I would like to express my deepest appreciation to:

Professor Karl Berggren, for always giving me the advice I needed, the opportunities that made graduate school so enjoyable and the encouragement to push myself in new directions

Professors Terry Orlando and Jeffrey Shapiro, for graciously agreeing to be on my thesis committee and teaching me much about superconductivity and quantum optics

Dr. Andrew (Jamie) Kerman, for always sharing his time, his useful insights, and his passion for science, which improved this research and my abilities as an experimentalist immeasurably

Joel Yang, for teaching me how to fabricate detectors while sharing his enthusiasm and gift for performing great research

Dr. Vikas Anant, Charles Herder, Xiaolong Hu and Professor Kristine Rosfjord, for their help in the lab and their useful insights

Dr. Richard Molnar and Dr. Bryan Robinson, for their contributions to this research, which saved me countless hours of work and permitted results that likely would not have been otherwise possible

Dr. Martin Stevens, Dr. Burm Baek, Dr. Sae Woo Nam, and Dr. Richard Mirin, for their enthusiastic help and extensive expertise making measurements with the detectors

Dr. Jeffrey Stern, for his encouragement and contributions pursuing detectors on alternative superconducting materials

Dr. Roy Bonduarant, Dr. Donald Boroson, Dr. Steven Constantine, Dr. Scott Hamilton and Dr. William Keicher, for their support and advice on my graduate studies

Dr. Alan Migdall, Professor Alexander Sergienko, and Dr. Franco Wong, for encouraging me to pursue experimental research

Jim Daley and Mark Mondol, for always being available to give useful advice and keep things working in the lab

Lisa Hill, Tiffany Kuhn, and Rick Magliocco for their help with wirebonding, purchase orders and circuit board design

The countless people whose contributions I have not acknowledged; I hope that some day I will also provide advice and tools that are so reliable and widespread that they similarly go without notice.

Finally, I will always be thankful for the loving support that Michelle Harman and my family have provided me during this wonderful experience and throughout my life.

Contents

List of Figures

List of Tables

Chapter 1

Introduction

Single photon detectors provide timing information about a digital event – the detection of single quantum of electromagnetic radiation. Superconducting nanowire single photon detectors (SNSPDs), also known as superconducting single photon detectors (SSPDs), [1-12] can provide very precise, ~30 ps, timing information [8, 13] for electromagnetic radiation over a wide range of frequencies – from ultraviolet to middle infrared [14-15]. With the exception of their small active area and cryogenic operating temperatures, SNSPDs are an ideal candidate for many applications [16-21].

This thesis will investigate operating multiple detector elements independently as a way to increase the active area while further improving the desirable performance features of SNSPDs. Multi-element SNSPDs can be used to detect simultaneous or nearly simultaneous photons while preserving the timing jitter, reset time and detection efficiency achieved with small-active-area SNSPDs [8]. The fast reset time and multiple detectors allow high counting rates and the ability to detect multiple photons with reduced dead-time effects. Finally, in addition to providing performance advantages, this work also investigates potential issues associated with operating arrays of SNSPDs, revealing that the detectors exhibit negligible interactions and are likely to perform well in a larger array format.

Before detailing how the multi-element SNSPD approach can improve the performance of the SNSPD, it is important to understand what limits the performance of single SNSPDs and what performance is important to potential applications. The remainder of this chapter will discuss these performance limitations, alternative photon-counting technologies and single-photon detector applications.

1.1 Superconducting Nanowire Single Photon Detector Overview

Superconducting nanowire single photon detectors were first demonstrated in 2000 by a collaboration between Moscow State Pedagogical University and the University of Rochester [1-2]. Although earlier work [22] had proposed a similar type of detector, the work in 2000 was the first to demonstrate a detector with discrete output pulses whose frequency was linearly proportional to the intensity of low-power optical radiation, confirming its single-photon sensitivity. The detector was composed of a NbN superconducting wire with small cross-sectional area (≤ 10 nm thick by ≤ 200 nm wide) attached to the end of a transmission line, as shown in Fig. 1.1. The wire was biased with a current approaching the level at which the charge carriers would switch from being in the superconducting state to the resistive (normal) state. This switching process was a digital event – current was either carried throughout the wire as a supercurrent, or the current density was too high in some region of the wire, making it energetically favorable for the superconducting charge carriers to become normal charge carriers across the full width, but a short length, of the nanowire. Consequently, photons absorbed in the wire could create a sufficient local excitation to reduce the fraction of superconducting charge carriers below the level required to carry the bias current as a supercurrent, switching a region of the nanowire normal. Once this region of the nanowire was in the resistive state, most of the bias current was shunted out of the highly resistive detector into the $50\,\Omega$ transmission line. The resistive state in the superconducting wire was unstable, as the energy dissipated in the wire was quickly extracted into the substrate, and the previously-resistive region in the wire quickly returned to the superconducting state, allowing the full bias current to again flow through the detector wire and automatically resetting the detector to be active for subsequent photon detection events. The simplicity of this detector structure, and the promising initial results, have subsequently encouraged and permitted many advances in the detector performance and a better understanding of the details of the detector operation.

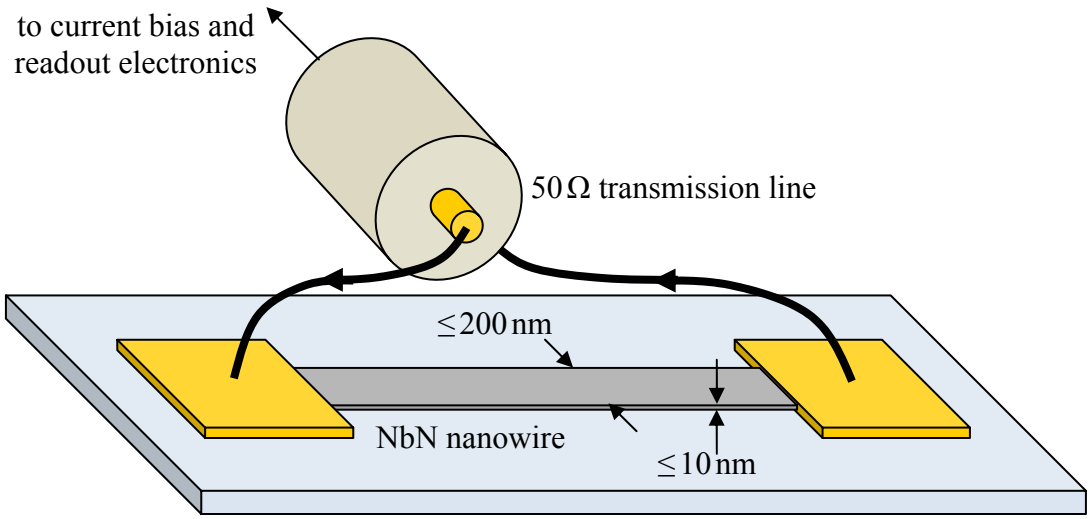

Figure 1.1: Schematic of the NbN nanowire used to detect single photons. When in the superconducting state, current flows through the nanowire, but during detection events, a resistive bridge forms across the nanowire with a sufficiently large resistance to shunt current out of the nanowire and into the 50 Ω transmission line.

1.2 Detection speed

The speed of a SNSPD can be described by its reset time (the time after a photon detection event until the detector is active for detecting a second photon) and by its timing jitter (the precision with which the timing of a detected photon is measured). The reset time is the primary limitation to the maximum counting rate of a SNSPD, although some other single photon detectors are limited by readout electronics, excessive heating or other effects. The SNSPD provides both low timing jitter and short reset times, making it desirable for many applications. This section will summarize ongoing work investigating both of these speed limitations in SNSPDs.

1.2.1 SNSPD reset time

The reset time of an SNSPD is limited by the time it takes for the full bias current to again flow as a supercurrent in the nanowire following a detection event. However, there are multiple steps to this reset process.

First, after current is diverted out of the nanowire, the resistive region must collapse so that the nanowire can return to the superconducting state. The process of expansion and contraction of the resistive state, and the corresponding amount of current flowing in the nanowire, requires considering both the electrical and thermal properties of the detector structure [23-24]. Before we address the reset time of the detector, we must first determine the conditions under which the detector will actually reset, which will occur when the resistive state in the wire is unstable at the desired bias current. The stability of the resistive state has recently been treated in detail [24], making it clear that the detector will only properly self-reset when the thermal time constants (dictated largely by the substrate and superconducting film, and less by the detector geometry) are sufficiently fast compared to the electric time constants. This constraint limits the extent to which the electrical time constant can be reduced to decrease the reset time of the detector.

Although the thermal time constants place a lower limit on the reset time, the electrical time constant for many SNSPDs prevents the reset time from reaching this limit. The electrical time constant, determined by the inductance of the nanowire and the load impedance to which it is connected, sets how long it takes the bias current to return to its full value. Since the detector relies critically on a high bias current to efficiently detect photons, the current recovery time dictates the reset time of the detector [6]. The inductance, which sets this time constant, is dominated by the kinetic inductance of the nanowire. The kinetic inductance is set by the energy stored in the ballistic motion of the superconducting charge carriers, not in a magnetic field as is the case for geometric inductance, and this kinetic inductance is proportional to the length of the nanowire divided by the cross-sectional area of the nanowire (independent of the actual wire path, unlike magnetic inductance). Thus, shorter wires (which necessarily cover a smaller area) have lower inductance and result in a faster reset time. Similarly, increasing the load impedance seen by the detector can decrease the electrical time constant [23].

Therefore, the reset time of the detectors is limited by a combination of the thermal and electrical time constants. Although there are several approaches to reducing the electrical time constants, the thermal constants place a lower limit on the reset time and can likely only be changed appreciably by changing the material properties. Although some SNSPD work has

investigated alternative substrates and film materials [9-12, 15, 25], producing faster SNSPDs by decreasing the thermal time constants has not been studied in detail. It is also not known if decreasing the thermal time constant will degrade the detector performance in other ways, such as dissipating the excitation energy before a normal region can fully develop, which would reduce the probability of detecting incident photons.

1.2.2 SNSPD timing jitter

Timing jitter in SNSPDs is not particularly well understood, but certainly depends on both the electrical time constants and the details of the readout electronics. Several groups have reported timing jitters of less than 30 ps [8, 26], with some reports of timing jitter ~ 18 ps [26], which have not been replicated. Timing jitter does not appear to be strongly related to the incident photon energy, the nanowire width (for wires < 100 nm in width) or the nanowire inductance (within the typical range 50 nH – 200 nH). The timing jitter is dependent on the bias current and the first-stage amplifier – high bias currents ($\geq 15\ \mu A$) close to the true critical current of the nanowire and low-noise, low-voltage-standing-wave ratio (VSWR), wideband (at least ~ 100 MHz – 3 GHz) amplifiers provide the lowest timing jitters. Artificially low timing jitter (~ 16 ps), and confirmation that the timing jitter is not dominated by the readout electronics, can be obtained by illuminating the nanowire with intense, short optical pulses that more quickly generate a resistive state in the nanowire (as observed in Ref. 27). Consequently, detector designs with wire widths and inductances in the ranges listed above are typically used, but further investigation is required to determine if timing jitter can be improved by any changes to the detector design and whether timing jitters < 25 ps can be obtained on a repeatable basis for single-photon detection.

1.3 Detection efficiency

Detection efficiency is a measurement of the probability that an incident photon results in an electrical output pulse. There is little ambiguity over what constitutes an electrical output pulse from a well-functioning SNSPD – the signal-to-noise ratio is sufficiently high ($\geq \sim 6$) for SNSPDs with critical currents of $\geq \sim 10\ \mu A$ that a wide range of output voltage threshold levels

correctly differentiate output pulses from voltage noise (noise counts are typically < 1% of the total counts, so they can be easily subtracted and often even neglected). However, the question of what constitutes "incident" photons is important. From a practical point of view, the detector should include the necessary coupling optics and the system detection efficiency, η_S, including losses introduced by this coupling should be measured. Using this definition, the performance of detectors with active areas too small for efficient coupling would be appropriately penalized. However, small SNSPD active areas and cryogenic cooling make achieving low loss when focusing light on the detector challenging, so these losses are often factored out in order to compare raw detector performance, particularly when comparing detectors with the same active area. The device detection efficiency, η_D, is therefore defined as $\eta_S \div \eta_C$, where η_C is the coupling efficiency. Finally, the device detection efficiency can be defined as $\eta_D = P_r \times A$, where P_r is the internal detection efficiency (the probability of resistive state formation) and A is the absorptance. Each of the three efficiencies (P_r, A, and η_C) will be described in this section in order to explain the various mechanisms by which photon counts are lost.

1.3.1 Internal detection efficiency

The internal detection efficiency remains a poorly understood aspect of SNSPDs. Although some simple models have been proposed for visualizing how the superconductivity is broken in SNSPDs [28-29], the proposed models do not quantitatively predict the wire geometry, photon wavelength or current dependencies observed experimentally. It is likely that an accurate model will require capturing both the way the photon-induced excitation evolves as well as how the coherent superconducting state reacts to the spatially and temporally varying density of superconducting charge carriers. Crude calculations suggest that the smooth but steep drop-off in detection efficiency as bias current is reduced may be due to shot noise in the spatial distribution of the excited (non-superconducting) electrons known as quasiparticles, as they diffuse and undergo scattering with other electrons and phonons. However, the superconducting state must be described by a single quantum mechanical wavefunction, limiting the ways in which regions of the wire become resistive and the supercurrent reacts to the excitation. The time-dependent Ginzburg-Landau equations, a set of non-linear, time-dependent differential

equations, can be used to calculate permissible superconducting states in narrow wires when the temperature of the superconductor is near its transition to a resistive metal [30]. However, the extent to which these equations are applicable to the case of interest for SNSPDs – when the superconducting gap is reduced, but non-zero, at low temperatures and high current densities – is not presently known. Finally, the issue of how to incorporate the photon-induced excitations, with potentially important spatial-temporal variations during the diffusion and scattering processes and statistical variations due to quantization of the charge carriers, is another difficult problem.

Although a theoretical model for the resistive state formation in SNSPDs is not available, several important aspects of this contribution to the detection efficiency can be investigated experimentally. As expected, a high bias current is critical to achieving a high internal detection efficiency [1-2, 8, 14, 31-33], particularly at long wavelengths (lower energy photons) [14]. The maximum achievable internal detection efficiency increases at lower temperatures [31], likely due in large part to the increased critical current in the nanowires. The critical current can typically increase by $\sim 50\%$ as the temperature of the detector is reduced from $4.2\,\mathrm{K}$ to $< 2.5\,\mathrm{K}$, but saturates (along with the detection efficiency) at lower temperatures [31]. The internal detection efficiency as a function of increasing bias current is essentially zero at low currents, increases exponentially and, for high energy photons in optimal SNSPDs, smoothly reaches a plateau at high bias currents (see, for example, Fig. 1.2(a)). The shape of this detection efficiency versus current curve depends on the photon energy, the nanowire width, the nanowire thickness and other parameters, but is qualitatively similar for all reported SNSPDs. The curve is shifted towards lower bias currents and typically sharper (steeper exponential region and higher curvature in the transition to the saturated efficiency) for higher energy photons and narrower or thinner wires. Wires with widths $\leq 100\,\mathrm{nm}$ and thickness $\sim 5\,\mathrm{nm}$ result in the highest internal detection efficiencies. For visible-wavelength photons [31- 32], the internal detection efficiency as a function of bias current saturates at high bias currents for the best devices operated at low ($< 2.5\,\mathrm{K}$) temperatures, likely at a value close to 100%. The detection efficiency versus bias current curve for longer wavelength photons is less sharp and shifted toward lower detection efficiencies and higher bias currents. The internal detection efficiency near the critical

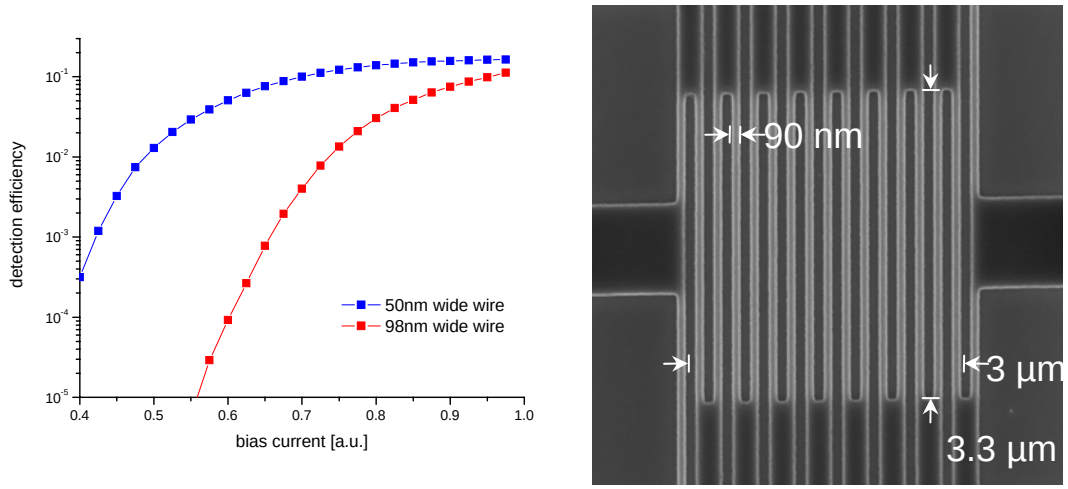

(a) (b)

Figure 1.2: (a) Detection efficiency versus normalized bias current for wire widths of 50 nm (blue) and 98 nm (red). (b) Scanning-electron micrograph of a nanowire pattern with 90 nm width covering an active area of 3 µm by 3.3 µm. The micrograph is actually an image of the electron-beam resist before etching the underlying superconducting film. After etching, the superconducting film will remain only in areas covered by resist – from the dark square on the left, up through the meander path outlined by the brightly-colored edges of the resist , and finally to the dark square on the right.

current is reduced slightly at short-wave infrared wavelengths and by orders of magnitude at middle-infrared wavelengths relative to the efficiencies for visible-wavelength photons. However, even this small sensitivity to middle-infrared photons makes shielding the detector from blackbody radiation (using a cooled material that is optically opaque in the middle-infrared) critically important to achieving low noise counts. Noise count rates in the low-kHz range have been observed for shielded SNSPDs with efficient optical coupling from a fiber.

While the photon wavelength and the average nanowire cross-sectional area affect the shape of the internal detection efficiency versus bias current curve, the critical current achievable in each detector limits its operating range. A defect that limits the critical current of a nanowire will similarly limit the range of detection efficiencies that can be accessed [33]. Unfortunately, such defects are common in SNSPDs, and their typically high density have made fabricating large area SNSPDs challenging. There have been no reports of high yield (> 10% of detectors exhibiting > 50% internal detection efficiencies at 1550 nm) for detectors 10 µm × 10 µm or larger, until recent developments described in this thesis. These defects, known as constrictions,

have been studied and can be identified through electrical [33] and optical illumination of operating SNSPDs [34]. However, the cryogenic temperature and serial testing required for either approach to identify constricted detectors, and the exponentially decreasing probability of defect-free detectors with increasing detector area, have restricted demonstrated high-efficiency SNSPDs to small active areas. Although a small constriction may affect the internal detection efficiency of SNSPDs negligibly at visible wavelengths, due to the saturated efficiency as a function of current, the internal detection efficiency is degraded more significantly for longer wavelengths. The defect densities typically seen in detectors fabricated in most of this thesis, as well as the densities that reports in the literature suggest are seen by others in the field, dominate variables such as the wire cross-sectional area in determining individual detector efficiencies. Consequently, reducing the defect density has been one of the most important steps to increasing SNSPD's internal detection efficiency.

1.3.2 SNSPD Absorptance

Absorption in SNSPDs has previously been treated in detail [35-36]. In order to fabricate a detector with a reasonable active area, the nanowire is designed to cover a meander (boustrophedonic) pattern, as shown in Fig. 1.2(b). The nanoscale dimensions of the superconducting wires require careful calculation of the electromagnetic interactions and result in a polarization dependent absorptance in the wires. The large index mismatch between air or the substrate and the NbN, along with the short optical path through the ~ 5 nm thick NbN wire, result in light being reflected and transmitted by the SNSPD. The light lost to reflection and transmission can be reduced by a factor of > 2 [36] by fabricating a $\sim \lambda/4$ dielectric spacer and metal reflector on top of the SNSPD and an anti-reflection (AR) coating on the back of the substrate [7]. In this way, no light is transmitted through the detector and partial destructive interference is achieved for the field reflecting off the detector. With proper choice of substrate, NbN film thickness and fill factor, absorption approaching 100% is possible. Device detection efficiencies, $\eta_D = P_r \times A$, as high as 57% have been published [7] and over 70% have been measured on the best detectors at 1550 nm wavelength with such a cavity and AR coating, indicating that both high absorption and high internal detection efficiency can be achieved. It is

important to note that the absorption in the SNSPD would be reduced by a factor of ~2 without the optical cavity, and by an additional factor of ~2 with improperly polarized light, so the absorption must be carefully considered in order to achieve a high detection efficiency.

1.3.3 Coupling efficiency

Finally, the coupling efficiency describes the fraction of the input light that is incident on the active area of the detector. The input to the detector system is typically a single-mode optical fiber, so the loss mechanisms include optical losses in this fiber and any lenses (due to absorption in the optics or the finite size of the optics) and light incident outside the active area of the detector (due to misalignment, vibrations, or the tails of the optical beam).

The approach most often taken to efficiently couple light to an SNSPD is to place a single-mode optical fiber in close proximity or contact with the surface of the detector [13, 19]. Although this approach is simple (relatively good alignment can be achieved at room-temperature and maintained during cooling), this method does not permit illumination through the substrate because the several-hundred-micrometer substrate thickness is large compared to the several-tens-of-micrometer depth of focus typical of the output from a fiber. Consequently, direct fiber coupling is not compatible with a cavity structure fabricated on top of the detector to increase absorption. Furthermore, misalignment can often be a problem, particularly in cases when the detector diameter and the mode-field diameter in the fiber are both ~10 μm.

A second approach that overcomes the drawbacks of direct fiber coupling is to use a lens assembly on the end of a fiber, which can be positioned at cryogenic temperatures [37-38]. The lens assembly can refocus the light at a working distance longer than the substrate thickness, allowing the light to be coupled through the substrate and thereby permitting the use of a cavity structure fabricated on top of the detector. The lens assembly can also be designed to focus the light to a spot size smaller than the mode-field diameter of the fiber, permitting a very high fraction of the light to be coupled onto the detector. Finally, having control over the position of the lens assembly at cryogenic temperatures allows it to be actively aligned to the detector using the detector count rate as feedback. Although this approach is more complex and can be more

susceptible to vibrations, depending on the design of the positioning mechanism, its potential for consistently low coupling loss and compatibility with cavity-integrated detectors makes it better for achieving the highest possible detection efficiencies.

1.4 Alternative single-photon detector technologies

In addition to the SNSPD, there are many other types of single-photon detectors. It is important to understand the advantages and drawbacks of the competing technologies to determine what unique capabilities the SNSPD can provide. This understanding is critical to improving the SNSPD in ways that will be useful to potential applications.

Single-photon detector technologies can generally be categorized by the medium that amplifies the photon excitation before the electrical readout, typically an electron multiplier, a semiconductor or a superconductor. The advantages and drawbacks of these general technology categories will be discussed briefly in this section in order to place the SNSPD in the proper context, particularly in terms of potential applications.

Electron multiplier devices, such as photo-multiplier tubes (PMTs) [39] and microchannel plate (MCP) detectors [40], are very mature technologies used in a wide range of applications. They are available with >10 mm diameter active areas, <100 Hz dark count rates, and <100 ps timing jitter [41] in relatively compact packages that include the necessary high-voltage supply. Their low multiplication noise allows them to be operated in a linear-mode where they can resolve the number of simultaneously incident photons, and their short pulse width and fast reset times permit distinguishing photons separated by nanoseconds in time. Maximum count rates from PMTs are typically a few-MHz or tens-of-MHz because the output current must be limited. Drawbacks to PMT and MCP detectors include their relatively low detection efficiency, which is typically 10 – 30%, and their insensitivity to infrared photons (typical cut-off wavelengths are 800 nm – 900 nm). Recently, advances have been made in integrating short-wave-infrared-sensitive photocathodes [42] and developing infrared-sensitive

hybrid PMTs [43], but these detectors have high dark count rates, low detection efficiencies, typically require liquid nitrogen for operation and are less mature than standard PMTs

Semiconductor-based single photon detectors, most notably the Geiger-mode avalanche photodiode (GM-APD or SPAD – single-photon avalanche diode) have also matured significantly in recent years [44-48]. Compared to PMTs, GM-APD active areas are typically smaller (tens to hundreds of micrometers) with timing jitters of a few tens of picoseconds [44] to hundreds of picoseconds [45], depending on the diode and readout design. Although silicon-based GM-APDs can have 60-70% peak detection efficiencies, <25 Hz dark counts, 40 ns reset times and several-MHz count rates, their sensitivity falls off dramatically at wavelengths longer than ~ 900 nm, with essentially zero detection efficiency at wavelengths beyond 1.1 μm [45]. The performance of InGaAsP-based APDs, and other short-wave and middle infrared sensitive APDs, is considerably worse, with 50% or lower detection efficiencies, kHz-rate dark counts, and microsecond reset times [46-47]. With the exception of the best small-area InGaAsP GM-APDs, most infrared-sensitive GM-APDs must be operated in gated-mode, where they are only active for short periods of time, because of the combination of long reset times and high noise counts. Relatively compact GM-APDs packages and readout electronics are available for both visible and infrared wavelengths with compact thermoelectric cooling. In addition to GM-APDs, other semiconductor-based single photon detectors, such as visible light photon counters (VLPCs) [48], have also been demonstrated that excel in specific performance areas (high detection efficiency and photon-number-resolution in the case of the VLPC).

Finally, superconducting single photon detectors, such as transition-edge sensors [49], tunnel junction detectors [50] and kinetic inductance detectors [51] have historically been desirable because of their high sensitivity over a very wide range of wavelengths (from gamma rays to infrared wavelengths with single-photon sensitivity) and their low noise. For example, transition-edge sensors with $>90\%$ detection efficiency at 1550 nm wavelength and no known intrinsic source of noise have been reported [52]. The SNSPD, however, is the first superconducting detector to achieve <100 ps timing jitter and to permit tens to hundreds of MHz-class counting rates. All of the superconducting detectors must be operated cryogenically

(generally at liquid helium or colder temperatures), limiting the total package size and restricting their use to relatively large-scale applications.

1.5 SNSPD applications

Now that the performance of the SNSPD and alternative single-photon detector technologies have been reviewed, it is useful to consider what applications may benefit from using an SNSPD. The key strength of the SNSPD is its speed, both its timing jitter and maximum counting rate, which are competitive or slightly exceed the best available for any single-photon detector technology. However, the cryogenically cooling requirements, small active area and low level of maturity put the SNSPD at a disadvantage. These disadvantages are most likely to be overlooked for applications at short-wave infrared wavelengths (~ 1 μm – 2 μm), where competing technologies are less mature and lower performance. The SNSPD can significantly outperform GM-APDs at short-wave infrared wavelengths in terms of maximum counting rate, timing jitter and, potentially, dark count rate. Compared to short-wave-infrared PMTs, the SNSPD can have significantly higher detection efficiency and lower dark counts. Consequently, the SNSPD is likely to be most attractive to applications requiring high performance in a number of areas including speed, high detection efficiency and low noise at short-wave infrared wavelengths.

Fortunately, there are many applications that work at short-wave infrared wavelengths, can benefit from the high performance of SNSPDs and are tolerant of its shortcomings. In fact, SNSPDs have already been demonstrated in many of these applications. The first application in which SNSPDs were commercialized was a tool that aids in identifying circuit design failures by detecting infrared photons from switching transistors [16]. Another important application in which SNSPDs have been used for proof-of-principle experiments [17] is interplanetary optical communication, which benefits from their high detection efficiency, low timing jitter and high count rate at 1.55 μm wavelength. Research applications such as quantum optics, including quantum key distribution [18], intensity correlation measurements [19] and more fundamental experiments [20], have readily adopted the SNSPD. The low SNSPD timing jitter and sensitivity

at eye-safe and telecom infrared wavelengths makes SNSPDs a potential candidate for laser ranging [21], particularly if reasonable size arrays were viable, or for optical time-domain reflectometry. Finally, near-IR fluorescence correlation spectroscopy [53] and fluorescence lifetime measurements [54] as well as astronomical observations [55] are also potential applications.

1.6 Summary

The SNSPD has advanced from initial demonstrations [1-2] to a very competitive photon counting technology in a short period of time. Although all of the details of its operation cannot yet be quantitatively modeled, many aspects can and most details of its operation have been studied experimentally. From an application perspective, achieving high system detection efficiency at short-wave infrared wavelengths, while maintaining the low timing jitter and high counting rate that make the technology attractive, is the most important improvement required.

Although this goal of high system efficiency was the initial motivation, and was successfully addressed, in this work, the multi-element approach also offers many other advantages that will be discussed throughout this thesis. The remainder of this thesis describes the multi-element SNSPD concept, fabrication and experimental results. Chapter 2 introduces the multi-element concept in detail, comparing it to other single-photon detector arrays and other approaches for improving the SNSPD performance. Chapter 3 describes the SNSPD fabrication, focusing on a general overview of the process which had been previously developed as well as presenting some specific challenges and solutions addressed in this research. Chapter 4 presents work on a two-element SNSPD used to verify the multi-element concept and better understand its limitations. Chapter 5 discusses the primary accomplishment of this work, a 4-element SNSPD with 46% system detection efficiency that can resolve photon number while precisely timing individual photons. Chapter 6 presents a new way of making intensity correlation measurements that takes advantage of the unique characteristics of the SNSPD and also permits measuring the crosstalk between detector elements, found to be below 0.00001%. Finally, Chapter 7 provides a summary of this work and a brief overview of potential future directions.

Chapter 2

Multi-element SNSPD Concept

Many single-photon detector technologies have been implemented in array formats, including Geiger-mode avalanche photodiodes [56-57], microchannel plates [58-59], and transition edge sensors [60-61]. Linear arrays can be used to extract spectral information using a diffraction grating or prism, and two-dimension arrays are often used to extract spatial information while maintaining the temporal information and single-photon sensitivity that the individual single photon detectors provide. Alternatively, by spreading a single optical mode across multiple single-photon detectors, photon-number-resolution [62] and higher counting rates [63] can be achieved. The multi-element SNSPD concept takes this one step further: by subdividing what would be a single detector into multiple independent elements with the same total area and optical cross-section, the performance is improved both because it has multiple elements and because of the elements smaller size, without introducing additional optical loss in coupling to the separate detector elements. This chapter provides a brief overview of single-photon detector arrays, the potential advantages and implementations of multi-element SNSPDs and alternative approaches to improving the performance of SNSPDs.

2.1 Single-photon detector arrays

There are several requirements for making a compact single-photon detector array. First, it must be possible to fabricate the desired number of detector elements, as well as the necessary biasing and readout electronics, in a reasonable amount of space. For many detector technologies, it is the size of the biasing and readout circuits that are the limiting factor, and these often must be redesigned in an integrated or hybrid circuit format in order to be sufficiently compact, particularly when a large number of detector elements are required. Furthermore, it is often not sufficient to simply shrink down the size of independent bias and readout circuits, with separate

wires addressing each detector element. Instead, some form of multiplexing is often required for reducing the number of wires necessary to address all of the detector elements. Finally, when operated simultaneously, the detector elements must not interact in ways that affect one another too strongly. This can be particularly problematic when detection events involve large voltage swings or the re-emission of photons, and may also limit how closely the detector elements can be spaced. Despite these challenging requirements, many single-photon detector technologies have been demonstrated or feasible proposals have been made for their integration in array formats.

Most single-photon detector technologies are sufficiently compact for array integration. Semiconducting and superconducting detectors are typically small and are fabricated using planar lithography processes in which fabricating arrays of devices is routine. Furthermore, microchannel plates, which consist of a large array of small channels in which electron multiplication occurs, can be combined with a suitable array of electron detectors (after the multiplication process) to form a compact array of photomultiplier tubes.

The types of readout and multiplexing vary widely between the various single-photon detector technologies. Complementary metal-oxide-semiconductor (CMOS) integrated circuits are typically used to perform the necessary biasing, reset and readout functionality of semiconductor-based Geiger-mode avalanche photodiode arrays [56-57] and microchannel-plate-based photon counting arrays [59], with various time-multiplexing approaches used to reduce the number of required readout lines. Both time and frequency multiplexed readout based on superconducting quantum interference devices have been demonstrated with arrays of transition-edge sensors [60-61, 64].

Finally, interactions between detector elements are a common problem for single-photon detector arrays. Geiger-mode avalanche photodiodes emit photons during the detection process that can subsequently be detected by neighboring pixels [56-57]. This level of crosstalk from photon emission can be reduced by minimizing the change flowing through the diode during an avalanche event and by obstructing the optical path between detectors (by isolating the diodes as mesa structures, etching trenches in the substrate or adding material layers to partially filter the

emitted photons spectrally), but crosstalk can be problematic for some applications. Similarly, electrical crosstalk, due to the high voltages and large gains present in microchannel plate detectors, can cause undesirable interactions [65]. Superconducting detectors can also be susceptible to electrical, as well as thermal, crosstalk [66-67].

Despite the challenges associated with reading out and operating single-photon-detector arrays, significant progress has been made in demonstrating and using such arrays in important applications. Photon-counting arrays have been used for astronomy [55], laser ranging [68], fluorescence correlation spectroscopy [69] and other applications. Small "arrays" consisting of four elements have been demonstrated for SNSPDs in this work, and have been applied to high-sensitivity optical communications [70] and intensity correlation measurements [71]. Larger SNSPD arrays, likely with a time multiplexed output due to the large bandwidth required to preserve the timing information, would permit SNSPDs to benefit a wider range of applications. Finally, those applications that make use of high-performance photon-counting arrays already have significant electronic requirements imposed by the data collection and processing, making the overhead required to cryogenically cool SNSPDs less likely to be a major impediment to their adoption.

2.2 Multi-element SNSPD advantages and implementations

Although photon counters provide the ultimate sensitivity in optical detection, many applications require additional information about the state of the optical radiation, including spatial, spectral and photon-number resolution that most photon counters do not provide. One of two approaches can be taken in order to obtain this information: the optical signal can be spread across a large array of single-photon detectors, so that the information is extracted from the number and position of the detectors that fire, or a photon counting technology can be selected that allows the information to be extracted from a single detector's output signal. The spatial and spectral resolution from a large array can be much better than from a single detector because the resolution of the array is limited only by the number of elements and the optics used to couple the light, not by noise in the detection process or analog readout electronics. Furthermore, an

array is more flexible than a single detector, because the same array and readout electronics can be combined with any combination of: (1) imaging optics that provide spatial information, (2) a diffraction grating that provides spectral information, or (3) an optic that spreads the beam across multiple elements to provide photon number resolution and higher counting rates. Finally, the array can be composed of detectors that do not individually resolve information about all of these properties of light, which allows a detector technology to instead be selected to provide high-detection efficiency, low dark count rate, or excellent timing resolution.

However, there are also disadvantages to using arrays of photon counting detectors. First, there is typically an optical coupling loss associated with a microlens array or non-unity fill factor. Second, some photon counters require a significant amount of discrete electronics or cannot be fabricated on a single wafer, so arrays may be expensive or bulky. Third, many problems faced by single detectors, such as fabrication yield and dark counts, are multiplied when arrays of photon counters are needed. Finally, there are additional challenges that arise in arrays, such as crosstalk between elements and providing readout for each detector in a large array.

The multi-element SNSPD approach proposed here alleviates many of these disadvantages, particularly when the input optics are configured so that the multi-element SNSPD provides photon-number resolution and higher counting rates. The first disadvantage of photon counting arrays discussed above, the additional optical loss associated with coupling light into the array versus a single detector, is eliminated by the multi-element SNSPD design. The multi-element SNSPD differs from conventional arrays of photon counters because there are no gaps between elements: the elements are lithographically patterned such that the combined active area is indistinguishable optically from that of a single-element detector (Fig. 2.1). This uniformity eliminates the coupling loss associated with a microlens array or non-unity fill factor. Second, a packaged multi-element SNSPD is unlikely to be large or expensive because hundreds of SNSPDs can be fabricated on a single chip and the electronics required to operate a SNSPD are simple (SNSPDs do not require an external reset circuit). Third, although fabrication yield and the scaling of dark counts will need to be addressed, the multi-element SNSPD design

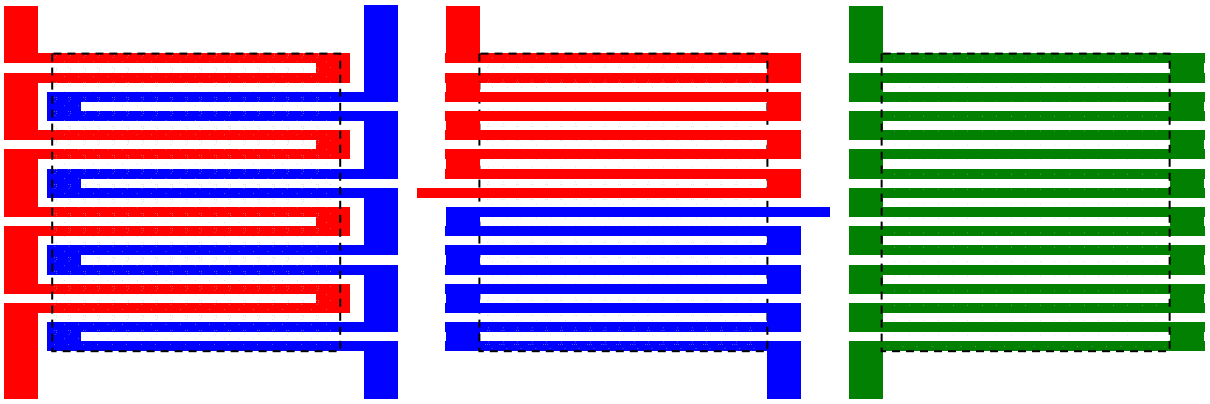

(a) (b) (c)

Figure 2.1: Schematic of (a) an interleaved two-element SNSPD, (b) a linear array two-element SNSPD and (c) a single-element SNSPD all with essentially the same active area. The coloring indicates the features corresponding to the (blue) first element, the (red) second element, the (green) single element and the (gray with dashed outline) detector active area.

provides a unique opportunity to alleviate these challenges. If the optical beam is to be spread across multiple elements to provide higher counting rates or photon-number resolution, the multi-element SNSPD elements can be fabricated with active areas smaller than a focused optical spot. Using smaller, contiguous elements that are illuminated by a single, tightly focused beam provides several advantages compared to larger, isolated elements. Smaller SNSPDs can have: (1) faster reset times, because this time is limited primarily by the kinetic inductance of the nanowire [6], (2) higher fabrication yields, because the yield is largely limited by constrictions [33], and (3) can potentially have lower dark count rates, because noise counts often occur primarily at the narrowest point in the wire [72], and noise counts from constricted elements could be drastically reduced through small reductions in the bias current, without affecting the detection efficiency of un-constricted elements that are independently biased. The final drawbacks to photon counting arrays mentioned above are the challenges associated with scaling to large array sizes and the potential for interactions between array elements. These drawbacks and the advantages of the multi-element SNSPD design are addressed in the remainder of this thesis.

Before quantifying the performance advantages the multi-element SNSPD approach provides, it is useful to consider how the elements should be arranged spatially. The appropriate

arrangement depends most critically on whether the light should be spread evenly across multiple elements or intentionally directed toward a specific element. When the goal of having multiple elements is to resolve the number of simultaneously incident photons or to count photons at a higher rate with reduced dead-time effects, the detector elements should be arranged so that the light is spread evenly across all of the elements. In this case, the ideal arrangement is to interleave the elements so that the alignment to the detector will not strongly influence the splitting ratio, as shown in Fig. 2.1(a). Alternatively, when multiple elements are used such that the element in which a count is measured provides additional information about the photon, then spatially-distinct elements are required (Fig. 2.1(b)). A linear array of elements may be sufficient for information that is one-dimensional, such as the wavelength of the incident photons, while a two-dimensional array of detectors is preferable for other applications, such as extracting spatial information or imaging. Both interleaved and linear-array arrangements will be demonstrated in this thesis.

2.3 SNSPD design changes: alternatives to arrays for improved performance

Finally, it is worthwhile to consider whether there are alternatives to the multi-element approach that allow SNSPDs to achieve similar performance improvements. Other than arrays, there have been no proposed or demonstrated approaches for using SNSPDs to achieve spatial resolution or spectral sensitivity, with the exception of an approach that may achieve limited spectral sensitivity at the expense of detection efficiency [73]. There have, however, been approaches for increasing the maximum counting rate and achieving photon-number-resolution that do not rely on using multiple, independent elements.

The maximum counting rate is limited by the current-recovery time, which is set by the load impedance and the nanowire inductance. As previously mentioned in section 1.2.1, increasing the load impedance does reduce the current recovery time and should increase the maximum counting rate, although the amount of speed-up is limited by the requirement to

maintain the detector's self-resetting property [23-24]. If speeding up large area SNSPDs to have a 5 - 10 nanosecond reset time is the only performance improvement sought, adding a series resistor is a simple and elegant approach. Furthermore, series resistors can also be combined with the multi-element approach to speed-up large area elements in a multi-element SNSPDs.

In addition to increasing the load impedance, the maximum counting rate can also be increased by reducing the inductance of the nanowire. The length, width and thickness of the nanowire cannot be changed without altering the active area or the internal detection efficiency of the SNSPD, so an alternative approach to reducing the inductance must be taken to maintain high detection efficiency. One approach is to put multiple nanowires in parallel electrically. If the nanowires are connected in parallel without a resistive element between them, current division between the nanowires is set by maintaining constant magnetic flux through the superconducting loops. This prevents proper biasing of the parallel nanowires when only the segment in which a photon is absorbed switches normal, because once current is diverted from that segment into the transmission line, that segment returns to the superconducting state forming a loop with parallel wires that prevents the current from equalizing in the various segments. This can be avoided by driving all of the parallel segments normal at the same time, but this requires adding additional inductance in series with the detector so that the current is diverted from the segment with the photon absorption into the parallel segments. This approach has been demonstrated using a discrete series inductor [74] and by dividing the detector area into a series of sections with short nanowire segments in parallel (in this way, each section of parallel nanowires is in series with a large number of similar sections that provide the necessary series inductance) [75]. It is not clear that the former idea [74] provides any increase in maximum counting rate, and although the second idea [75] could potentially be faster, the demonstrated detectors often oscillated. Such oscillation is expected to occur for both designs when the bias current is too low for the diverted current to drive the parallel segments normal, which can potentially be all accessible currents for constricted detectors. This parallel nanowire approach does result in larger output signals when all of the parallel segments switch in unison, but relaxing the amplifier requirements appears to be one of the only advantages of the design, while many drawbacks exist.

A better approach to putting multiple nanowires in parallel is to put a non-superconducting element in series with each segment, before the parallel connection. This has been demonstrated using both resistors [76] and high-electron-mobility transistors (HEMTs) [77]. Using resistors, the resistance values set the current splitting ratio between the detectors; using HEMTs, the bias currents can be set completely independently. The maximum counting rate is improved using either approach, and in the case of the multi-element approach, in three ways: (1) increased load impedance (either necessarily because of the resistor required in the first approach, or by choice with the HEMT or multi-element approaches), (2) the lower inductance per segment, due to the shorter length of each segment relative to the total detector active area (all three approaches divide the active area into multiple shorter nanowires) and (3) the multiple nanowires counting in parallel. Similarly, all three approaches provide a way of achieving photon-number-resolution. In the case of the resistor or HEMT approach to analog adding the nanowire outputs, the photon-number information has been extracted by measuring the pulse height, while the number of independent elements that fire provides the photon-number information in the case of the multi-element detector.

The critical difference between the three approaches (resistors, HEMTs, and multi-elements) is the degree to which the detectors are independent. The first such independence issue is the degree to which the bias currents can be set, and reset, without influencing the adjacent detectors. The resistor approach provides little flexibility in this regard – the resistor values would need to be individually trimmed to set the ratio of bias currents flowing in the parallel nanowires and some current from a switching nanowire will always flow into neighboring nanowires. This issue of current flow into neighboring wires is further complicated by the requirement that the nanowires self-reset [23-24], which places constraints on how low inductance and how high resistance the segments can be (creating a tradeoff between detector speed and isolation of the current between detectors). Additionally, when multiple photons closely-spaced in time are detected in different wires, more current is diverted into the parallel segments than if just a single photon were detected. This makes the detection efficiency non-linear with photon-number and creates a tradeoff in terms of bias current: at low currents, the single photon detection probability is reduced, but at high currents, the maximum number of

simultaneous photons that can be detected is limited (otherwise the large diverted current will drive all of the parallel segments normal). Using the HEMT or multi-element approach eliminates these problems: the bias current in each nanowire is set and recovers independently.

The second independence issue is one of readout. Both the resistor and HEMT approaches combine the output from the nanowire segments into a single analog output. This makes distinguishing closely spaced detection events a difficult analog readout problem, particularly when accurate timing of the photons is required or the photons are not incident in well-separated ($> \sim 10$ ns), short (< 1 ns) optical pulses. There are no commercially available circuits for performing the desired functions, like resolving photon number from the pulse height or counting / timing the incident photons from the analog addition of many overlapping pulses, at the speeds required to improve the performance of the SNSPD. Alternatively, the multi-element approach adds complexity in terms of more independent detector readouts, but the actual readout elements are much simpler because they are digital components – a comparator and a digital timing circuit. Furthermore, the complexity of independent readouts for multiple elements is very manageable for small numbers of elements using discrete readout of each element, and for large numbers of elements, a readout-integrated circuit would solve the problem (and could be a purely digital circuit). This makes the multi-element approach more attractive as well.

Finally, only the multi-element approach provides information about which detector element fired. This information is important for studying potential interactions that would occur in a large array of SNSPDs. It also permits intensity correlation measurements or demonstrations of limited spectral or spatial resolution, such as a quad-cell. Finally, there are no advantages, other than fewer output lines, provided by any other approach that are not met or exceeded by the multi-element approach. Consequently, from both a scientific point of view, in terms of studying the physical interactions between superconducting nanowires, and an application perspective, in terms of performance and real-world utility, multi-element SNSPDs are well worth investigating.

Chapter 3

Fabrication of Multi-element SNSPDs

Although multi-element SNSPDs require a different layout of contact pads and superconducting nanowires than individual SNSPDs, the same fabrication process was used to make both types of detectors. Several processes have been previously developed for fabricating SNSPDs [1, 4-5, 10, 78], including a process developed by Joel K. W. Yang at the Massachusetts Institute of Technology [5, 78], with modifications introduced by Kristine M. Rosfjord et al. [7] and Vikas Anant [36], that will be used throughout this work. Although relatively few additional modifications to the process were required, many subtleties in the fabrication process were discovered by repeating the process many times. New problems can appear even in well-tested processes when chemicals, storage containers, wafers and process tools change in unexpected ways or unintentional consequences result from intentional changes. This chapter will review the basics of the fabrication process and highlight a number of ways the fabrication process was improved as the process was stressed with the fabrication of ~100 chips using various substrates, superconducting films and other variables. The precise details of the fabrication process used for particular chips will be given in the subsequent chapters describing those detectors.

In addition to issues with the fabrication process itself, the problem of fabricating SNSPDs with high yield was also addressed. Localized defects called constrictions often limited the current that could be used to bias SNSPDs because the critical current was set by the most constricted point in the nanowire [33]. If the remainder of the nanowire could not be biased at a current density close to the critical value, the average detection efficiency was limited significantly. The density of defects that resulted in appreciable constrictions was typically high both for devices made by our group and by other groups, so yielding large area devices or large arrays of devices was not feasible. Reducing the defect density required a new source of superconducting films and the development of simple techniques for characterizing superconducting films prior to detector fabrication. SNSPDs fabricated on the best of these films

had significantly lower defect densities that removed the area-dependence of the yield for detectors with active areas as large as 100 μm^2.

3.1 Fabrication process overview and improvements

The fabrication process used in this work can be divided into four general steps: (1) dicing and chip preparation, (2) lithography, deposition and liftoff of contact pads, (3) lithography and etching of detector structures and (4) lithography, deposition and liftoff of cavity structures. A detailed description of the development of steps (2) and (3) can be found in Ref. 78, with additional information in Refs. 5, and 36, and step (4) is described in Ref. 7. These steps, related issues considered in this thesis and the solution to these issues will be described.

3.1.1 Dicing and chip preparation

The superconducting films used to fabricate SNSPDs were typically supplied on wafers or pieces of wafers that were larger than the desired chip size, so a process was needed for splitting these wafers into appropriately-sized pieces. The first step in this process was to assess the suitability of the material for detector fabrication. This could rely on both electrical measurements, which will be described in section 3.2.2, and inspection in an optical microscope to note significant defects, contamination or other visible issues. The superconducting films were commonly supplied on substrate materials such as sapphire (Al_2O_3), magnesium oxide (MgO), or silicon (Si). Both sapphire and magnesium oxide were difficult to cleave, and even silicon did not cleave well enough to reproducibly divide the supplied wafer into uniform chips (the chips used for detector fabrication were typically square and have evolved from 3.5 mm to 8 mm to the currently used 10 mm on a side). Cleaving was used to obtain a suitably-sized piece in rare cases when only a single chip was likely to be fabricated from a given wafer and the risk of losing some of the wafer was acceptable. However, in the majority of cases, chips were cut from the wafer using a dicing saw. Dicing was also used to sub-divide chips into smaller pieces after detectors were fabricated using the same process developed for dicing unprocessed wafers.

During dicing, the superconducting film needed to be protected. A layer of photoresist (Shipley 1813) was spun on top of the superconducting side of the piece or wafer. The photoresist was spun for 1 minute at 3 krpm spin speed and was baked for 3 minutes at 90ºC to evaporate any remaining solvent. The chip was typically placed photoresist and superconducting-film-face against the adhesive side of dicing tape (the preferred tape is now Ultron Systems, Inc. 1020R UV-release-type dicing tape). Note, the procedure of putting the superconducting film face down on the tape worked whenever the wafer was unpatterned, and only rough alignment was necessary, or when the substrate was transparent. The superconducting film needed to be face up if alignment to a pattern on a non-transparent substrate was required, although the superconducting surface was still coated with photoresist in this case. The dicing tape was required in order to provide a continuous surface that would be held to the vacuum chuck of the dicing saw, to which the pieces would remain secured after dicing. The preferred method for securing the wafer to the tape was to lay the wafer flat on a surface and to bend the dicing tape such that contact was initially made along a stripe near the center of the wafer. The bend in the tape was then slowly reduced so that contact with the tape progressed toward the edges of the wafer. The adhesion between the wafer and tape was then strengthened by gently pressing the tape against the wafer with a smooth, flat object, such as the side of a pair of tweezers. It was critical that strong adhesion was obtained and that no air gaps between the dicing tape and wafer were large enough to jeopardize the adhesion of the pieces to the tape after dicing. In addition to the risk of losing any pieces that did not adhere, a primary mechanism by which the dicing blade would shatter (typically damaging a considerable area of the wafer) was movement of diced pieces during a cut. An alternative approach for holding pieces in place was to use wax on a handle wafer. After several tests, the wax approach was abandoned because the wax was difficult to remove from the diced pieces, it required heating, the pieces needed to be attached superconducting-side up and the wax did not appear to hold the diced pieces any more securely than tape.

The appropriate dicing saw settings and blade depended on the substrate and the size of the diced pieces. For hard material such as Al_2O_3 and MgO, the dicing speed was slow, ~1 mm/s, and appropriate diamond tipped blades were used (such as Disco G1A851

SDC320R13B01 52×0.15×40). Blade widths as narrow as 100 µm have been used. The rate of water flow during dicing needed to be sufficient to prevent significant particle buildup on the back of the wafer and risk to the dicing blade, which could be determined using a scrap piece of the same substrate material. For dicing large pieces (> 3 mm on a side), where a ~ 100 µm-wide region on the edges of the pieces could be roughly edged, it was preferable to cut entirely through the wafer on a single pass. Although pieces as small as ~ 1 mm on a side could typically be held securely to the dicing tape if there were no air gaps and the tape had been securely pressed into place, a better approach for applications requiring smaller pieces was to make a more shallow cut, leaving ~ 20 - 50 µm thickness of material uncut. These pieces that had not been cut through completely could subsequently be cleaved along the guides defined by the cuts (while still attached to the dicing tape), producing much narrower and cleaner breaks. This approach limited the possibility of small pieces separating from the tape and prevented chipping from damaging the edges of the diced pieces. However, this approach could not guarantee the cleave would occur along a specific line, so the uncertainty in the cleave position was set by the width of the blade. Furthermore, unless the guide provided by the diced trench was along a cleave plane, a straight and clean cleave would not be obtained. Finally, the combined dicing and cleaving approach did introduce some risk: if the depth of the cut was not made sufficiently large and the cut was made along a direction other than a cleave plane, the substrate could crack during dicing or the cleave might not have followed the desired guide. These risks vary according to the substrate material and other factors, so a test piece was always diced first. Optical micrographs of chips that were diced into smaller pieces after detector fabrication, while still attached to the dicing tape, are shown for the case of dicing completely through the substrate in a single pass in Fig. 3.1(a) and the case of cleaving the chip after dicing through all but ~ 50 µm thickness of the substrate in Fig. 3.1(b).

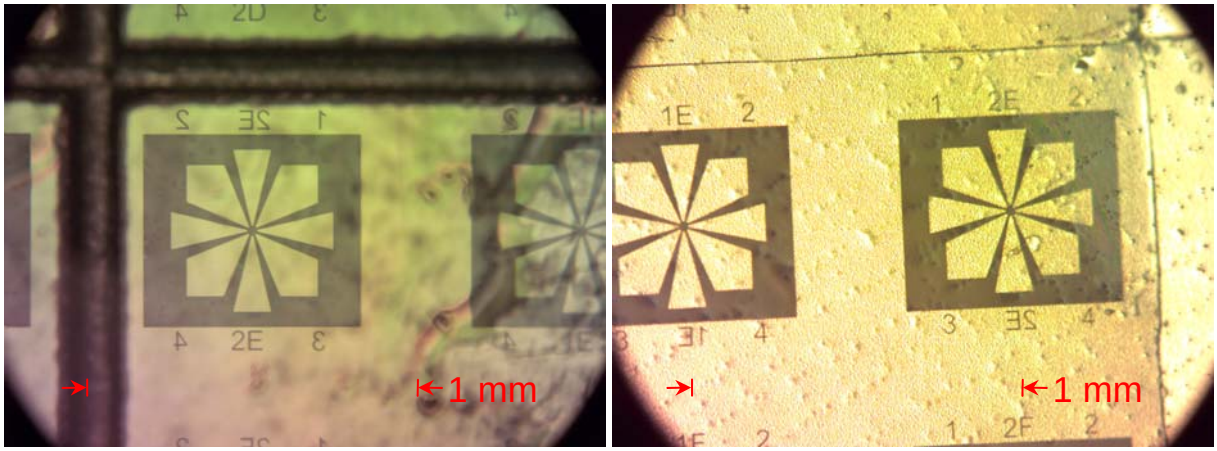

(a) (b)

Figure 3.1: Optical micrographs of diced pieces from a fabricated detector chip in which the cut was (a) sufficiently deep to fully cut through the Al_2O_3 substrate and (b) set to leave ~50 µm thickness of the Al_2O_3 substrate, which was subsequently cleaved. The cleaved cut was clearly narrower and had less chipping of the edges, but was not completely reliable. The tape, photoresist and particles present on both the back of the chip and the front of the tape were responsible for the visible distortions and texture observed in the micrographs.

Following dicing or cleaving, the chips needed to be cleaned prior to the fabrication of detectors. In the case of pieces on the dicing tape (if the superconducting film side was against the tape), the back of the pieces were first cleaned by scrubbing with a stiff cleanroom swab (Texwipe CleanTips Swab, TXTX751B) soaked in deionized water, without removing the pieces from the dicing tape. Several swabs were often needed to clean the entire surface and the procedure was carried out with sufficient deionized water and speed to avoid significant evaporation of the water. After scrubbing, the combination of tape and chips was carefully rinsed in water to remove remaining residue and was dried with nitrogen. If a UV-sensitive dicing tape was used, the tape and chips were exposed under a UV lamp for ~1 minute ($200\,mJ/cm^2$) to weaken the adhesive. All pieces were labeled by marking the tape using a lab pen (VWR permanent lab marker) to identify the location of the pieces. The labeling convention for dicing pieces is shown in Fig. 3.2. Pieces were only removed as needed, and the location of pieces was recorded (the orientation of the pieces was not typically recorded and would require identifying or marking a feature on the piece, as the orientation could not otherwise be identified after resist spinning). Portions of the wafer < 10 mm from the edge of 50.8 mm diameter wafers were not used for detector fabrication as the performance of detectors from these regions was

significantly degraded. The pieces were removed by first cutting out the section of tape to which the desired chip was attached using a razor blade and then peeling the tape away from the surface of the chip. Previously, the tape was removed from the chip in acetone with the belief that the acetone would dissolve the photoresist and promote the tape removal. This practice is now avoided to prevent dissolving the tape adhesive, which could subsequently redeposit on the chip surface and compromise adhesion of the electron-beam resist. With considerable effort, even the non-UV-sensitive dicing tapes could be removed without soaking them in a solvent, although the UV-sensitive tape was selected in part because of the ease with which it could be removed after exposure. Finally, the photoresist was removed from the surface of the chip by spraying the chip with acetone. The chip was then rinsed separately with methanol and isopropyl alcohol, in series, dried with nitrogen and inspected in the optical microscope. Although this dicing and chip preparation process typically prevented the deposition of particles on the chip surface, in cases when particles were deposited or were present before dicing, a cleanroom swab could be used to clean the surface of the chip in acetone. The chip was rinsed again with acetone, methanol and isopropyl alcohol and dried with nitrogen.

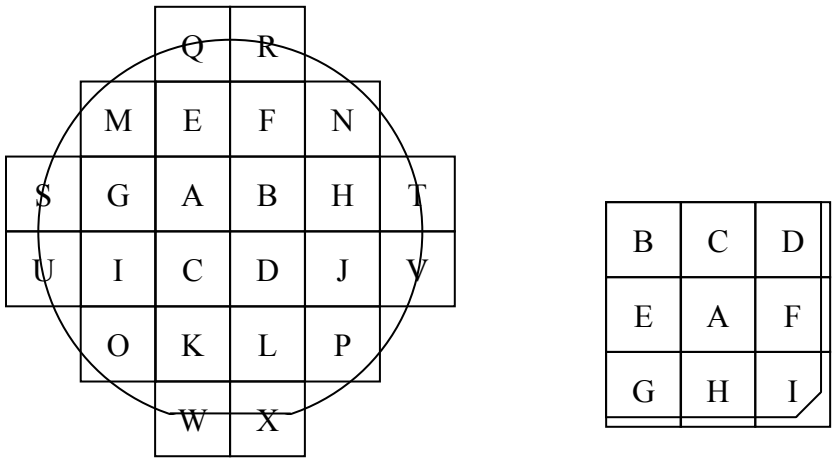

Figure 3.2: Labeling convention for square pieces diced to be10 mm-on-a-side from (a) wafers 50.8 mm in diameter and (b) approximately square pieces ~30 mm-on-a-side.

3.1.2 Lithography, evaporation and liftoff of contact pads

The contact pads were typically, although not necessarily, added before electron-beam patterning of the detector structure. Adding the contact pads first had several advantages, including significantly relaxed tolerances on the placement of the contact pad pattern and relaxed requirements on the photoresist developer used and/or the exposure dose of the electron-beam resist, which will be described in more detail below. The advantages of electron-beam patterning the detector structure first include: (1) the electron-beam resist could be spun more smoothly over the unpatterned chip, (2) fewer processing steps before application of the electron-beam resist would limit potential adhesion problems, (3) the exposed electron-beam resist could be used to protect the superconducting film that would comprise the detector from steps in the contact pad deposition process and (4) any errors that occur in the electron-beam exposure (the highest-risk step in the process) would occur before time had been wasted fabricating contact pads (and the new detector patterns offset from the old patterns could likely be written). The contact pads were fabricated before electron-beam patterning for all of the detectors discussed in this thesis, so that process will be described here, although some important points to note for the reverse process will be mentioned briefly.

The electrical-contact-pad features were defined using contact photolithography. Adhesion of photoresist directly to most superconducting films (including NbN, Nb and TaN) was acceptable. Only for materials where adhesion of the photoresist was poor (VN) was an adhesion promoter applied before spinning the photoresist. Shipley 1813 positive photoresist (positive photoresists are developed away in regions that are sufficiently exposed to UV light) was spun on the surface of the chip for 1 minute at 5.5 krpm spin speed and was baked for 3 minutes at 90ºC to evaporate any remaining solvent. The optical mask consisted of a quartz plate on which chrome had been etched into the desired pattern. The smallest sized features in most of the patterns were crosses for subsequent alignment steps, with a minimum feature size of 6 μm. Pattern transfer of this feature size, given the large tolerances on the exact size of the transferred features, could be easily obtained without hard contact between the substrate and the optical mask. Furthermore, the optical mask needed to be aligned to the chip only with a few hundred micrometer accuracy, which could be achieved by manual placement of the mask on the

chip, without the need for an optical microscope. In the case of patterning the electron-beam resist prior to the contact pads, $< 5\,\mu m$ alignment of the mask to the underlying detector features was required, and could not be performed without a microscope. For the crude alignment, the UV exposure was performed under a simple collimated, mercury-arc lamp (Tamarack Scientific Co., Inc.), the intensity of which could be easily calibrated and was typically $3.3\,mW/cm^2$. In order to obtain sufficiently close contact between the chip and the optical mask (to prevent diffraction effects from washing out small features), a weight consisting of a $\sim 10\,mm$-thick aluminum plate, $\sim 100\,mm$-on-a-side, with a $\sim 50\,mm$-diameter circular hole in the center was placed on top of the optical mask, centered on top of the chip. Air gaps between the optical mask and detector chip remained, but the corresponding optical fringes (typically ~ 10 fringes were observable across the chip) were actually used as an indication that a sufficiently small gap had been achieved. A $16\,s$ exposure time was used, in conjunction with the development process discussed next.

As part of the development process, the top surface of the photoresist was hardened in order to ensure a desirable resist-edge profile. This was accomplished by soaking the chip in chlorobenzene for 15 min [79], ensuring a slower development rate for the top surface of the resist so that the slope of the resist sidewalls would be undercut. Although undercut sidewalls were not required for clean liftoff, they did relax the requirements on the chip placement and collimation of the evaporated material. After the chlorobenzene soak, the chlorobenzene was removed from the chip using forced nitrogen and the photoresist was developed in a sodium-hydroxide-based developer (Shipley 352) for 3 minutes. Dilute tetramethylammonium-hydroxide would be a more suitable developer if the electron-beam resist had been patterned prior to the contact-pad-deposition process because a sodium-hydroxide-based developer would require the electron-beam resist to be exposed with a higher dose to avoid further development. The rate at which the photoresist dissolved from the exposed regions increased significantly after ~ 1 minute, when the full thickness of the chlorobenzene-hardened surface layer had been developed. Finally, at the end of the development time, the chip was rinsed with deionized water, first in glassware and subsequently using a flow of water. The chip was dried with nitrogen and inspected in the optical microscope to ensure proper exposure.

Potential issues with the patterning were almost always related to the exposure step – features that were missing or the wrong size were typically due to poor contact between the optical mask and the chip, while residue at the bottom of features (which could result in interference fridges when viewed in the optical microscope) was due to underexposure. In the case of underexposure, the photoresist could be developed a second time in a stronger sodium-hydroxide-based developer (5:1 Shipley 352: Shipley 351). If the patterning was still unacceptable, the entire chip could be exposed in the UV lamp and put in the developer to remove the photoresist. The chip was then scrubbed with a stiff cleanroom swab (Texwipe CleanTips Swab, TXTX751B) soaked in acetone to remove any chlorobenzene-hardened photoresist that had not been fully dissolved by the developer. Finally, the process could be restarted again at the photoresist spinning step. Several improvements to this process that could be considered in the future, but were not necessary to obtain high-quality detectors, would be the use of a negative resist designed for liftoff applications (which could eliminate the need for the chlorobenzene soak), the addition of a antireflection coating layer beneath the photoresist, which could improve the sidewall roughness and increase the range of acceptable exposure doses, and the use of a flexible optical mask (which could provide all of these benefits).

After the appropriate pattern was transferred into the photoresist, the contact pad metals were evaporated and liftoff was used to remove the unwanted metal from regions covered by photoresist. Electron-beam evaporation (base pressure of $\leq 2 \times 10^{-6}$ Torr and deposition rate of 0.5 nm/s) was used to deposit 10 nm of titanium, followed by 50 nm of gold. The titanium provided adhesion between the superconducting film and the gold, while the gold provided a good electrical contact layer, free from oxidation and sufficiently soft for subsequently electrical testing. Liftoff was performed in N-Methyl-2-pyrrolidone (NMP) heated to 90ºC. The length of time required for the metal to liftoff was dependent on the pattern. Early in this work, patterns with electrically isolated contacts pads for each detector were replaced with patterns that used a single ground plane, in order to facilitate scanning-electron microscopy of the detectors after etching, as described in section 3.2.1. The patterns with a continuous ground-plane required liftoff of features that were all small in size, which occurred within seconds in the heated NMP. Conversely, the liftoff of large features often took several minutes or longer. Although the rapid

liftoff of small features was desirable, the small size and large number of features made it likely some would redeposit on the substrate. After liftoff in the NMP, the chip was transferred to acetone-filled glassware at room-temperature. A gentle spray of acetone was used to remove any redeposited features that were large, or were sticking out from the surface. Such features would obstruct the smooth flow of the acetone over the surface and could be readily identified. Although there were typically some redeposited features that could not be removed, only the features obstructing the flow of acetone were critically important, as they would also obstruct the electron-beam resist during spinning, preventing the application of a smooth layer. Finally, the chips were rinsed in deionized water flowing from the faucet, dried with nitrogen and inspected in the optical microscope.

3.1.3 Lithography and etching of the detector structures

The nanowires were patterned in resist using electron-beam lithography and this pattern was transferred into the superconducting film using reactive ion etching. After fabricating the contact pads, the chip was dipped in 25% tetramethylammonium hydroxide (TMAH) for 4 minutes. The TMAH cleaning step was required to remove contaminates that would be attacked during the development process and could prevent adhesion of the electron-beam resist to the superconducting film. It was likely that one source of such contaminants was related to the chlorobenzene dip, which tended to produce thin layers of photoresist that did not dissolve readily in NMP or acetone and may have been redeposited during liftoff. Other sources of adhesion problems included organics on the superconducting film surface that accumulated during chip and wafer storage. In the case of NbN films, there was no evidence the TMAH soak damaged the film surface or degraded the detector properties. Within 20 minutes of the TMAH cleaning step, hydrogen silsesquioxane (HSQ) resist was spun onto the surface of the chip. The dilution of HSQ resist in methyl isobutyl ketone solvent and the spin speed were selected in order to obtain the desired resist thickness. This thickness was typically ~90 - 100 nm, although HSQ as thin as ~60 nm was sufficient for use as an etch mask. Early in the research, the chip was baked at 90ºC for 3 minutes in order to evaporate any remaining solvent, although this baking step was subsequently eliminated.

The HSQ resist was patterned using a Raith 150 electron-beam lithography tool with an accelerating voltage of 30 keV. Early in the research, an aperture size of 20 μm was used while later a 30 μm aperture was found to permit faster write times without degrading the patterning results. The dose of different features was varied in order to minimize proximity effect, with a dose of ~300 - 600 μC/cm^2 being typical for non-isolated features (doses as high as 1500 μC/cm^2 were used for small, isolated features). Dose matrices were always patterned in order to determine the proper dosing whenever a new pattern was introduced, a new substrate or new bottle of HSQ was used, or more than two months had passed since the previous dose matrix was written. The selected dose was ~10% lower than the dose at which appreciable footing could be observed. Dose matrices were often written on scrap pieces from the edge of the wafer or, in cases when the goal was simply to determine the dosing of new patterns or confirm the dosing of patterns, they were written on unused portions of a detector chip in the same lithography step as the detector patterns.

In addition to improper dosing, the quality of the patterned detector structures was also critically dependent on how well the electron beam was focused. While patterning over a small fraction of a chip could be performed without requiring a change in focus, chips and wafers were rarely level enough to permit high-resolution patterning over their full area with a fixed working distance. Although the Raith 150 tool did have piezoelectric elements that could be used for leveling, a much simpler procedure was employed in this thesis to maintain focus across a chip. First, the chip was mounted to be as level as possible on the chuck by avoiding scratches in the chuck, removing particulates or resist from the surface of the chuck and the back of the chip and by clipping the chip to the chuck in such a way that the clip did not angle the chip. It was also important that the chip be placed on a solid region of the chuck, that electrical contact be established between the substrate or top surface of the chip and the chuck and that the clip be placed as far as possible from areas of the chip that would be patterned, because all of these could affect the electric fields that focused the electrons. With minimal effort to mount the chip correctly, the working distance across a 10 mm-wide chip varied by less than 30 μm; with a reasonable level of effort, this variation was typically less than 5 μm. However, even a 5 μm variation in working distance was large compared to the < 1 μm depth of focus of the electron-

beam. To compensate for this remaining variation in working distance, dynamic focus correction was employed, in which the working-distance of the electron-beam was recorded when it was focused at three points near the edges of the chip. The Raith 150 software fit these points to a plane and interpolated the working distance for each write-field. The advantages of this approach were that it was far less time consuming than leveling the chip with the piezoelectric elements and it could compensate for much larger tilt angles (which were commonly required to level small chips). The disadvantages of dynamic focus correction were that each writefield was rotated slightly as the working distance was changed (mostly a problem for features extending across writefields) and the working distance was fixed within a write field (this would only be a problem for very small chips, large write fields or highly tilted samples – a 5 μm variation in working distance across a 10 mm-wide chip would correspond to a negligible 50 nm variation in working distance across a 100 μm writefield). Neither of these drawbacks were important for patterning small-area SNSPDs. Finally, the focus was checked at several points across the chip after dynamic focus correction was enabled because the correction procedure often needed to be repeated two or three times before the correction was acceptable.

Finally, several features were added to the detector structures that did not alter the detector electrical operation, but did improve the fabrication uniformity and yield. Proximity effects, in which the exposure dose at each point was affected in part by the level of exposure nearby, was particularly important to consider when making SNSPDs with HSQ because of the high sensitivity of the detectors to line-width variations and the low development contrast of the HSQ resist (using the development process described below). Proximity effect could be corrected either by adding dummy features precisely chosen based on calculations [78] or by adding electrically disconnected, but otherwise identical, dummy nanowire features extending ~5 μm beyond the edge of the detector area [36]. The second approach was used in most cases because of its simplicity and its ability to precisely correct SNSPD-type patterns. In addition to the proximity-effect-correction features, additional dummy patterns were eventually added to the process to ensure adhesion of the HSQ pattern on top of the contact pads. Adhesion of the HSQ to the gold contact pads was often poor, as seen in Fig. 3.3(a) where the HSQ feature peeled off the contact pad and folded back across the dummy proximity-effect features. The simplest way

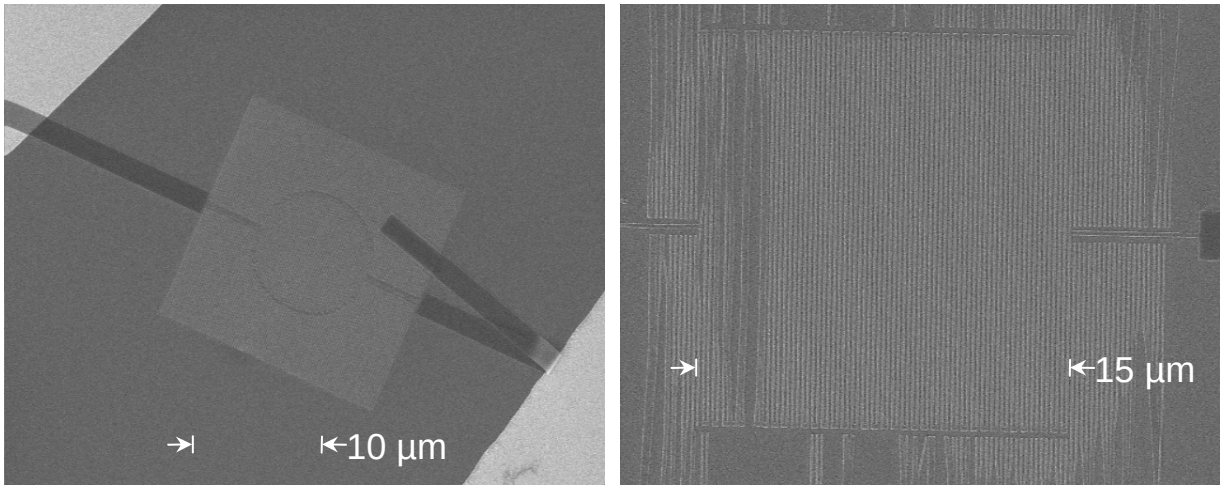

(a) (b)

Figure 3.3: Scanning-electron micrographs of patterned HSQ. (a) The adhesion of the HSQ feature on the right to the gold contact pad was poor, resulting in the HSQ feature peeling back. (b) The adhesion of the HSQ features defining the detector meander and the proximity-effect-correction features was poor.

to overcome this problem was to add ~5 µm-by-5 µm square patterns with ~600 µC/cm^2 dose over the region of the contact pad with an exposed HSQ feature, since the size and shape of the HSQ feature on the gold did not affect the detector, and larger higher dose features adhered better. These high-dose squares adhered well to the gold, and if they were ≥10 µm from the detector pattern, they did not affect the dosing of the nanowire features. Finally, increasing the size of the HSQ connection to the underlying contact pads reduced the required alignment tolerance.

Within several hours of electron-beam exposure, the HSQ resist was developed in 25% TMAH for 4 minutes. Optical microscopy and scanning-electron microscopy were used to verify that the patterned HSQ had adhered well to the superconducting film, was correctly dosed and had sharply defined edges (i.e. the electron beam was in focus) at the corners and at several additional points across the chip. Fig. 3.3(b) is an example of poor adhesion of the HSQ to the superconducting film, in which many on the HSQ nanostructures peeled away. Poor adhesion of HSQ to NbN (as well as TaN) was generally found to be caused by contaminants on the superconducting film surface. Removing the dicing tape without using acetone (section 3.1.1) and cleaning the chip surface with TMAH prior to spinning HSQ (section 3.1.3) were generally

found to be sufficient to achieve good adhesion. Although these steps permitted good adhesion of the HSQ to NbN and TaN, a process was not found that permitted good adhesion of HSQ to VN.

Differentiating focus and dose problems was important, because although they could result in similar patterning issues, they were solved in different ways. Fig. 3.4 shows scanning-electron-micrograph images of detector structures with (a) correct dosing and focus, (b) incorrect focus, but correct dosing, (c) correct focus, but slightly excessive dosing, and (d) correct focus and excessive dosing. Note that in the case of incorrect focus, the edges of the features were not sharp and resist had been exposed between the desired features just to the edge of the patterned features. In contrast, in the case of excessive dosing, the edges of the features remained sharp while the resist was exposed both between and around the desired features. This undesired resist exposure appears first as "footing" in areas with the highest exposure dose (near the bends in the meander). In cases where the focus, dosing or alignment was poor, there was typically no way to repeat the electron-beam patterning step because no effective way to remove the HSQ without damaging the NbN or contact pads was found. Although not used in this work, it may be possible to repeat the resist spinning, exposure and development steps to add small features to bridge alignment errors, or to redefine the detector structures in cases where the alignment, dosing or adhesion were so bad that entirely new detector structures could be written.

After inspection of the HSQ, the pattern was transferred into the superconducting film using a reactive ion etching process in CF_4 gas. The HSQ resist and the contact pads served as a mask, so that the underlying superconducting film was not etched. The etching process was performed in a PlasmaTherm reactive ion etching tool, using a pressure of 10 mTorr, a flow rate of 15 sccm CF_4 and 100 W of RF power. The substrate was cooled with helium and a microscope coverslip was used to cover the larger aperture in the chamber that affected the DC level during etching. While the etch rate of HSQ using this process could be precisely measured, the etch rate of thin superconducting films was considerably more difficult to measure. These difficulties arose because of (1) challenges measuring the thickness of such thin films, (2) etching and fluorination of substrate materials from which the thickness was measured, and (3) different etch rates for the superconducting material and any thin oxide present on the surface.

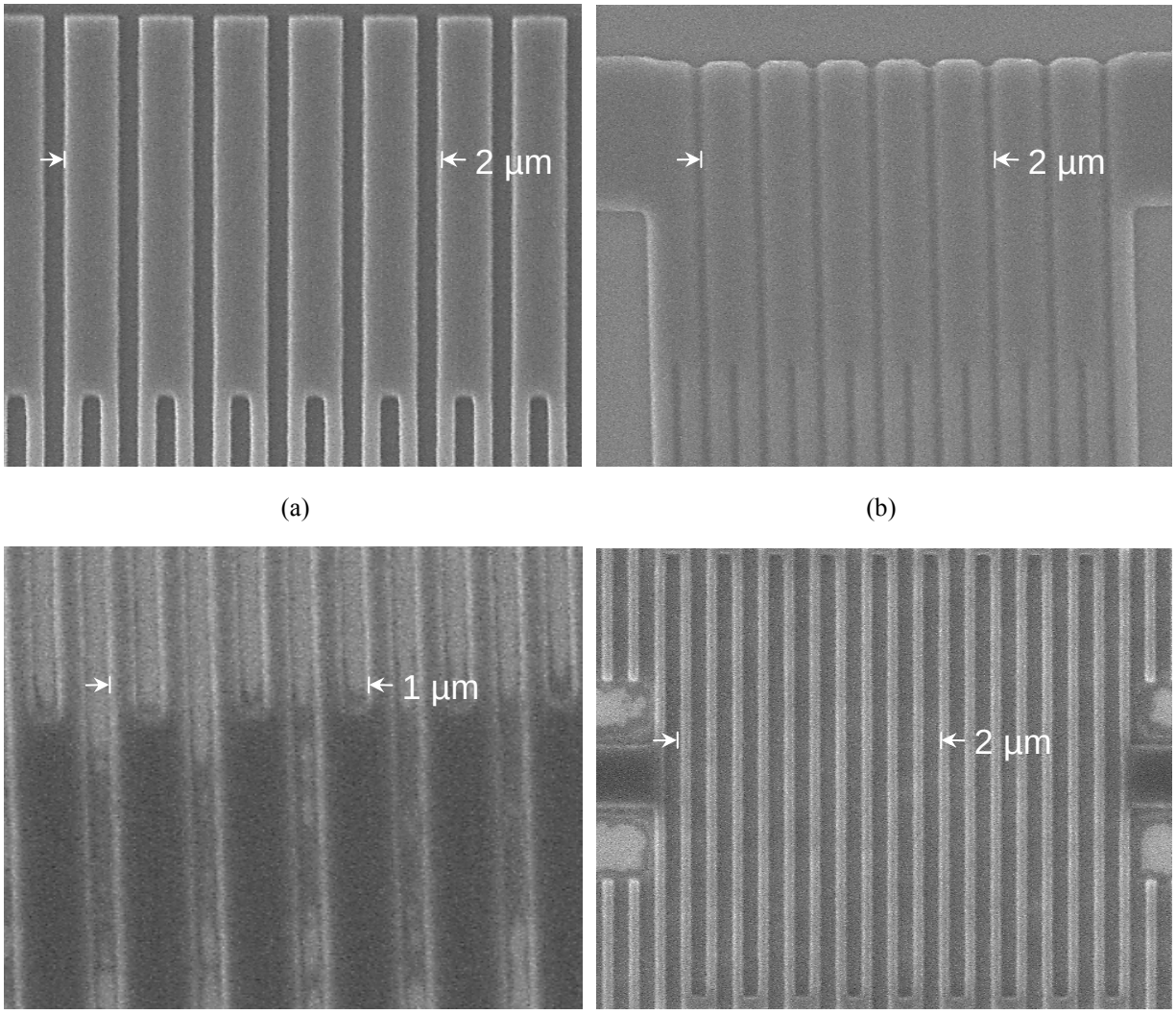

Figure 3.4: Scanning-electron micrographs of patterned HSQ. The images were taken of patterns with (a) correct electron-beam focus and dosing, (b) incorrect focus, but correct dosing, (c) correct focus, but slightly excessive (~20%) dosing, and (d) correct focus and excessive (~40%) dosing.

Furthermore, the superconducting film and oxide thicknesses varied slightly between chips, so highly accurate etch rates could not be used to precisely time the etch process anyway. Table 3.1 summarizes the approximate etch rates for several materials considered in the work using the etch process described above.

The fast etch rate of HSQ in this process provided both advantages and disadvantages. It was problematic because it required that the HSQ resist be several times thicker (considerably

Material	Etch Rate	Comments
HSQ	20 nm/min	Measured for high exposure dose
NbN	~6 nm/min	Thin films; includes native oxide
TaN	>6 nm/min	Thin films; includes native oxide
VN	~1 nm/min	Thin films; includes native oxide
Ti	~3 nm/min	Includes native oxide
Au	<1 nm/min	

Table 3.1: Etch rates for several materials using a reactive ion etching process with a flow rate of 15 sccm CF_4, 10 mTorr pressure and 100 W of RF power.

more to provide margin for process variations) than the superconducting film it was being used to protect. However, the fast etch rate of HSQ did ensure that any thin layers of residual resist between the desired features would not be a problem (they were quickly removed in the CF_4–based etch, without requiring an additional step) and there were no concerns with the HSQ etch mask being sputtered onto the superconducting film and preventing etching of the superconducting film, since the HSQ was etched and SiF_4 was reactive. Finally, the anisotropic nature of reactive ion etching, combined with the high rate of HSQ etching, ensured that no superconducting material beneath the HSQ was etched and that the line-edge roughness of the etched wires was determined primarily by the smoothness of the HSQ.

3.1.4 Lithography, deposition and liftoff of cavity structures

In order to increase optical absorption in the detectors, as discussed in section 1.3.2, cavity structures were added to detectors that were used to demonstrate high detection efficiency. The fabrication process for this cavity structure closely followed the process described in Ref. 7, with a few important changes.

The first step in making the cavity structure was the fabrication of the dielectric layer, which consisted of electron-beam exposure of HSQ, a spin-on glass that became roughly SiO_2

during the electron-beam exposure. A layer of HSQ was spun to a thickness 30 – 50 nm thicker than the desired thickness of the optical cavity, independent of the thickness of the patterned HSQ remaining on the underlying nanowires. After spinning of the HSQ, the sample was baked at 90ºC for 3 minutes and aquaSAVE (Mitsubishi Rayon America Inc.), a conductive spin-on polymer, was spun onto the devices at 3 krpm in order to provide a continuous, conductive film through which charging of the sample could be prevented during electron-beam patterning. Large, 40 μm by 40 μm square areas were exposed in the Raith 150 electron-beam lithography tool, centered on the detector area. This exposure was performed with a 60 μm aperture (to increase beam current; patterning resolution was not critical) at 10 kV acceleration voltage with an exposure dose of 600 $\mu C/cm^2$. This high exposure dose ensured that the HSQ became sufficiently crosslinked to avoid chemical attack during subsequent development of a photoresist layer in a sodium-hydroxide-based developer. The exposed HSQ was developed in 25% TMAH for 4 minutes, rinsed in deionized water and dried with nitrogen.

Following development of the dielectric spacers, the height of the features was measured and reduced as necessary using reactive-ion etching. The height of the spacer could be measured to sufficient accuracy using a Dektak profilometer (Figure 3.5(a)). The dielectric spacer was typically 30 – 50 nm thicker than the desired cavity thickness (the thickness of the HSQ was reduced during electron-beam exposure, see Ref. 80, but it was thicker over the active area of the detector as a result of the length scale over which it planarized on top of the underlying HSQ meander). The thickness of the dielectric spacer could then be reduced by reactive ion etching in the same CF_4-based process described above (see section 3.1.3). The etch rate of the electron-beam-cured HSQ was 20 nm/min (± 1 nm/min) after the 600 $\mu C/cm^2$ exposure with 10 kV electrons. It is important to note that all of the detectors on the chip had to be covered with an HSQ spacer (or photoresist) during this etch step. Although similar cavity structures could be fabricated by evaporating SiO_x and the metal reflector at the same time, eliminating the need to define the dielectric spacer using electron-beam lithography, there are drawbacks to this approach. Evaporating the dielectric spacer directly on top of the HSQ pattern used to define the detector could result in voids, a non-planar cavity surface or a high-uncertainty in the dielectric spacer thickness, while removing the underlying HSQ pattern could damage the detector

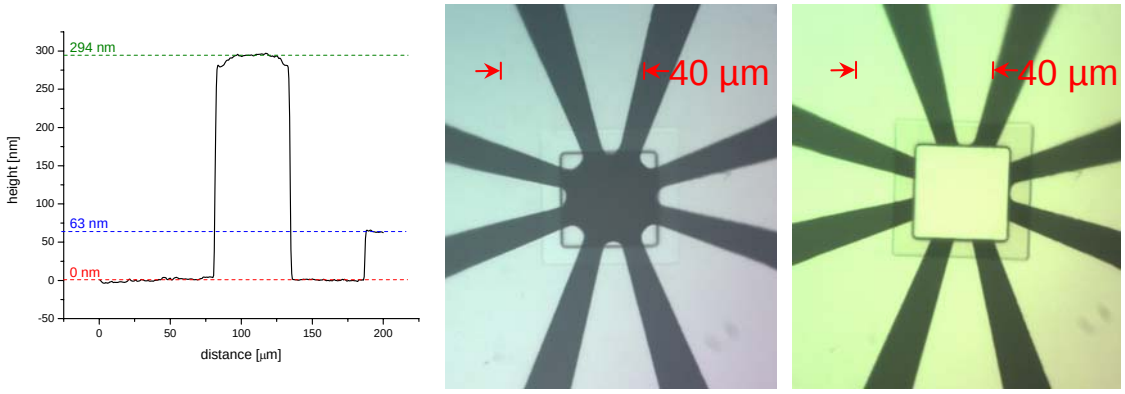

(a) (b) (c)

Figure 3.5: (a) Height versus position data obtained using a Dektak profilometer for a dielectric spacer (center feature) and the 10 nm Ti / 50 nm Au contact pad (right feature). The center region of the dielectric spacer was taller than the edges because of the way the HSQ resist planarized over the underlying HSQ meander pattern. The height of the dielectric spacer over the device active area measured from this profile was 294 nm (± 5 nm) and the contact pad feature was 63 nm (± 5 nm). (b, c) Optical microscope images of (b) the completed dielectric spacer (faint larger square in center of the image) and the photoresist layer used for liftoff of the cavity structure (photoresist covers everywhere except the center square region inside the dark outline) and (c) the completed cavity structure.

structure. Consequently, spinning and electron-beam exposing HSQ over the detectors was viewed as a safer approach considering that it had been previously demonstrated that smooth, continuous, dielectric spacers could be achieved (as evidenced by AFM and TEM evaluation in Ref. 7). Finally, the new process of etching back the HSQ permitted the thickness of the dielectric spacer to be accurately measured and controlled, without the need to remove the underlying HSQ meander.

After fabricating the dielectric spacers, the final step was to fabricate the reflectors using a photoresist-based liftoff process similar to the one used to pattern the contact pads. The primary differences were the need to align the photolithography to the underlying detector structures and the need to minimize the thickness of the titanium adhesion layer to improve the optical properties of the reflector. Identical to the contact pad process, a ~ 1.2 µm-thick layer of Shipley 1813 was spun on the chip at 5.5 krpm and baked at 90ºC for 3 minutes. The photomask was aligned to the underlying contact pad layer using a Karl Suss MJB3 contact aligner (high-resolution model in the Experimental Materials Laboratory at MIT) and exposed for 1 minute (~ 50 mJ/cm^2). The chip was soaked in chlorobenzene for 15 minutes, developed in Microposit

352 (sodium hydroxide-based developer) for 3 minutes, rinsed in deionized water and dried with nitrogen. The chip was inspected with an optical microscope to confirm that a sufficiently high dose was used in order to achieve full development (no residual photoresist was visible in regions that should have been developed), as shown in Fig. 3.5(b). A reflector layer consisting of 1 nm of Ti and 120 nm of Au was evaporated on the chip (base pressure of $\leq 2 \times 10^{-6}$ Torr and deposition rate of 0.5 nm/s). Liftoff was performed in N-Methyl-2-pyrrolidone (NMP) heated to 90ºC and subsequently rinsed in room-temperature acetone and deionized water. The continuous Ti / Au sheet lifted-off in order to define the cavity reflectors typically took $1-2$ minutes to peel off completely and was often aided by gentle agitation of the chip in the NMP. In cases when an edge or corner of this Ti / Au film remained adhered to the chip, the chip was moved to the acetone soak with the film folded away from the surface of the chip and could be fully removed with a gentle acetone spray. Following the deionized water rinse, the chip was dried with nitrogen and inspected in the optical microscope to ensure adhesion of the reflectors, as is shown in Fig. 3.5(c). Reflectors with good adhesion and smoothness were achieved with high yield ($>95\%$) despite the thinness of the titanium adhesion layer.

3.1.5 SNSPD fabrication process summary

The basic SNSPD fabrication process used throughout this thesis, which had been previously developed [78], has been described. Improvements to this process introduced in this research included developing a robust dicing and cleaning procedure that did not require scrubbing the chip, fabricating a continuous ground plane to permit scanning-electron-imaging of patterned detectors, using dynamic focus correction to permit consistent patterning across reasonable-size areas on a chip and etching back the cavity dielectric spacer to ensure the proper thickness was achieved over non-uniform topography. Finally, fabrication issues related to using superconducting materials other than NbN and other potential changes to this process were discussed throughout the section.

3.2 High yield SNSPDs

Although the fabrication process describe in section 3.1 enabled high detection efficiencies to be achieved for small-area detectors [7], it was also useful to investigate how high detection efficiencies could consistently be obtained, even for large-area detectors. Large-area detectors were difficult to obtain with high yield because of random defects that caused detectors to be constricted, as described in Ref. 33 and section 1.3.1. In constricted detectors, the critical current was limited by the properties at a single isolated location, preventing the remainder of the nanowire from reaching a current density near the critical value. Photon absorption in constricted detectors occurred throughout the detector active area, but the probability of photon detection was low everywhere except near the constriction, which made the overall efficiency of the detector low. In order to increase the detector yield, the density of defects resulting in appreciable constrictions need to be reduced dramatically. This section describes a successful effort to dramatically reduce the probability of constrictions and increase the yield of high efficiency detectors.

3.2.1 Identifying the source of constrictions

The first step in reducing the defects that result in constrictions was to identify their source, or at least determine whether the constrictions were introduced prior to fabrication or during the fabrication process in order to determine what might be done to eliminate them. In order to isolate whether the defects were introduced prior to the fabrication process, the approach taken was to look for evidence that the defects were fabrication-related. This approach consisted of two steps: device inspection to look for patterning defects and correlation of the defect density with fabrication details and the wafer from which the NbN material was obtained.

The simplest source of constrictions, both conceptually and in terms of identification, would be patterning defects that limit the wire width at a single point. Constricted detectors with critical currents suppressed by 50% or more could be identified by electrical measurements and patterning defects resulting in a 50% narrowing of the wire should have been readily visible by scanning-electron-microscope inspection, so the identification of patterning errors that explain

the observed level of constriction should have been straightforward. Due to charging of the insulating sapphire substrate, high-quality scanning-electron-microscope images could only be obtained from devices with a continuous ground plane, a change that was introduced early in this work. Attempts to image electrically isolated detectors using an environmental scanning-electron microscope (using a sufficiently high pressure of water vapor to eliminate the charging effects), did not result in images with as high contrast as permitted with the continuous ground plane and a high-vacuum scanning-electron microscope. None of the images taken with either approach showed evidence of any patterning defects on the scale required to explain the reduced critical current.

In addition to the lack of evidence suggesting patterning defects, the defect density varied widely between chips and, to a much lesser extent, across chips. Given that the fabrication and testing of detectors was time-consuming, rather than quantitatively testing the dependence of the defect density on many potential parameters, a qualitative approach was taken to categorizing the performance of previously fabricated and tested detectors. The performance of standard, 3 μm x 3.3 μm area detectors from many previously fabricated chips were roughly classified by average detection efficiency and the results used to look for correlations between the detector performance and either the wafer from which the NbN material was obtained or the fabrication run and the individual who fabricated the chip. The performance of the detectors was clearly most correlated with the wafer from which the chip was fabricated, even though these wafers were nominally identical in terms of their source, the deposition process and the film properties (including room-temperature resistivity and critical temperature). It should be noted that while this evaluation was not quantitative, nor did it attempt to separate constriction-related limitations to the detection efficiency from other limitations, the identified correlation between detector performance and the superconducting films did indicate that better control over the superconducting films was critical to reliably obtaining detectors with high efficiency.

3.2.2 Superconducting NbN films for SNSPDs

Although the deposition of superconducting NbN thin films was beyond the scope of this thesis, several important ways of evaluating the potential of these films for use in fabricating SNSPDs

were investigated. This section will describe these techniques and how they were used to optimize the NbN deposition conditions in a collaborative effort with Dr. Richard Molnar at MIT Lincoln Laboratory to better understand and control the superconducting properties of NbN thin films. There were many variables that affected the properties of superconducting thin films, but four of the most important for SNSPDs were the substrate material and surface quality, the thickness of the NbN, the ratio of niobium (Nb) to nitrogen (N) to various impurities in the films, and the energetics of the film deposition. In order to investigate how these properties affected the detector performance and how they could be controlled during the deposition process, the NbN films needed to first be sufficiently optimized to permit reliable detector performance. The techniques for evaluating superconducting films described in the remainder of this section guided this initial optimization, and to some extent a stabilization, of the NbN deposition process.

Given that the NbN films deposited at Moscow State Pedagogical University [81] were successfully used to make all of the detectors described in chapter 4 and chapter 5, the initial goal of the collaborative work with MIT Lincoln Laboratory was to deposit NbN films using a nearly identical process before attempting to improve upon it. Both processes deposited thin NbN films by DC magnetron sputtering with a fixed current bias, often on r-plane sapphire substrates heated to temperatures as high as ~800ºC. However, it was likely that the substrate preparation, total deposition pressure, N_2 partial pressure, target-to-substrate distance, bias current, system base pressure and sources of impurities differed between the systems, because these were not precisely known for the process at Moscow State Pedagogical University and were varied in some cases to optimize the films deposited at MIT Lincoln Laboratory.

Although the most straightforward approach to understanding how the deposition parameters affect the detector performance would be to directly measure the various dependencies, this was not feasible without some way of initially optimizing and stabilizing the deposition process. This film evaluation requirement arose both because of the difficulty of fabricating and testing detectors on a large number of samples and because deposition conditions were often changing unintentionally to a degree that impacts detector performance. Many evaluation techniques were considered, including transmission electron microscopy, atomic force

microscopy, x-ray analysis, and electrical characterization. The method ultimately determined to be most effective, however, was electrical characterization.

Several important properties of the films could be determined using a relatively simple electrical characterization that did not require modifying the film in any way. This characterization consisted of contacting the film with four gold-plated, spring-loaded pins arranged in a line with equal spacing (Fig. 3.6(a)). Such a four-point measurement allows the resistivity of the film to be measured independent of the potentially variable contact resistance, because the current was sourced and the resultant voltage drop in the sample was measured using separate pairs of pins, with negligible current flow or additional voltage drop in the connections used to measure the voltage [82]. By lowering this setup slowly into liquid helium (Fig. 3.6(b)), the resistivity of the film as a function of temperature could also be measured, again independent of any changes in contact resistance. Based on the measured resistivity versus temperature curve (Fig. 3.6(c)), the three key numbers that were extracted were the room-temperature resistivity (R_{300K}), the residual resistance ratio (RRR), defined here to be the ratio of the resistivity at room-

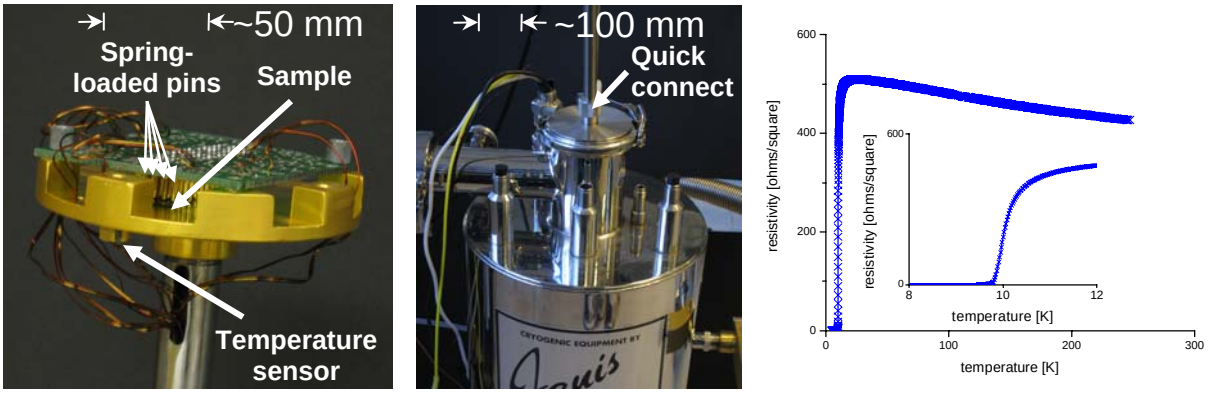

(a) (b) (c)

Figure 3.6: (a) Sample holder and spring-loaded pins for four-point resistivity measurements that was designed and built in large part by Charles Herder. Sixteen rows with four pins each were arranged for testing multiple samples as small as 8 mm across or for characterizing the uniformity of samples with diameters as large as 50.8 mm. (b) Liquid helium dewar in which sample holders could be lowered. The quick connect clamp permits the level of the sample holder in the dewar to be adjusted. (c) Resistance vs. temperature measured on a NbN film exhibiting a T_c=10.1 K, RRR=0.81 and R_{300K}=414 Ω/□.

temperature to that just before the superconducting transition at 20 K ($RRR = R_{300K} / R_{20K}$), and the temperature at which the resistivity of the film was halfway between R_{20K} and zero.

The electrical characterization of the superconducting NbN thin films provided many important mechanisms by which to optimize and screen the films prior to detector fabrication. During optimization, or re-optimization in the case of attempting to redeposit the same film multiple times, the electrical characterization indicated several things about the films. First, the measurement of T_c was the critical feedback mechanism. In addition to this feedback, *RRR* could be used to determine whether there was too much nitrogen in the films (*RRR* was higher than desired) or too little (low *RRR*), and in combination with the absolute value of the resistivity at room temperature, could be used to optimize the deposition time to achieve the desired thickness. The resistivity was actually an excellent way to optimize the deposition time to achieve consistent critical currents per unit width of wire, whether changes were warranted due to target depletion or the use of a different substrate material. The initial optimization at MIT Lincoln Laboratory consisted of varying the partial pressure of N_2, the total deposition pressure, the substrate temperature and the substrate material in order to maximize T_c, while attempting to roughly match the resistivity of the films deposited at Moscow State Pedagogical University by adjusting the deposition time. The initial target electrical parameters for NbN films used for the fabrication of SNSPDs were $\sim 450\,\Omega/\square$ room temperature resistivity, $RRR \approx 0.85$ and as high a T_c as possible, typically 10.5 K – 12 K. Note that while these optimal parameters were found to be fairly consistent for NbN deposited over a wide range of total deposition pressures and substrate materials, they were likely unique to NbN and not quantitatively correct for other superconducting materials.

Although superconducting films have been deposited with a wide range of deposition parameters and spread in electrical parameters from the target values discussed above, only a subset of these films have been evaluated by fabricating and testing SNSPDs. The three deposition parameters that have been varied in order to investigate their influence on SNSPD performance were the deposition time, the substrate material and the total deposition pressure. The deposition time strongly affects the performance of the detectors, with deposition times as little as 25% higher resulting in detectors with several times lower average detection efficiency

and 25% shorter deposition times resulting in devices with nearly zero critical currents. The substrate material has not been investigated sufficiently, but appears to affect several important parameters such as the thermal boundary resistance. The highest efficiency detectors to date have been demonstrated on r-plane sapphire, but more work is needed to fully investigate the potential of alternative substrates. Finally, reducing the deposition pressure allowed NbN films to be obtained with a higher T_c for a given resistivity, but detectors fabricated from these films have not demonstrated as high detection efficiency. This issue also requires further investigation and would be particularly interesting if it holds true over a range of other deposition conditions, because most published work on the deposition of NbN thin films for SNSPDs is performed at very low total pressures.

3.2.3 Reduced defect density

Improving the yield of high-detection-efficiency SNSPDs was the primary motivation for investigating the NbN deposition in more detail, so the remainder of this section will focus on the performance of detectors fabricated from the NbN films best-suited to this purpose. The films resulting in the highest detection efficiency SNSPDs were deposited on r-plane sapphire. The sapphire wafers were ordered with an epi-front-side polish and optical-back-side polish from Kyocera, cleaned using a heated acid bath to etch a thin layer from the surface, back-side coated with a ~100 nm-thick layer of sputtered tungsten, and radiatively heated to ~800ºC. The deposition was performed at a total pressure of 8 mTorr, with 100 sccm flow of Ar and 5 sccm flow of N_2. The two wafers with NbN films used to demonstrate higher yield were deposited under the same controllable conditions, but after many intervening depositions over a several month period had resulted in a 7% drop in the target voltage, most likely due to target depletion. The measured electrical properties of these films and the performance of SNSPDs were the same for both films, within the noise typical across a single chip or wafer. Portions of the wafer <10 mm from the edge were not used for detector fabrication as the performance of detectors from these regions was significantly degraded.

While the performance of detectors would ideally be compared by measuring the detection efficiency of each SNSPD, a more efficient approach was taken to evaluate the yield of

a large number of detectors. This approach [33] relied on measuring the critical current, which was set by the point in the device with the lowest product of critical-current density and cross-sectional area. The critical current for each detector was multiplied by its room-temperature resistance in order to compensate for slow variations in the average cross-sectional area of each detector, which may have been due to variations in the film thickness or variation of the linewidth of the exposed features across the chip. The room-temperature resistance was proportional to the length of the nanowire – which was very accurately set by the lithography – and inversely proportional to the average cross-sectional area of the detector. Thus, the product of critical current and room-temperature resistance gave a number independent of the average cross-sectional area, but still proportional to the minimum value of the product of the critical current density and the fractional cross-sectional area. This product of the measured critical current and room-temperature resistance was defined to be the constriction factor C, normalized so that $C = 1$ corresponded to a wire that was perfectly uniform along its entire length.

Using this definition of the constriction factor, C, it was possible to quickly measure the extent to which a large number of detectors had critical currents limited by defects. In Fig. 3.7, histograms from two different size detectors fabricated on a film from Moscow State Pedagogical University are shown (reproduced from data in Ref. 33). Both the detection efficiency of the least constricted detectors with 3 μm-by-3.3 μm areas, and measurements of their inductance as a function of bias current [33] indicated that the best detectors on this chip were among the best demonstrated on any film. Similar histograms are shown in Fig. 3.8 for five different detector types measured on a chip fabricated from the NbN deposited at MIT Lincoln Laboratory. Note that these histograms have not been normalized by the measured inductances as a function of bias current, as is the case in Fig. 3.7, but instead were normalized to the maximum measured constriction factor ($\max(C) = 1$). This normalization was justified by the detection efficiency measurements, which indicated that the best detectors on this chip had device detection efficiencies of ~50% after the addition of an optical cavity. Furthermore, the narrow distribution of constriction factors, particularly for detectors with large areas, clearly indicated a much smaller distribution of defect sizes. Thus, the combination of the detection efficiency measurements performed on ~30 detectors and the narrow distributions of constriction

factors measured for several hundred detectors indicated that the probability of large defects had been drastically reduced on the NbN films deposited at MIT Lincoln Laboratory.

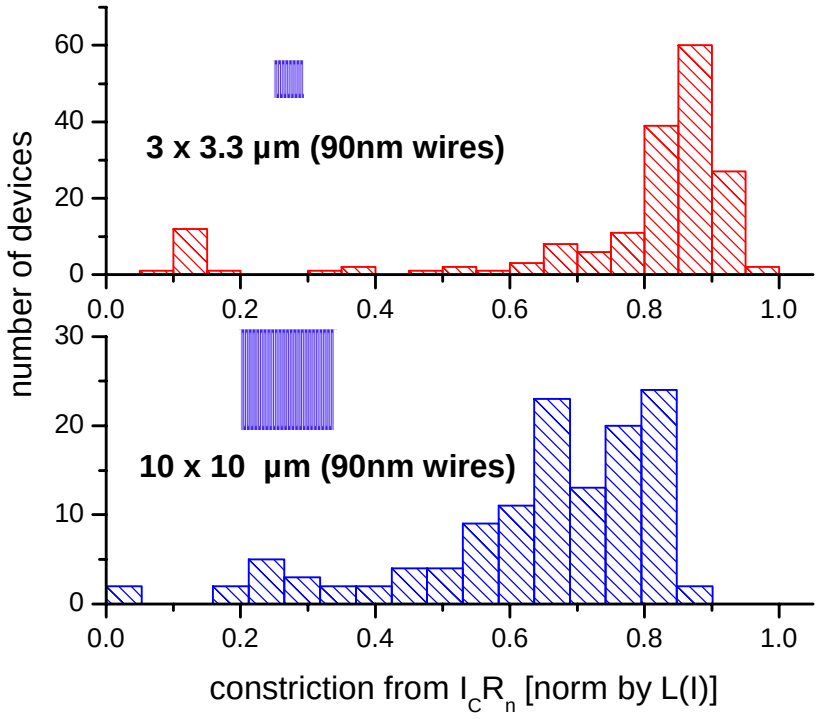

Figure 3.7: Histogram of measured values for the product of I_c and R_n for SNSPDs fabricated on NbN films deposited at Moscow State Pedagogical University. The values in the histogram were normalized by the maximum product of I_c and R_n possible for such a nanowire, determined using measurements of the inductance as a function of current (see Ref. 33). The insets show the layout and size of the nanowires from which the data was obtained, with the top (red) histogram measured on ~50 µm long nanowires and the bottom (blue) histogram measured on ~500 µm long nanowires. The histograms indicate that the probability of a nanowire being constricted was a strong function of the nanowire length, and that nanowires ~500 µm in length were very likely to be significantly constricted.

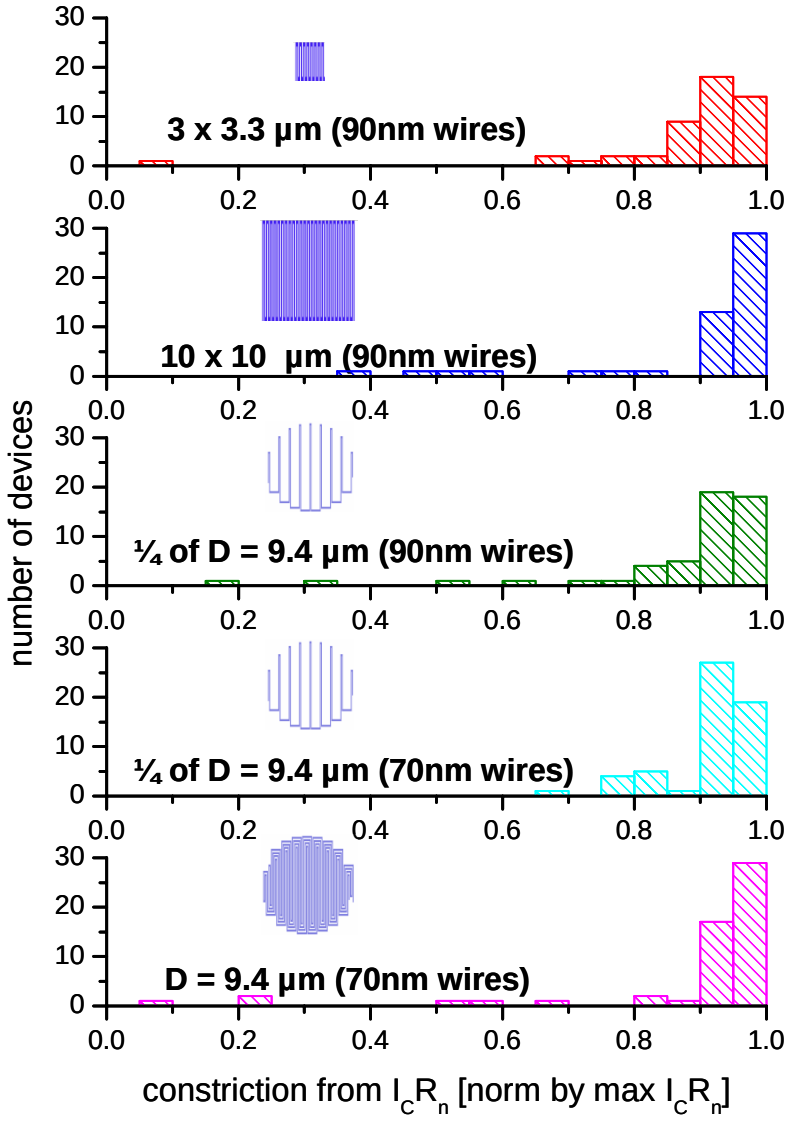

Figure 3.8: Histogram of measured values for the product of I_c and R_n for SNSPDs fabricated on NbN films deposited at MIT Lincoln Laboratory. The values in the histogram were normalized by the highest measured value of $I_c \times R_n$ (i.e. max(C)=1). The insets show the layout and size of the nanowires from which the data was obtained, with the histograms from top to bottom measured on: red=~50 µm long nanowires, blue=~500 µm long nanowires, green=~108 µm long nanowires, cyan=~124 µm long nanowires and magenta=~496 µm long nanowires. The histograms indicate that the probability of a nanowire being constricted was not measurably dependent on the nanowire length and constrictions were much less of a problem than for the detectors, particularly the large area SNSPDs, represented in Fig. 3.7.

3.2.4 Consequences of high-yield SNSPDs

This high-yield process for SNSPDs with high device detection efficiency permits a range of new possibilities. First, and perhaps most obvious, producing single detectors with high yield was a critical step to being able to produce reasonable size arrays of SNSPDs. The defect density demonstrated in this section should already be sufficient for applications requiring a high median or mean detection efficiency, but not necessarily 100% yield of all pixels. Second, larger area detectors can now be considered for applications that do not require the fastest possible reset times. One advantage of multi-element detectors, described in chapter 2, was the ability to mitigate high defect densities by allowing the multi-element detection efficiency to approach the average efficiency of its small-area-SNSPD elements, as opposed to being limited by the largest defect anywhere in the active area. With a lower defect density, it would be possible to consider using single-element detectors to obtain high system detection efficiencies.

Chapter 4

Two element SNSPD – Initial Demonstration and Performance Advantages

As discussed in chapter 2, an array of superconducting nanowire single photon detectors (SNSPDs) may take many forms in terms of the geometry and spacing of the nanowire elements. Initially, however, the basic idea needed to be tested using a design with minimal complexity, so that insight could be gained into the limitations of the approach before designing complex new packaging, readout and data processing capabilities. A reasonable compromise between discrete, widely-separated nanowire elements and fully intertwined, closely-spaced nanowires was a linear array of self-contained (not intertwined) nanowire elements that were closely-spaced to form a continuous active area. This design allowed the key feature of the multi-element SNSPD concept – closely-spaced, but independent nanowire elements forming a continuous active area – to be tested with only moderate potential for interaction between the elements – due to the fact there were only two elements and close proximity between nanowires occurred along only a short portion of their full length. This chapter will focus on the testing procedures and measurement results for a two-element SNSPDs with 2.3 μm ×4 μm elements, arranged to form a continuous 4.7 μm ×4 μm active area, which were published in Ref. 8. The results from these measurements indicated that the multi-element SNSPD concept was very promising and also served to guide the subsequent research, both in terms of feasible multi-element geometries and the potential issues that required more detailed investigation.

(a) (b)

Figure 4.1: Schematic of the layout of the (a) two-element SNSPD and (b) the two-element SNSPD connected to the contact pads. The coloring indicates the features corresponding to the bottom (blue) NbN element, top (red) NbN element, the shared NbN connection to ground (green), non-electrically connected NbN elements (black) used to mitigate proximity effects in the electron beam patterning of the device and the Ti/Au contact pads (yellow).

4.1 Two-element SNSPD design and fabrication

The design of an initial two-element SNSPD required considering both the key features of multi-element SNSPDs that the detector would be used to investigate as well as more general SNSPD requirements and limitations. The key multi-element design feature was the narrow spacing between nanowires, whereby the elements combined to form a continuous active area nearly identical to that of a similarly-sized, single-element SNSPD. This could be accomplished with minimal potential for interaction between the devices by arranging two meander-style SNSPD elements side-by-side, with the nanowires bordering on a single edge and spaced apart by the same gap as that separating the segments of the nanowire within a meander (Fig. 4.1(a)).

4.1.1 Two-element SNSPD design

The general SNSPD features were discussed in chapter 1: efficient SNSPDs could be made using ~4 nm thick (300 – 500 Ω/□) NbN patterned into 100 nm (or narrower) wires. A NbN nanowire of these dimensions needed to be at least 20 μm long in order to prevent a stable normal region

from developing in the nanowire after a photon detection event (at bias currents less than the critical current of the wire) [23-24]. Furthermore, longer nanowires had an increased probability of a defect, or constriction, limiting their critical current and detection efficiency [33], and were therefore avoided.

Although the general concept of these length limitations was understood during the design of the two-element detector, the quantitative details were not. Therefore, the most prudent course of action was to closely match each of the design parameters to those from a successfully demonstrated single element SNSPD. The highest detection efficiencies had been achieved using a ~4 nm thick, ~100 nm wide NbN wire patterned on 200 nm pitch to cover a 3.3 μm×3 μm area (total wire length of 51 μm). Thus, the two-element detector elements were designed with the same wire width and pitch to cover an area of 2.3 μm×4 μm each (total length of 48 μm each), as shown in Fig. 4.1(a).

4.1.2 Two-element SNSPD fabrication

The detectors were patterned using the process described in chapter 3 from superconducting NbN films deposited at Moscow State Pedagogical University. The films had a nominal thickness of 4 nm, typical room temperature resistivities of 300 – 400 Ω/□ and critical temperatures (temperature at the midpoint of the resistance between the normal and superconducting state) between 10 K and 11 K [81]. The films were diced into square chips 8 mm on a side with a layer of photoresist protecting the NbN surface, which was face down on the dicing tape. After dicing, the chips were removed from the dicing tape in acetone, and subsequently cleaned using a cleanroom swab to rub the surface first with acetone, followed by drying with nitrogen, and finally the surface was rubbed a second time using a cleanroom swab with deionized water. After the cleaning process, few particulates (~$10/\text{mm}^2$ or less) could be seen on the center portion of the chip when viewed using a 10x objective in an optical microscope. Contact pads consisting of 10 nm of Ti beneath 50 nm of Au were added using the standard photolithography and liftoff process described in chapter 3. The contact pads used for these devices consisted of two ~100 μm-on-a-side signal pads separated by ~50 micrometers from the surrounding ground plane (Fig. 4.1(b)). Given that the maximum frequency of interest

from the devices was a few GHz, the exact shape of the signal pads and the placement of the devices were not critical – the device and contact appear electrically as a lumped element.

Finally, the nanowires were patterned in resist using electron-beam lithography, and this pattern was transferred into the NbN using reactive ion etching. After fabricating the contact pads, the chip was dipped in 25% tetramethylammonium hydroxide (TMAH) for 4 min. Within 10 min of the TMAH cleaning step, hydrogen silsesquioxane (HSQ) resist was spun onto the surface of the chip. The TMAH cleaning step was required to remove contaminates that would be attacked during the development process and could prevent adhesion of the HSQ to the NbN. The HSQ resist was a 1:1 dilution of FOx-12 (Dow Corning) and methyl isobutyl ketone and was spun to a thickness of 90 - 100 nm at a speed of ~ 4.5 krpm. The chip was then baked at 90ºC for 3 min in order to evaporate any remaining solvent. The resist was patterned using a Raith 150 electron-beam lithography tool with an accelerating voltage of 30 keV and an aperture size of 20 μm. The dose of different features was varied in order to minimize proximity effect, with a dose of ~ 480 $\mu C/cm^2$ being used to expose the 100 nm wide lines with 200 nm pitch, selected based on a dose matrix imaged prior to the exposing the patterns on the final chip. The selected dose was ~ 10% lower than the dose at which appreciable footing could be observed at the bends of the meanders. The resist was developed in 25% TMAH for 4 min within several hours of exposure. Optical microscopy and scanning-electron microscopy were used to verify that the patterned HSQ had adhered well to the NbN, was correctly dosed and had sharply defined edges (i.e. the electron beam was in focus) at the corners and at several additional points across the chip (Fig. 4.2). Finally, the NbN was etched using CF_4 gas in a reactive ion etching process (see chapter 3 for details) for 2 min to remove the NbN not protected by the HSQ or the contact pads. After etching, the devices were ready for testing.

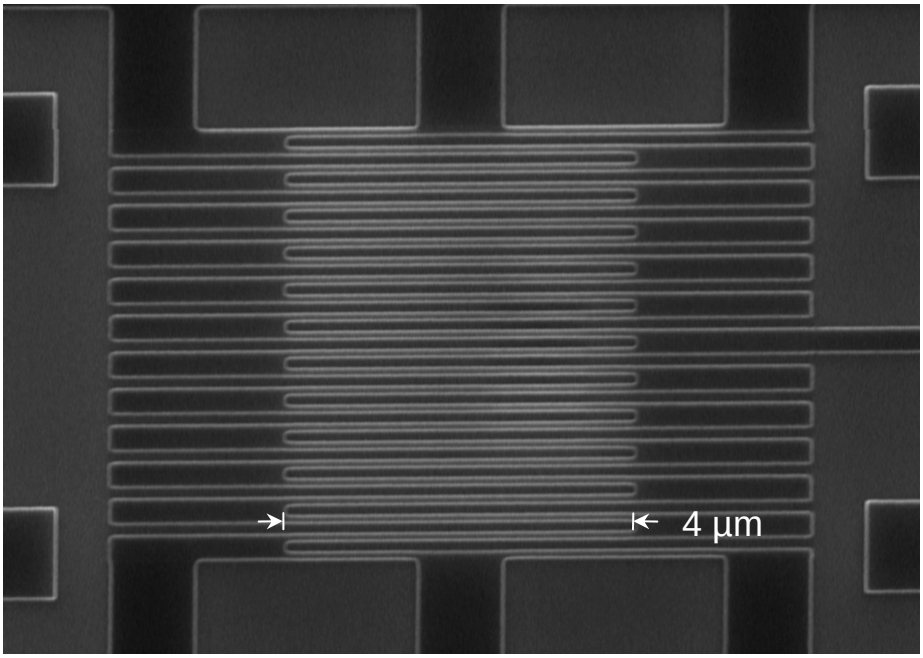

Figure 4.2: Scanning-electron micrograph of the patterned HSQ resist on top of NbN after development, but before etching. Note that the edges of the features appear sharp, with no contamination or footing visible.

4.2 Measurement setup

Testing the two-element SNSPD required the ability to independently readout and bias each of the elements, as well as the ability to optically illuminate the detector area, while maintaining the temperature of the device at 4.2 K or lower. Although the details of these electrical and optical connections might have been important, the flexibility to make many measurements and to try different optical and electrical arrangements was viewed as more important during initial testing than optimizing a package for long-term use. Consequently, the tests were performed using a cryogenic probing station in which electrical connections to the devices were made through two radio-frequency (RF) probes (Fig. 4.3) and optical illumination was provided by a fiber and lens assembly attached to a third probe [6-8]. Each of the probes could be micro-manipulated with < 1 µm resolution in all three linear coordinates relative to the detector chip, with sufficient range to address any point on the chip. The layout of contact pads on the SNSPD chip and the chip's orientation in the probing station were chosen to allow the two RF probes to independently

connect to the two nanowire elements (Fig. 4.3(a)) and to allow optical illumination through the sapphire substrate. Measurements in the probing station allowed many devices to be tested in quick succession, and basic device properties, such as critical currents, to be quickly measured in order to determine the repeatability of various measurements. However, this setup did restrict measurement times to ~10 hours (overnight data collection was not possible) and prevented accurate dark count measurements due to the inability to filter blackbody radiation transmitted through the openings in which the probes were translated.

4.2.1 Electrical components of the measurement setup and detector circuit

The electrical connections to the two-element SNSPD were made through two independent, but identical circuits as shown in Fig. 4.3. Each device was connected to a 50 Ω transmission line through a RF probe. The end of this transmission line was connected to a bias "T" (Picosecond Pulse Labs 5575A), with the DC port connected to a current source and the AC port connected to an amplifier chain and the data collection electronics. The current source was composed of a 100 kΩ resistor in series with an isolated, battery-powered, voltage source (SRS SIM928). This arrangement allowed bias voltages of a few volts (which could be easily sourced and adjusted with millivolt resolution) to supply the device with the desired few tens of microamperes of current, while appearing to the device like a stiff current source. The amplifier chain consisted of a 3 dB attenuator ("T" style RF attenuator), two wideband, low-noise amplifiers (Miteq JS2-00100400-10-10A), and finally a DC block (Inmet 8039) in order to limit noise thought to be due to a ground loop when the amplifier chain was directly connected to the oscilloscope or counter. The independent amplifier chains from each of the detector elements were connected to separate channels of an oscilloscope and frequency counter, as will be discussed in detail in section 4.2.3.

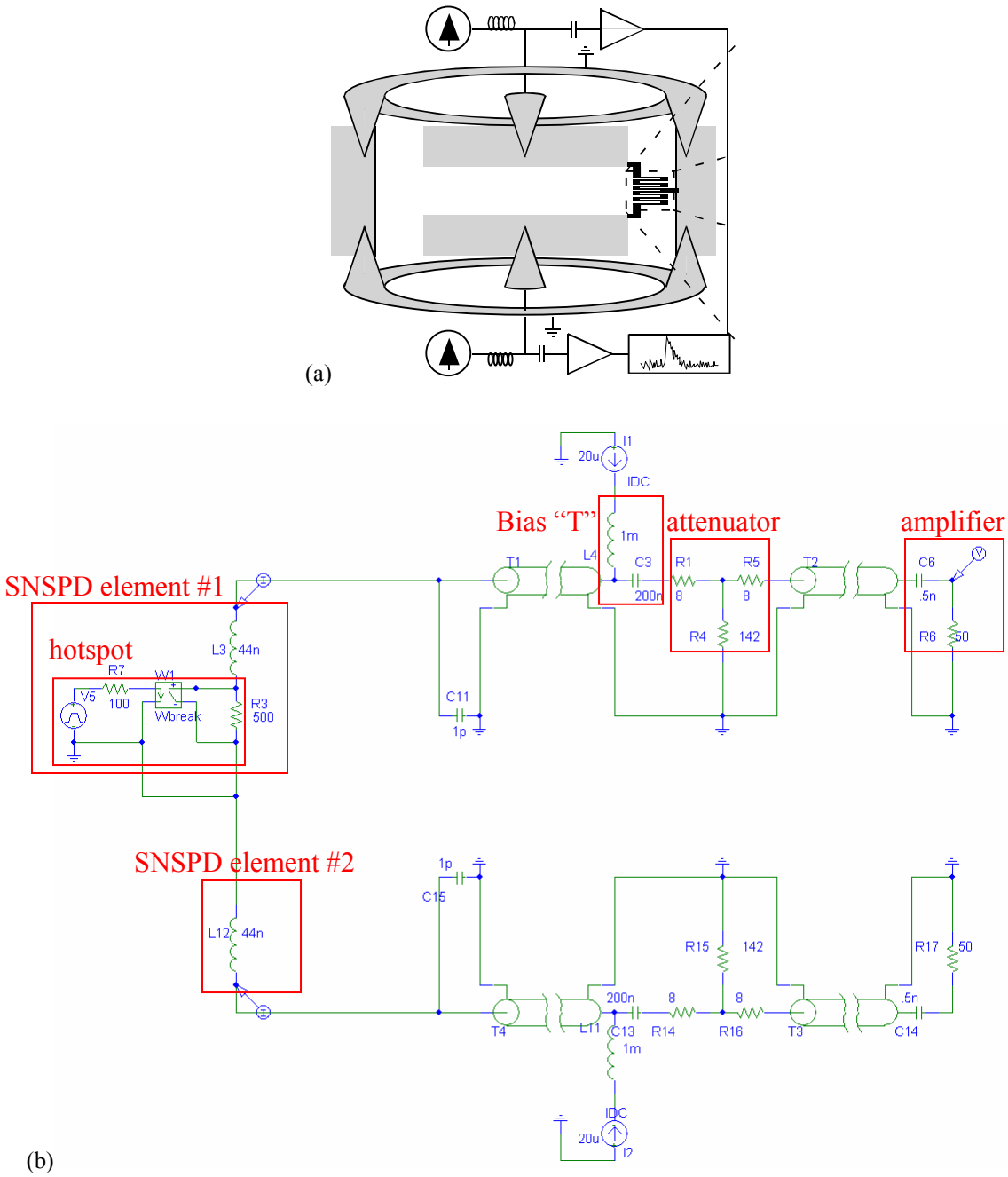

Figure 4.3: Schematic of the layout of (a) the overall electrical components and (b) the detailed electrical circuit elements. In the electrical circuit model, only SNSPD element #1 had a periodically forming hotspot, while SNSPD element #2 was always superconducting.

4.2.2 Optical components of the measurement setup

Fig. 4.4 illustrates two different sources of optical illumination were used for testing the device: a short-pulse, passively mode-locked fiber laser and an externally-modulated, continuous-wave (CW) laser diode. The wavelength of both sources was 1550 nm (± 10 nm), but they differed in terms of their pulse duration and the ability to control the timing of the pulses.

The passively mode-locked fiber laser provided optical pulses less than 1 ps in duration at a constant ~ 10 MHz repetition frequency. The duration of these pulses was much shorter than the timing jitter of the detectors and electronics, such that all of the photons in a pulse could be approximated as arriving simultaneously and the timing jitter in the arrival time of output pulses was only due to the detectors and electronics. Furthermore, the light emitted during the pulse periods was several orders of magnitude higher than total emitted during the periods between pulses, so the energy per pulse, E_p, could be accurately calculated by measuring the total power, P, and using the simple relation $E_p = P/10^7$, where $10^7\ s^{-1}$ was the repetition frequency of the laser. The frequency of the laser was sufficiently low to allow full recovery of the detector

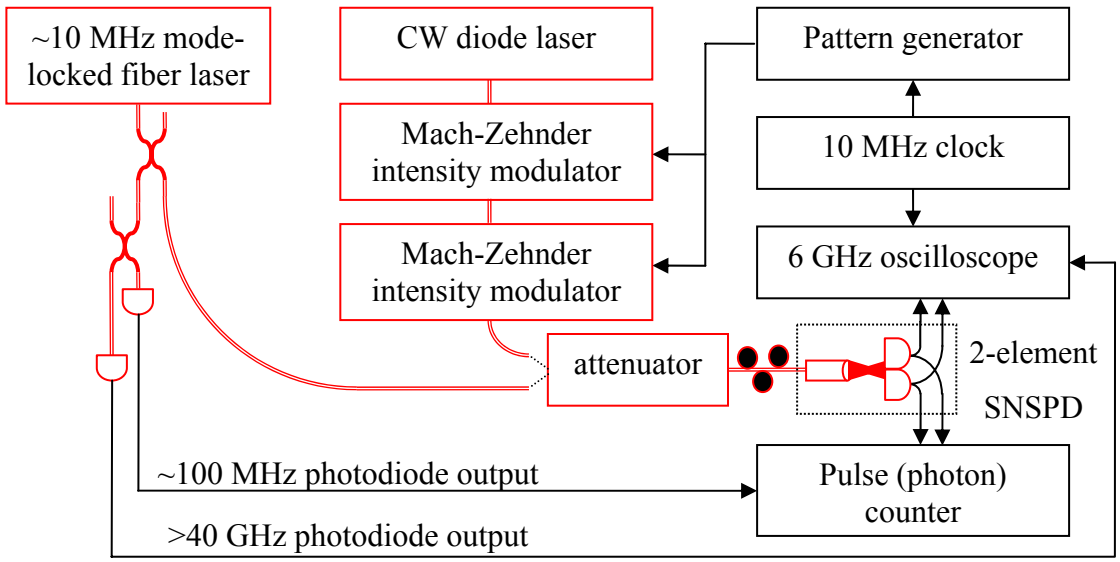

Figure 4.4: Schematic of the layout of optical and data collection components in the measurement setup. The optical and opto-electronic components are outlined in red, while the purely electrical components and cables are outlined in black.

elements between pulses, but because the frequency was fixed, the reset properties of the detector could not be probed without splitting a portion of the beam, delaying this second pulse by a variable time, and recombining the two pulses. Measuring the reset properties of the detector over a ~10 ns range required a wide variation in path length, and consequently calibration of the energy in the second pulse as a function of delay.

Instead of attempting to split and delay optical pulses from the mode-locked fiber laser, a simpler approach was taken for generating two optical pulses separated in time using a CW laser diode that was externally modulated using a pair of Mach-Zehnder intensity modulators. The modulators were arranged in series optically and were driven by an electrical pattern generator. In this way, an electrical pattern of two pulses with variable delay in the range of 0.2 to 10 ns between them could be digitally generated and used to create two optical pulses. The energy in the second pulse was sufficiently independent of the delay between the pulses to eliminate the need for the delay-dependent energy to be calibrated. The rate of the pattern generator could be user-defined, and was set to 50 MHz to ensure the detectors had time to reset between optical pulse pairs. The bandwidth of the pattern generator, drive electronics and intensity modulator limited the optical pulses to ~100 ps in duration. While this was more than sufficient for measuring the reset properties of the detectors, this pulse duration was too long to accurately measure timing jitter and this optical source was only used in the reset time measurements.

Before coupling the light from either source into the probing station, this light was sent through a carefully calibrated, computer-controlled optical attenuator and a manual polarization controller (Fig. 4.4). All of the optical components following the sources themselves used SMF-28 fiber, which was single mode at 1550 nm wavelength. The optical attenuator could be used to reduce the optical power by a factor up to 10^{10}, although the attenuation factor was typically between 10^6 and 10^8. The polarization controller could be used to correct for any rotation of polarization between the light source and the detector. The polarization was typically (always, in the case of peak detection efficiency measurements) optimized to maximize the detector count rate. An SMF-28 fiber was also used to couple light into the probing station. The end of the fiber in the probing station was epoxied into one end of a stainless steel ferrule with a lens epoxied onto the other end. This assembly was manufactured by OZ Optics, with a hole in the

ferrule to allow the pressure inside to adjust between atmosphere and vacuum, and epoxy that had withstood repeated thermal cycling to cryogenic temperatures. The lens assembly was installed at the end of a micro-manipulated probe cooled to $< 18\,\mathrm{K}$ through copper braids. The focal length of the lens and the distance to the fiber were selected to provide a $\sim 25\,\mu\mathrm{m}$ $1/e^2$ diameter, although this spot size required in-situ recalibration in order to account for thermal contraction during cooling. This calibration was performed during every cooldown during which calibrated detection efficiencies were measured by recording the count rate as a function of the probe position and deconvolving the size of the detector from the resultant profile. The measured $1/e^2$ diameter was $25\,\mu\mathrm{m}$ ($\pm 2\,\mu\mathrm{m}$), providing a spot size considerably larger than the detector area and a depth of focus of $\sim 350\,\mu\mathrm{m}$, reducing the alignment tolerances and the sensitivity of coupled power to small vibrations. At the same time, the spot size was small enough to limit the total optical power – even a 0.1% efficient device, with small $(3\,\mu\mathrm{m})^2$ area, illuminated with enough light to generate 300 Mc/s requires only $3\,\mu\mathrm{W}$ total optical power – to levels easily achieved with the optical sources and easily absorbed by the cold head without raising the base temperature.

Finally, the laser pulses must be synchronized with the data-collection electronics. In the case of the mode-locked fiber laser, this was accomplished by splitting off a fraction of the light before the optical attenuator that was split a second time and coupled into a $> 40\,\mathrm{GHz}$ photodiode (New Focus 1024) and a $\sim 100\,\mathrm{MHz}$ photodiode (Thorlabs DET410). The electrical output of the high-speed photodiode was used as a trigger input for an oscilloscope, while the electrical output from the low-speed photodiode was used to trigger an electrical pulse counter. Only the oscilloscope was used to make precise timing measurements, and the timing jitter of the low-speed photodiode output needed to be only $\sim 1\,\mathrm{ns}$, which was easily achieved. The externally-modulated laser diode was synchronized to the oscilloscope used to collect the data by connecting the same 10 MHz reference clock to both the electrical pattern generator and the oscilloscope. This ensured that the analog-to-digital converters in the oscilloscope were always measuring the detector output signals at the same points relative to the optical signal. An output from the pattern generator was used to provide a trigger input to the oscilloscope.

4.2.3 Data collection components of the measurement setup

The data for the measurements of the two-element SNSPDs was collected using a 6 GHz real-time oscilloscope (Lecroy WaveMaster 8600A), and an electrical counter (SRS SR400) was also used to measure the detector count rates. The oscilloscope allowed the analog output signal from the detectors to be viewed and manipulated directly, and allowed most of the data processing to be performed during the measurement, providing very rapid feedback. In this way, the effect of any changes to the setup could be seen immediately – any oscillations of the amplifiers due to improper landing of the electrical probes on the contact pads could be corrected and the threshold levels could be seen visually to ensure their proper selection.

The oscilloscope could be set up to make several different measurements. The most general measurement was to record the analog output traces within a particular time window relative to a trigger. The time window used for these measurements was only as long as required for the data analysis in order to limit the data that needed to be stored. This stored data could then be post-processed in order to extract the timing of the output pulses. This approach was only used in the case of measuring the reset properties of the detector, to give maximum flexibility and control over extracting output pulses closely spaced in time. For all other measurements, the oscilloscope recorded the number of front edges (pulses) crossing a user-defined threshold within a specified time window relative to the trigger. In the case of the timing jitter measurements, the specified time window was sub-divided into narrow time bins and the oscilloscope recorded a histogram of counts versus pulse arrival time. In the case of the detection efficiency and crosstalk measurements, the counts were recorded for only a single, 1 ns-wide time bin centered at the time of peak counts found in the timing jitter histograms. This 1 ns-wide time bin was sufficiently wide to capture all of the detection events from the incident light and a negligible number of background counts.

While the oscilloscope was triggered by the optical source in the case of measuring a single detector element, many of the two-element measurements required triggering on the second detector element. The trigger input to the oscilloscope determined when an event on the input channel was recorded and analyzed, so the measurement of a detector element *A* on

channel 1 of the oscilloscope was independent of whether detector element *B* registered a count if the oscilloscope was triggered by the optical source. However, using the output of detector element *B* to trigger the oscilloscopes allowed a conditional measurement to be made: the measurement of the output from detector element *A* was conditioned on the detection of a count in detector element *B*. Thus, the conditional measurements were made simply by connecting the second detector output to the oscilloscope trigger input and appropriately setting the threshold and timing window (ensuring that the timing window did indeed correspond to the first detector output coincident with the second detector trigger).

4.3 Interactions between elements

With the two-element detector described in section 4.1 and the measurement setup described in section 4.2, potential interactions between elements could be investigated and performance advantages of the two-element SNSPD could be characterized. Crosstalk, in which one detector firing would affect the adjacent element, might have occurred due to coupling of electromagnetic fields or the generation of phonons during a detection event. It was possible this crosstalk could affect the timing jitter (section 4.3.1) by changing the speed with which the adjacent detector fired or the detection efficiency (section 4.3.2) by changing the probability that the adjacent detector switched. A subtle increase in the probability that the adjacent detector fired might have been seen only when the detector was counting random noise or CW light (section 4.3.3), because it was far less likely both detector elements would have fire simultaneously due two incident photons from a CW source then would be the case with pulsed light.

Before making careful measurements of these potential interactions, the timescale over which such crosstalk might occur must first be considered. Some level of interaction might have occurred over infinitely long timescales, due to a finite decrease in the critical current of a nanowire when an adjacent wire was biased. To check this, the bias currents in both detector elements were adjusted and it was found that the critical current for a given element did not change measurably as the current in the adjacent element was adjusted over the range in which it remained superconducting. When the critical current was exceeded and heat was continually

dissipated in one of the nanowires, the critical current of the adjacent nanowire decreased by more than 10%, which was likely due to local heating. The measurements discussed in the remainder of this chapter were made with both elements in the superconducting state, biased at approximately 95% of their respective critical currents, except where otherwise noted. Given that the critical currents of the nanowires were not measurably affected when both were superconducting, it was not likely the wires were interacting in steady state.

The other timescale of importance was short – no more than ~1 ns. The reason only short time scales were of interest was because the duration of the optical pulse was in the range of 1 – 100 ps, the thermal time constants were known to be < 100 ps [83], the entire process of the wire switching from superconducting to normal and back was a few hundred picoseconds [6], and the propagation time of electromagnetic radiation and phonons across the entire detector length were tens of femtoseconds and hundreds of picoseconds respectively [84]. The only time constants longer than 1 nanosecond were the full recovery of current through the device and reflections or electrical interactions from the electronics outside the probing station. In both cases, such interactions were not direct crosstalk between detector elements, and will be considered in chapter 6. Instead, this section will focus on measuring the level of direct interactions (i.e. on timescales < 1 ns) between detector elements.

4.3.1 Timing jitter

The first type of interaction to investigate was the timing, because we needed to determine the relative time delays from the outputs of the two detectors in order to investigate other types of potential interactions over the short time scales at which we expected they would occur. Before looking at the output from both detectors firing simultaneously, we looked at each detector output independently. The front edge of one detector element's output signal was used to trigger the oscilloscope and the timing of the front edge of the photodiode output was measured. This allowed the timing jitter of each element's output to be measured, as the timing jitter of the photodiode output was negligibly small. This measurement was repeated for each of the two detector outputs and the obtained histograms (Fig. 4.5 (a, b)) showed that the two detector

elements each had a timing jitter of 29 ps FWHM, which was the same as the timing jitter measured for a single-element SNSPD.

Next, the relative timing jitter of the two detector elements needed to be measured in order to look for unexpected interactions. For this measurement, the oscilloscope continued to be triggered by the front edge of one detector element's output while the timing to the front edge of the second element's output signal was measured. The histogram of this relative timing jitter is shown in Fig. 4.5 (c). This timing jitter closely matched the prediction based on the convolution of the timing jitter measured for each element independently.

These measurements have only examined the case of timing jitter between simultaneously incident photons, and not between photons separated by tens to hundreds of picoseconds, when some of the potential interactions described above would have occurred. This shortcoming will be partially addressed in chapter 5, when photons spaced by ~ 100 ps in time will be examined, but even the measurement of simultaneously-incident photons provided more insight than might initially be assumed. The full detection process, which governed the shape and timing of the front edge of the output pulse, occurred over a > 100 ps timescale and

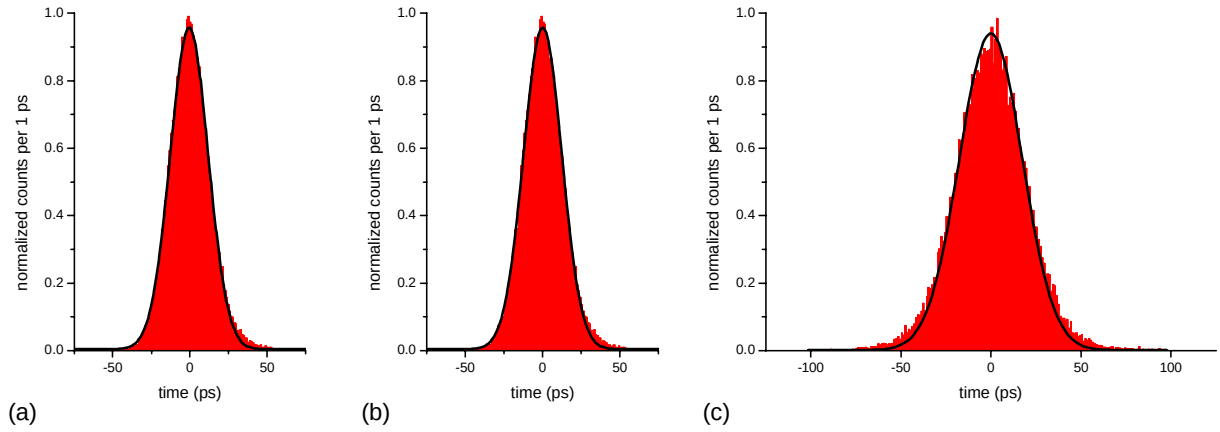

Figure 4.5: (a) and (b) Histogram of the timing jitter of each detector element measured relative to the illuminating optical pulse and a Gaussian fit (line) showing 29 ps FWHM timing jitter; (c) histogram of the timing jitter of one detector measured relative to the adjacent detector and a Gaussian (line) calculated by convolving the fits from (a) and (b), demonstrating that the timing jitter from each element was essentially uncorrelated during a two-photon detection event.

was likely to be susceptible to any interactions that would have affected detection events occurring with small delays in time. Neither the single-element or relative timing jitter measurements showed any features (broadening, double peaks, etc.) that would have indicated such an interaction. Therefore, this measurement provided strong evidence that there was little to no dependence of the detector timing jitter on the presence of an adjacent element firing and that this was not a major concern for the multi-element SNSPD concept. Finally, the ~41 ps relative timing jitter between coincidence photon count events was believed to be the best demonstrated for a pair of single photon detectors, demonstrating the potential of this approach for precise timing of multiple photons.

4.3.2 Detection efficiency

Next, the detection efficiency of the devices was measured to look for evidence of an interaction between the device elements that altered the detection probability. The optical and electrical setup used to measure the detection efficiency was the same as that used to measure the timing jitter except for the way the oscilloscope data was analyzed. First, only one of the detector elements was biased at various critical currents while the other element was left unbiased. The oscilloscope was triggered using the photodiode output and the detector element's output was connected to an input oscilloscope channel. The detection efficiency was measured by comparing the number of detection pulses in a 1 ns time period, centered to capture detection events from the optical pulses, to the total number of trigger events. Second, the adjacent detector element was biased at 95% of its critical current and the oscilloscope was triggered by its output. The detection efficiency of the first detector element was again measured by comparing the number of detection pulses in a 1 ns time period to the number of trigger events, which in this case restricted the measurement to only those optical pulses from which a photon was detected by the adjacent element. Thus, the detection efficiency without the adjacent detector element biased can be compared to the detection efficiency conditioned on the adjacent element firing. Fig. 4.6 shows both of these measured detection efficiencies. There was no statistically significant difference between the detection efficiency measured with and without the adjacent element biased. However, this measurement was only a good way of investigating

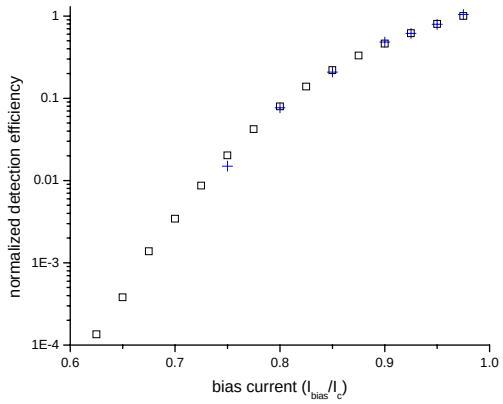

Figure 4.6: Normalized detection efficiency of a single detector element measured with the adjacent element unbiased (open squares) and conditioned on the adjacent element firing (blue crosses). A single factor, one over the detection efficiency at $I=I_c \times 0.975$ with the adjacent element unbiased, was used to normalize both data sets.

high levels of crosstalk, because there was a high probability the adjacent detector would switch due to a photon in the same optical pulse and this large coincidence count rate would have dominated over any small crosstalk rate.

4.3.3 Crosstalk from random noise counts

A more quantitative study of crosstalk and detection efficiency variations than the approach described in section 4.3.2 could be made using a non-pulsed light source. In this case, the laser input to the device was blocked and the electrical arrangement was identical to that used to measure the relative timing jitter. The detector elements were illuminated with low-intensity light from an incandescent lamp that had constant intensity and could be well approximated by Poisson statistics. Although thermal light emission is not a Poisson process, the broadband spectrum of thermal light used in this experiment resulted in a very short coherence time, and the expected average number of coincidence detection events in a 1 ns timing window could be accurately calculated by assuming that the second-order temporal intensity correlation function was constant. Temporal intensity correlation functions and their connection to crosstalk measurements will be discussed in more detail in chapter 6.

To look for crosstalk, the background light counts from one detector element were used to trigger the oscilloscope and the number of coincident noise counts from the second element was measured. The intensity of the background light was adjusted such that the count rate in the second detector was ~100 kHz, a reasonable counting rate that minimizes the probability of detection events being blocked by periods in which the detector was resetting while maintaining a reasonable data collection rate. An output pulse from the second element was considered coincident whenever it occurred within a 1 ns time period, centered on the timing of coincident events as determined from the relative timing jitter measurement using a pulsed source. After 750,000 detection events in the element used to trigger the measurement, 80 coincident detection events were observed in the adjacent detector element. If the counts in the second detector were uncorrelated to those in the triggering detector, 75 coincident detection events would be expected within 750,000 1 ns time windows (750,000 single events × 100,000 uncorrelated events/second × 10^{-9} seconds per coincidence bin = 75 expected coincidence events). If we assume the primary source of noise in the measurement was statistical noise in the number of coincidence events, the uncertainty in the measurement was $\sqrt{80} \approx 9$. Therefore, the measured crosstalk, 0.0007% (±0.0012%), was within the noise of the measurement.

However, as with the timing jitter measurement, several limitations of this crosstalk measurement should be noted. The primary limitation to the measurement was the triggering and processing speed of the oscilloscope, which prevented much larger amounts of data from being processed. At the counting rates considered, this limited the number of coincidence counts, and resulted in a relatively large uncertainty in the measurement relative to the measured crosstalk. Ideally, enough data should have been collected in order to measure a non-zero crosstalk that was larger than the measurement uncertainty. Additionally, this measurement was limited to reasonably high counting rates, in order to collect a non-zero number of coincidences. At lower counting rates, the crosstalk was likely to have contributed a larger fraction of the total coincidences, and is an important operating region to consider. Finally, the visible-wavelength photons used to illuminate the detectors (from a lamp filtered by the probing station cold window), were absorbed with a detection efficiency that was less sensitive to fluctuations in the current or other interactions between the nanowires. Ultimately, crosstalk should be examined

over a wider range of operating parameters and with a data collection system that can collect and process the detection events more efficiently. These measurements do, however, demonstrate the potential for multi-element SNSPDs to have low crosstalk, and more detailed measurements will be investigated in chapter 6.

4.4 Two-element SNSPD performance benefits

In addition to investigating potential crosstalk, it was also useful to investigate the improved capabilities provided by a two-element SNSPD. Even with only two elements, the maximum count rate was substantially increased and dead-time effects could be partially overcome (section 4.4.1). Furthermore, the two elements introduced the possibility of resolving two photons simultaneously (section 4.4.2), a first step toward achieving photon-number-resolution. Given that it was these performance benefits that first motivated exploring multi-element detectors, it was critical to determine the degree to which the two-element detector could provide these capabilities and what changes to the detector or measurement setup needed to be made in the future.

4.4.1 Reduced reset time

Spreading an optical beam across a two-element SNSPD could provide a higher maximum counting rate for a detector with a given active area. This increased counting rate comes from two sources, the faster reset time of the shorter elements relative to a single element covering the same active area and due to the elements counting in parallel. This increase in the counting rate could be demonstrated by measuring the probability of detecting photons from a second optical pulse as a function of time after detecting the first pulse.

An externally modulated CW laser was used in which pulses with variable spacing in time were generated by controlling the electrical pattern sent from an electrical pattern generator to a pair of lithium niobate electro-optical modulators, as described in section 4.2.2. The optical intensity was adjusted such that each detector element had a ~13% probability of detecting an

optical pulse. In this way, the probability of detecting the second optical pulse was not substantially lower than the probability of detecting the first, regardless of the time between the optical pulses, because ~87% of the time the detector element did not fire on the first optical pulse and was thus fully recovered when the second photon was incident.

The electrical output from each detector element was sent to the oscilloscope and the traces from both elements' outputs were saved simultaneously. These traces were post-processed using Matlab in order to determine the marginal and joint probabilities of four events during each optical pulse pair: XY where $X = (A, B)$ identifies the detector element and $Y = (1, 2)$ identifies the first or second optical pulse in a pair [85]. Thus, for a given optical pulse pair, event $A1$ would denote detector A firing on the first optical pulse.

Using the event probabilities calculated from the recorded oscilloscope traces, we calculated the detection efficiency as a function of time following a detection event. We first calculated the probability of each detector element independently detecting a photon from the second optical pulse conditioned on measuring a photon from the first optical pulse. Normalizing this probability relative to the probability of detecting the second pulse when the detector was fully recovered, the probability for each detector X was: $P(X2 \mid X1) / P(X2 \mid \overline{X1})$. The normalized detection efficiency was calculated by averaging this probability over ~210,000 optical pulse pairs for each value of pulse separation and is shown as a function of the relative time between optical pulses for one of the detector elements in Fig. 4.7 (red open squares). It is clearly seen that the probability of detecting both optical pulses with a single detector element becomes negligibly small when the optical pulses are closely spaced in time

However, the two-element detector did not have a negligible probability of detecting photons from two pulses closely spaced in time. The normalized probability of a photon from both optical pulses being detected by any combination of the two detector elements was given by: $P(A2 + B2 \mid A1 + B1) / P(A2 + B2 \mid \overline{A1 + B1})$. The normalized detection efficiencies calculated from this probability for the two-element detector are also shown in Fig. 5 (black filled squares) and the detection efficiency was ~50% when the two optical pulses were closely spaced in time. This 50% normalized detection efficiency occurred only in the low-flux limit, when it was

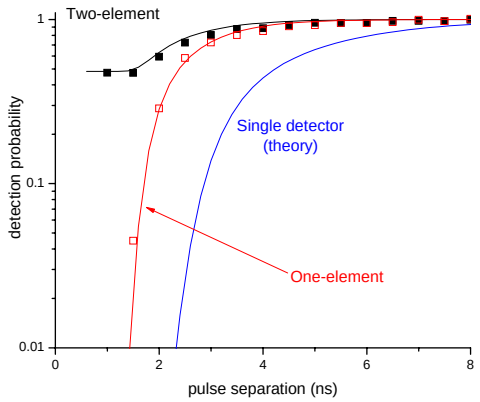

Figure 4.7: Normalized probability of detecting a photon from a second optical pulse conditioned on the detection of at least one photon from the first optical pulse as a function of the optical pulse separation. Data marked with red open squares were for one of the individual elements while the data marked with black closed squares was for the 2-element SNSPD. The measured inductance and detection efficiency versus bias current of the nanowires was used (see [6]) to calculate the expected recovery time for the two-element detector (black line), the single detector elements (red line), and a single detector with the same active area as the two-element detector (blue line).

unlikely that both detector elements would have fired on the first optical pulse. If only a single detector fired on the first pulse, the probability of detecting a photon from the second optical pulse was cut by the probability the second photon was incident on the same, then inactive, element.

The recovery of the detection efficiency following a detection event was also calculated using the measured inductance and detection efficiency versus current, as described in Ref. 6. The detection efficiency recovery for the two-element detector (black line in Fig. 4.7) was calculated assuming the second detector remains active 87% of the time, and needed to recover from simultaneously detecting a photon the remaining 13% of the time. The recovery of each independent element was also calculated and shown in Fig. 4.7 (red curve). Finally, the detection efficiency recovery time of a device with the same active area as the two-element device was calculated by assuming its inductance was the sum of the two individual elements' inductances (blue curve in Fig. 4.7), because the kinetic inductance dominated and was proportional to the length of the nanowire [6]. These curves in Fig. 4.7 clearly show that the counting rate of the two-element SNSPD is increased relative to a single SNSPD with the same

active area both by the fact that each element could count independently and due to the fact the kinetic inductance of each element was only half that of the entire nanowire.

4.4.2 Two-photon counting

A two-element SNSPD was sufficient to obtain limited photon-number resolution by spreading the optical beam evenly across both elements and recording whether both, one, or neither of the detector elements generated an output pulse at a given time. In order to characterize the two-element SNSPD's ability to resolve multiple photons, the probability that zero, one or two elements fire as a function of optical intensity was measured. The optical and electrical setup used to measure these probabilities was the same as that used to measure the timing jitter and detection efficiency, except that the photodiode output was used to trigger the oscilloscope and the number of detection events was extracted by adding the voltage levels from the output traces from each detector element after analog-to-digital conversion and then recording a histogram of the voltage heights at the time when a photon from the pulse would be detected. Although it would have been preferable to threshold each output signal separately and digitally add the number of detected photons if a large number of elements had been used, the signal to noise ratio of the summed output trace was sufficient to clearly distinguish zero, one and two detection events from the summed analog trace (Fig. 4.8(a)). The measured probability of detecting zero, one, or two detected photons as a function of optical intensity is shown in Fig. 4.8(b).

Additionally, two sets of theoretical curves are also shown in Fig. 4.8(b): dashed curves showing the expected probabilities of registering a count as a function of pulse energy for a two element array and solid curves showing the expected probabilities for an ideal photon-number-resolving detector with the same detection efficiency as the two-element SNSPD. The equations for generating these theoretical curves will be discussed in chapter 5. It should be noted that coherent optical radiation was used in both the measurements and theoretical curves, so non-unity detection efficiency scales the curves horizontally without changing their shape (i.e. shifting the curves on the logarithmic axis used in Fig. 4.8(b)). Although, the detection efficiency plays a crucial role in determining the fidelity with which any photon counter can measure the number of incident photons, Fig. 4.8(b) is intended to highlight the penalty

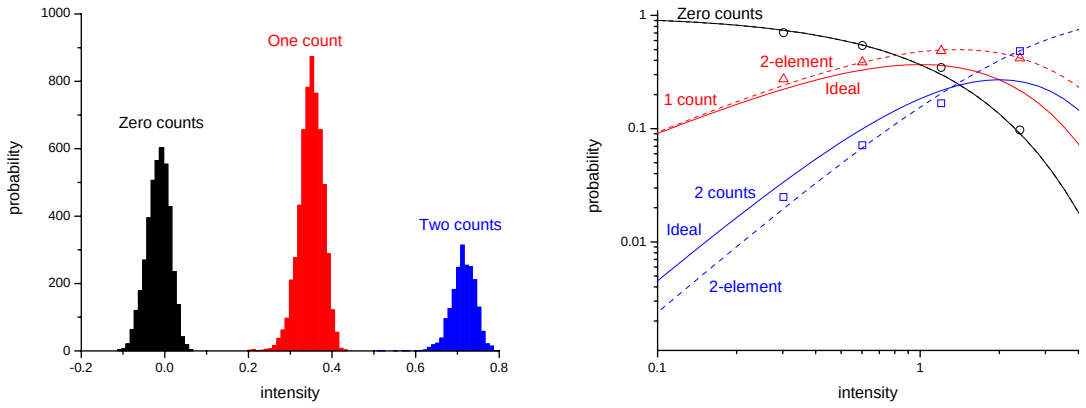

(a) (b)

Figure 4.8: (a) The histogram of voltages measured from the summed analog output signal showing the excellent SNR for distinguishing zero, one, and two detected photons. (b) Theoretical probability of detecting zero, one, or two photons as a function of optical intensity using a two-element single-photon detector (dashed lines) and an ideal photon-number-resolving detector (solid lines). The two-element detection probabilities vary by ~3 dB from the ideal detection probabilities for intensities < 2.5 photons. The measured probabilities of detecting zero (black circles), one (red triangles), or two (blue squares) photons are also shown.

associated with using a two-element SNSPD. MESNSPDs with a larger number of elements may be required to reduce this penalty to an acceptable level for some applications, although the SNSPD detection efficiency will quickly become the dominant limitation to achieving high fidelity.

4.5 Two-element SNSPD summary

The measurements of both potential interactions between elements and the performance benefits of the two-element SNSPD were very encouraging and in good agreement with expectations for two independent elements. The fact that any interactions between elements were below the levels measurable in the experiments indicates that it was reasonable to pursue multi-element detector layouts in which the nanowires would be intertwined and have the potential for interactions along their entire length. Furthermore, the two-element results suggested that using

more elements would have provided additional benefits, particularly for measuring the number of simultaneously incident photons. This approach will be explored in chapters 5 and 6.

Although the two-element measurements demonstrated the potential of the multi-element concept, there remain a number of issues that have not been fully resolved. First, the detection efficiency of the demonstrated two-element detectors was not as high as other similar area detectors fabricated using the same process. It was certainly possible, particularly given that all of the two-element devices tested were from a single chip, that the superconducting film or fabrication differed in some way from those that yielded the best demonstrated devices. In fact, inconsistencies of this magnitude were often seen in the measured detection efficiency between nominally identical devices on different chips. However, the detectors demonstrated in this chapter do not rule out the possibility that some unknown effect related to the multi-element design might also be contributing to the low detection efficiency. Secondly, the issue of crosstalk between elements should not be considered fully resolved because of the limited amount of data that was collected. A more accurate crosstalk measurement can be made both by measuring more data points (by using a faster data collection system that did not suffer from as long an electronic dead-time as the oscilloscope and by measuring over a longer period of time) and by operating the detector in a system with lower noise counts, which would allow even lower levels of crosstalk to be observed. The issue of multi-element detectors with high detection efficiency will be discussed in chapter 5, while crosstalk will be examined in chapter 6.

Chapter 5
Photon Number Resolution using a Multi-element SNSPD

The initial measurements of a two-element SNSPD described in chapter 5 demonstrated the potential for measuring multiple simultaneously incident photons, but the detector was limited to measuring at most two simultaneous photons with very low efficiency. In this chapter, we will examine the limitations from both the number of elements and the detection efficiency and will discuss efforts focused on optimizing a multi-element SNSPD for photon-number-resolution (PNR). The implemented changes – (1) increasing the number of detector elements from two to four, (2) ensuring that the light was split evenly between the detector elements, and (3) obtaining a high coupling efficiency and device detection efficiency – required changing both the design of the detector as well as its packaging. In addition to permitting PNR, the multi-element approach provided some useful advantages over single-element SNSPDs for obtaining high coupling and detection efficiencies. These efforts yielded a detector capable of individually timing up to four simultaneous photons with ~30 ps timing resolution and, with additional changes to the packaging, 46% system detection efficiency. Much of this work has also been published in Ref. 38.

5.1 Theory of photon-number-resolution with multiplexed detectors

The photon-number-resolution measurement fidelity will be examined for two reasons. First, the conditions under which this fidelity is limited by the finite number of elements, as opposed to the detection efficiency, should be calculated in order to determine when it is more important to

focus on increasing the number of elements versus increasing the detection efficiency. Second, the count statistics that would be expected from a spatially-multiplexed detector must be calculated in order to provide a way of evaluating the performance of the detector later in this chapter.

5.1.1 Photon-number-resolving fidelity limitations

Mathematically, the multi-element SNSPDs should have the same photon-number-resolving performance as any spatially-multiplexed arrangement of independent single-photon-sensitive detectors. This situation has been considered previously in Ref. 86, where the process of splitting the input and vacuum modes between multiple elements was described in terms of an N-port device (Fig. 5.1). Although no beamsplitter or additional vacuum modes were introduced in the case of the multi-element SNSPD, the calculations are unchanged by this distinction. The spatial multiplexing approach is useful for measuring photon number using single-photon-sensitive detectors, which are capable of detecting a single photon, but cannot resolve whether one or several photons are simultaneously incident. By splitting an input mode into several modes, each with much less than one photon on average, the number of simultaneous detector counts from each of the single-photon-sensitive elements can then be digitally added. In order for this approach to work well, the spatially-multiplexed detector must have: (1) vacuum modes at all inputs except for the one of interest, (2) enough detector elements that the probability of any detector having more than one photon is sufficiently low, (3) detectors with high-efficiency and (4) low-noise. In the analysis that follows, we will neglect noise in the detectors and assume vacuum modes at all inputs other than the one of interest, which closely approximates the measurement conditions described throughout this chapter.

The number of detector elements and the detection efficiency will both limit the fidelity of a photon-number measurement using the multi-element SNSPD, where the fidelity is defined to be the probability of measuring the correct number of photons. It is important to isolate each of these effects in order to determine the circumstances in which each is the dominant limitation. We will now show in the following section that by using only 4-elements, the achievable SNSPD detection efficiency is the dominant limitation to the fidelity of measurements of 1, 2, 3 or even 4

photons. The theory will also provide us with a method for evaluating the performance of the 4-element SNSPD and for predicting what improvements in the measurement fidelity may be expected by increasing the number of elements or improving the detection efficiency.

The probability of measuring the correct number of photons in a pulse with n photons, $P(n|n)$, has previously been found analytically for the case of equal splitting between N detector elements, each with the same detection efficiency η [87]:

$$P(n \mid n) = \frac{N!}{N^n (N-n)!} \eta^n \tag{5.1}$$

This expression was used to perform the calculations in the remainder of this section. In order to simplify the discussion, the detection efficiency will be defined to include all losses incurred in coupling the light onto the multi-element detector. The solution to Equation 5.1 is plotted as a function of detection efficiency and the number of detector elements, where Figure 5.1(a) shows the probability $P(2|2)$, Figure 5.1(b) shows the probability $P(3|3)$, and Figure 5.1(c) shows the probability $P(4|4)$.

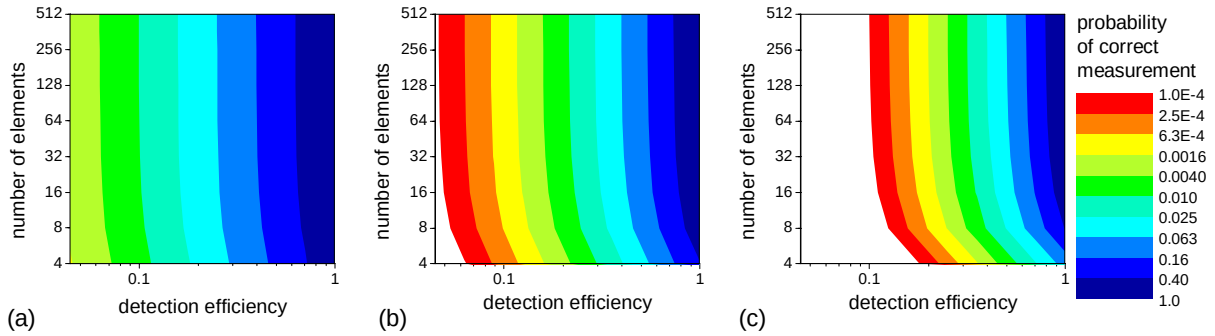

Figure 5.1: Calculated probabilities (a) $P(2|2)$, (b) $P(3|3)$, and (c) $P(4|4)$ for a spatial multiplexed detector plotted as a function of the number of elements and the detection efficiency, which is the same for all of the elements between which the light is equally split. Note that the contours of equal measurement fidelity are logarithmically spaced. In order to maximize the fidelity, the detection efficiency must be close to 1 and a large number of elements are required. Under those conditions, the fidelity is more sensitive to small fractional changes in the detection efficiency than the number of elements.

Both Equation 5.1 and Figure 5.1 illustrate that the measurement fidelity is scaled by a factor associated with the detection efficiency and that reduced detection efficiency rapidly degrades the multi-photon measurement fidelity. The measurement fidelity is also reduced by a fixed factor associated with the number of elements. In the case of measuring zero or one photon, the scale factor is unity, while for measuring more than N photons ($n > N$), where N is the number of elements, the scale factor is zero. Consequently, for a given number of elements, the fidelity for measuring N or fewer photons is limited primarily by the detection efficiency, when this detection efficiency is low, and by the number of elements when the efficiency is high.

In order to quantify this effect, a parameter called penalty, or α, will be defined which is equal to the fidelity expressed in decibels. The fact that the terms containing the detection efficiency and the number of elements in Eq. 5.1 are separable allows us to easily compare the penalty from each. The penalty associated with the detection efficiency is simply $\alpha_{DE} = 10\log_{10}(\eta^n)$. Similarly, the penalty for using a finite number of elements, α_N, is the other factor in Eq. 5.1 expressed in decibels. Consequently, the total penalty is $\alpha = \alpha_{DE} + \alpha_N$. The penalty due to the number of elements for measuring one photon is always 0 dB, because the photon will be detected with the same probability regardless of the number of elements to which it is directed. For measuring two photons, the penalty is 1.25 dB (25%) for using $N = 4$ elements and only 0.28 dB (6.3%) for using $N = 16$ elements. Similarly, for measuring three photons, the penalty is 4.26 dB (62.5%) for using $N = 4$ elements and 0.86 dB (18%) for using $N = 16$ elements.

Although these penalties are significant, they must be compared to the penalties associated with the detection efficiency, α_{DE}. This comparison is made in Figure 5.2, where the ratio of the penalty from the number of elements, α_N, to the total penalty, $\alpha_{DE} + \alpha_N$, is plotted as a function of the detection efficiency. The detection efficiency at which the penalty from the number of elements dominates ($\alpha_N < \alpha_{DE}$) can be easily seen in Fig. 5.2(b), where the horizontal axis intersects the vertical axis at $\alpha_{DE} = \alpha_N$. For the commonly encountered case of detecting two photons, the detection efficiency of the elements must be high (>86.6% for the case of $N = 4$ and >96.8% for the case of $N = 16$) in order for the penalty from the number of elements to dominate. In fact, even for the case of detecting three or four photons with a 4-element detector, the detection efficiency penalty dominates when the efficiency is below 72.1% or 55.3%

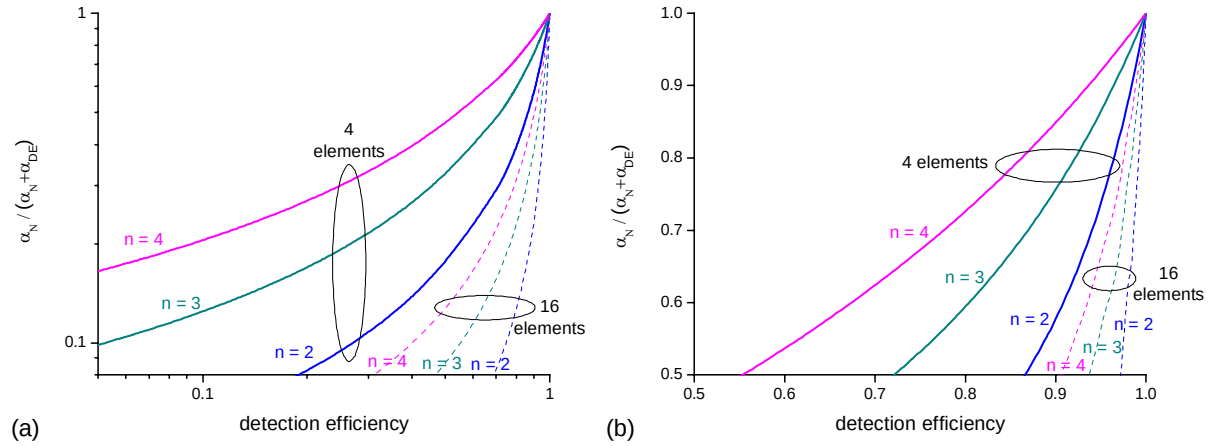

Figure 5.2: Fraction of the penalty due to the finite number of elements plotted on (a) logarithmic and (b) linear scales. The detection efficiency must be greater than the value at which the curves in (b) intersect the horizontal axis ($\alpha_{DE} = \alpha_N$) in order for the penalty from the number of elements to dominate.

respectively. Given that the detection efficiency and coupling losses of the superconducting nanowire single-photon detector elements will be the primary limitation to its performance for measuring four or fewer photons, there is little fidelity to be gained by using more than four elements in applications that do not require counting large numbers of photons. Therefore, a four-element superconducting nanowire single-photon detector will be used to demonstrate the photon-number-resolving capability of this approach.

5.1.2 Photon-number statistics for coherent light measured with an N-element detector

Although we have now examined the fidelity of the spatially-multiplexed approach in resolving photon number states, it is more straight-forward to test the detector with a coherent source than with photon number states. We may again use the probabilities previously calculated in Ref. 87, along with the photon statistics for coherent light to find the probability, $P^N_\eta(m|\lambda)$, of measuring m counts from an optical pulse with, on average, λ photons using an N-element detector with detection efficiency η:

$$P_{\eta}^{N}(m\,|\,\lambda)=\sum_{n=m}^{\infty}\frac{N!}{m!(N-M)\,!}\frac{(\eta\lambda)^{n}e^{-\eta\lambda}}{n!}\sum_{j=0}^{m}(-1)^{j}\frac{m!}{j!(m-j)\,!}\left(1-\eta+\frac{(m-j)\eta}{N}\right)^{n} \qquad (5.2)$$

This equation will provide a way to compare measurements made with a coherent source to what is theoretically expected.

5.2 Four-element detector design and fabrication

After the relative importance of the number of elements and the detection efficiency had been determined, we needed to design and fabricate a suitable multi-element detector for further investigating the photon-number-resolving capabilities of this approach. We wanted this detector to have high *system* detection efficiency, including losses coupling light onto the active area, so the detector needed to be packaged in a way that permitted this. Although this new packaging allowed some flexibility in selecting the number of detector elements, it was also important to consider how the data would be collected. Although it was certainly possible to design custom electronics or to synchronize data collection from multiple pieces of hardware, four input channels was standard on many hardware options including the oscilloscope used in chapter 4 and time-correlated single-photon counting hardware that will be described in chapter 6. Consequently, both the fidelity limitation results in section 5.1.1 and the electronic hardware limitations suggested that a four-element SNSPD with the highest possible detection efficiency was the optimal compromise between complexity and performance.

5.2.1 Design of a four-element SNSPD for photon number resolution

As discussed in section 5.1.1, the design of the spatially-multiplexed superconducting nanowire single photon detector needed to take into account several desirable properties, including: (1) a sufficient number of elements, (2) equal splitting of the light between the elements and (3) elements with as high detection efficiency as possible. First, we determined that four elements sufficed for measurements of up to four photons, but did not introduce too much complexity in the readout. Second, the crosstalk between two neighboring elements was found

to be very low in chapter 4, encouraging the possibility of interleaving several elements in a configuration similar to that described in chapter 2. Such an interleaved design ensured that the light was split equally between the elements and that the splitting ratio was insensitive to the optical alignment of the detector. Finally, maximizing the detection efficiency of the elements required several tradeoffs. This optimization needed to consider all three contributions to the detection efficiency: the coupling efficiency, the absorption and the internal detection efficiency. Tradeoffs existed between the device area, wire width, fill factor (wire width divided by wire pitch) and film thickness.

These tradeoffs between detector parameters and the detection efficiency were not fully understood and only some of the contributions to detection efficiency could be accurately calculated. For example, coupling efficiency could be accurately and easily calculated as a function of the detector active area by knowing the achievable optical spot size, but the relationship between internal detection efficiency and wire width or film thickness was not even consistent between devices on the same chip, much less different chips or different superconducting films. While developing a model to accurately describe how the nanowire parameters affect the internal quantum efficiency would have been difficult enough if the devices had consistent performance, it was clear from the wide variations in device performance that some uncontrolled parameter, or the constrictions discussed in chapter 1, played an important role. Without understanding these variations well, there was little hope of generating a model to accurately predict the tradeoffs.

Fortunately, we could investigate the tradeoffs experimentally. Hundreds of detectors could be fabricated on a single chip, and the parameters of each detector could be set by changing a layout file in which the nanowire patterns were defined. Similarly, a large number of detectors could be tested with the cryogenic probing station setup described in chapter 4 and the detector with the best overall performance could be selected. However, it was not practical or desirable to test the parameter space completely, particularly given that some knowledge about the tradeoffs was known. The four nanowire parameters that needed to be considered were (1) detector active area, (2) fill factor, (3) superconducting film thickness, and (4) wire width. The remainder of this section will discuss how each of these parameters was expected to

influence the system detection efficiency, and the extent to which the parameters were varied to explore tradeoffs.

Detector active area

Large detector active area simplifies optical coupling and ensures that high coupling efficiency can be achieved, but also reduces the yield with which good devices are obtained. In order to demonstrate high system detection efficiency, an active area large enough to achieve high coupling efficiency was required. The packaging will be discussed in more detail in section 5.3, but the minimum achievable spot size using readily available optics and without appreciable clipping of the optical beam by the focusing optics was ~4 μm $1/e^2$ diameter. The package allowed high-resolution in-situ alignment of this optical beam to the detector active area, but a slightly oversized detector active area was desirable to provide margin for a potentially enlarged spot size as the fiber focuser was cooled (its alignment is optimized at room-temperature) and for potential vibrations of this focused spot on the detector. Furthermore, although the detector yield decreased with increasing area, the initial objective was to demonstrate a single detector with high efficiency, so a sufficiently large active area was considered more important than high yield. Consequently, an active area of ~10 μm diameter was selected. In general, the detectors were fabricated with a circular-shaped active area (with straight, parallel nanowires covering this area) in order to minimize the non-illuminated area of the device, which would only reduce the potential detection efficiency by increasing the probability of a constriction (defect). However, a control device with a square active area was also fabricated and tested.

Fill Factor

Increasing the fill factor of the detector should deterministically increase the absorption in the device, while potentially decreasing the internal efficiency of the device (most likely due to increasing the probability of incorporating a defect). The fill factor was limited by the challenge of fabricating narrow gaps, particularly given that the process (HSQ development with 25% TMAH) was not altered. Consequently, the fill factor for most devices was maximized within reasonable limitations of the process by setting the gaps between the wires in the layout file to 60 nm (~70 nm after development at the selected doses). Once again, the control device

(with square-shaped active area) was designed with the standard 100 nm wide gaps (~110 nm after development).

Film Thickness

The film thickness was not intentionally varied, but sufficient variations existed between the fabricated chips to investigate the range of interest. Although significantly thicker films than those used should permit near-unity absorption in the detectors with a cavity, the internal detection efficiency of such devices were always found to be very low, so the target film thickness for all devices was set at the value used for producing high efficiency devices (4 nm quoted thickness for films deposited by Moscow State Pedagogical University). The actual thickness (and/or superconducting properties) varied sufficiently across wafers and between wafers to permit the necessary thickness range to be investigated using nominally identical films.

Wire Width

Finally, wire width was varied between detectors in order to explore potentially available tradeoffs. Wires with widths of 60 nm, 80 nm and 100 nm were defined in the layout file, resulting in wire widths of ~ 50 nm, ~ 70 nm and ~ 90 nm after development at the selected doses. The control detector had 100 nm (~ 90 nm after development) wide wires.

Scanning-electron microscope images of two of the investigated device types are shown in Fig. 5.3. The detector designs were arranged in the layout file, along with several single-element detector designs, to be fabricated on adjacent contact pads, such that all of the detector designs were distributed across the chip. This distribution limited the probability that variations in the superconducting film thickness or properties across the area of the chip dominated the differences between detector designs.

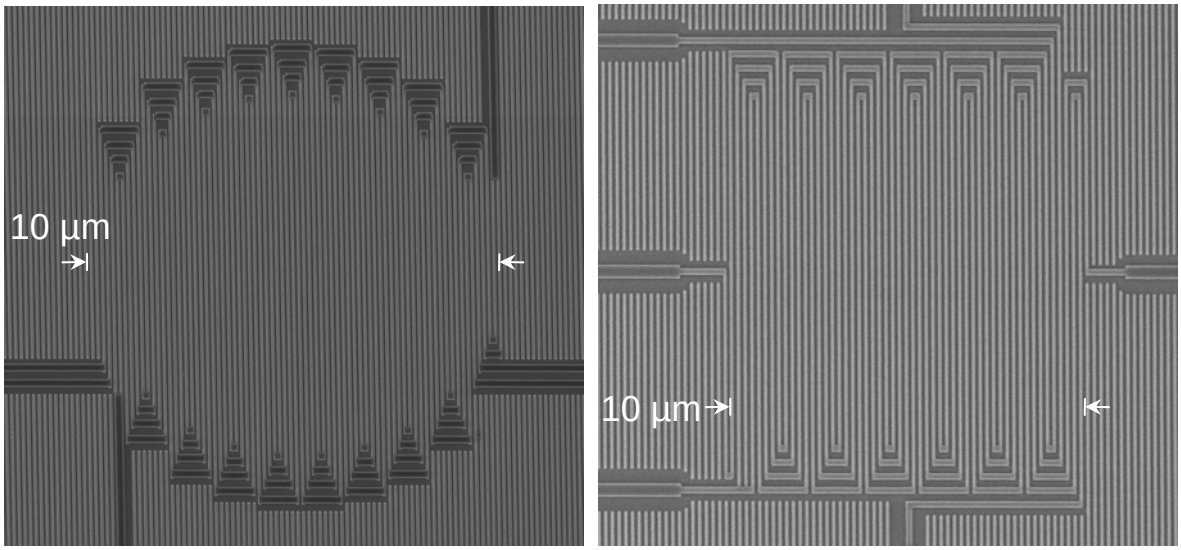

(a) (b)

Figure 5.3: Scanning-electron micrographs of developed HSQ resist on NbN prior to etching for the four-element detector designs. The detector with a circular-shaped active area (a) was designed to have nanowires covering a region with average diameter of 9.4 µm and the control detector with a square-shaped active area (b) had nanowires covering a ~10 µm×10 µm area. The nanowire widths (and pitch) after development were (a) ~50 nm (120 nm) and (b) ~90 nm (200 nm).

5.2.2 Four-element SNSPD fabrication

The detector structures were fabricated using nearly the same process as described in section 4.1.2. A few process details were changed and are noted here, although the performance of single element devices, used as control detectors, were not notably different after the changes and large variations in device performance, due to constrictions and perhaps other effects, continued to be seen. First, the electron beam resist used to fabricate the four-element detectors was switched to Dow Corning XR-1541 (6% solids), spun to a thickness of 80 nm – 90 nm at a spin speed of 6.5 krpm. The XR-1541 resist is also an HSQ resist in MIBK, but is marketed specifically for use as an electron-beam resist with the stated difference being its higher-purity relative to the previously used FOx-12 formulation. Additionally, the spin thickness of the 6% solids formulation of XR-1541 eliminated the need to dilute the HSQ with MIBK, which may have reduced the probability of the resist degrading before its stated shelf life (> 10% changes in the sensitivity of the resist, increasing line-edge roughness of developed features and changes in

the viscosity of the resist prior to spinning – either noticeable formation of solids in the resist bottle or > 10% changes in the spin thickness of the resist – were considered indicative of resist degradation). Changes in the electron-beam patterning of the resist included the upgrade of the Raith 150 tool, which coincided with patterning offsets for certain layouts, and the use of the 30 μm aperture (as opposed to the previously used 20 μm aperture) in order to increase the writing speed. The patterning offsets present in features written with the upgraded Raith 150 tool were limited to regions outside the active area of the device, and consisted of offsets of as much as ~ 50 nm between features written by scanning the beam in orthogonal directions. The pattern offsets were dependent on the writing speed and details of the pattern, but could not be removed even with scan speeds < 1 mm/s, far below the specified maximum, or by resetting all of the beam scanning parameters to their default values (which made the offsets worse). Increasing the aperture size resulted in a beam current of ~ 230 pA and reduced the pattern writing time by approximately a factor of 2, without any noticeable variation in the patterning quality. Consequently, the modifications to the fabrication process were not expected to alter the performance of the detectors.

In addition to these small changes to the nanowire fabrication process, optical cavity structures consisting of a dielectric spacer and reflector were fabricated on top of the detectors to increase the optical absorptance. The fabrication process for this cavity structure closely follows the process described in Ref. 7 and section 3.1.4. Initial optical calculations, based on an effective index model of the patterned NbN, suggested that a cavity thickness of 210 nm would be optimal, so the dielectric spacers on all devices discussed in this chapter were fabricated to be ~ 210 nm thick. The layer of HSQ (Dow Corning FOx-15, diluted 1:1 with MIBK) used to form the cavity spacer was spun to a thickness of ~ 250 nm over the patterned HSQ remaining on the underlying nanowires. After spinning of the HSQ, the sample was baked at 90ºC for 3 min and aquaSAVE (Mitsubishi Rayon America Inc.), a conductive spin-on polymer, was spun onto the devices at 3 krpm in order to provide a continuous, conductive film through which charging of the sample could be prevented during electron-beam patterning. Large, 40 μm × 40 μm square areas were exposed in the Raith 150 electron-beam lithography tool, centered on the detector area. This exposure was performed with a 60 μm aperture (to increase beam current; patterning resolution

was not critical) at 10 kV acceleration voltage with an exposure dose of 600 $\mu C/cm^2$. The exposed HSQ was then developed in 25% TMAH for 4 min, rinsed in deionized water and dried with nitrogen. Following development of the dielectric spacers, the height of the features was measured and reduced by the necessary ~30 nm using reactive-ion etching. The etch rate of the electron-beam-cured HSQ in the CF_4-based reactive-ion-etching process was 20 nm/min (±1 nm/min) after the 600 $\mu C/cm^2$ exposure with 10 kV electrons.

After fabricating the dielectric spacers, the final step was to fabricate the reflectors using a photoresist-based liftoff process similar to the one used to pattern the contact pads. Identical to the contact pad process, a ~1.2 μm-thick layer of Shipley 1813 was spun on the chip at 5.5 krpm and baked at 90ºC for three minutes. The photomask was aligned to the underlying contact pad layer using a Karl Suss MJB3 contact aligner (High-resolution model in the Experimental Materials Laboratory at MIT) and exposed for 1 minute. The chip was soaked in chlorobenzene for 15 min, developed in Microposit 352 (sodium hydroxide-based developer) for 3 min, rinsed in deionized water and dried with nitrogen. The chip was inspected with an optical microscope to confirm that a sufficiently high dose was used in order to achieve full development (no residual photoresist was visible in regions that should have been developed). A 1 nm-Ti-and-120 nm-Au layer was evaporated on the chip. Liftoff was performed in N-Methyl-2-pyrrolidone (NMP) heated to 90ºC and subsequently rinsed in room-temperature acetone and deionized water. The continuous Ti / Au sheet lifted off in order to define the cavity reflectors often took 1-2 minutes to peel off completely and was often aided by gentle agitation of the chip in the NMP. In cases when an edge or corner of this Ti / Au film remained adhered to the chip, the chip was moved to the acetone soak with the film folded away from the surface of the chip and could be fully removed with a gentle acetone spray. Following the deionized water rinse, the chip was dried with nitrogen and inspected in the optical microscope to ensure adhesion of the reflectors (Fig. 5.4). Reflectors with good adhesion and smoothness were achieved with high yield (>95%) despite the thin titanium adhesion layer.

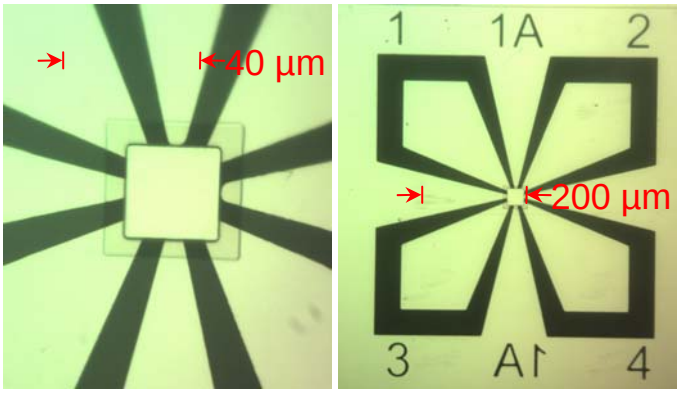

(a) (b)

Figure 5.4: Optical micrographs of the completed cavity structure and surrounding contact pads recorded with a (a) 100× objective and (b) 20× objective.

5.3 Four-element SNSPD packaging and measurement setup

Initial testing of the detectors was performed in a cryogenic probing station, as described in section 4.2. This testing was conducted primarily to select a 4-element detector in which the elements had high and roughly equal detection efficiencies. It was also used to calibrate the device detection efficiency, subtracting for coupling losses, since it was straightforward to measure the size of the optical beam in this setup.

A second setup, based on a closed-cycle cryocooler, was used to focus the light from a single-mode optical fiber onto the detector and to operate all four detector elements simultaneously. This package allowed not only a high device detection efficiency to be demonstrated, but virtually eliminated the coupling loss to achieve high system detection efficiency. Furthermore, the package permitted the continuous operation of all four detector elements over long periods of time, with lower noise count rates than were possible in the probing station. The package will be described in more detail in section 5.3.1. Finally, the optical and electrical setups used to operate and test the four detector elements were very similar to those described in section 4.2, but the differences will be described in section 5.3.2.

5.3.1 Four-element detector package

As discussed previously, one of the important requirements for a detector to resolve the number of photons with reasonable fidelity is high system detection efficiency. Achieving high system detection efficiency requires not only an efficient detector, but also optical coupling to the device that efficiently focuses the light onto the device active area. In order to achieve a high device detection efficiency, an optical cavity structure was added to the detectors that required light be coupled through the substrate. In order to achieve an optical spot size smaller than the ~10 μm-diameter detector active area, it was clear that the light must be focused with a working distance of at least a few hundred micrometers. Furthermore, a mechanism was required for aligning this small focused spot to the detector active area while maintaining (or achieving) this alignment after the package was cooled to cryogenic temperatures. These requirements were met by a package that used cryogenic-compatible nanopositioners to align a fiber + lens assembly with a small focused optical spot onto the detectors in-situ [Ref 37].

The full package was composed of several parts assembled on the cold head of a closed-cycle cryocooler (Fig. 5.5(a)). The cryocooler (Sumitomo RDK-101D) provided 0.1 W of cooling power at 4.2 K and a base temperature of 2.5 K – 3 K, the lower end of which allowed the SNSPD performance to be approximately the same level as the best performance achieved at temperatures < 2 K in the probing station. Electrical connections to the SNSPDs were provided through four well-thermalized (at both the ~ 60 K first stage and the < 4.2 K second stage), high-speed and low-loss semi-rigid coaxial cables (with a stainless steel outer conductor), as well as DC connections through cryogenic wire. The gold-plated copper mount in which the coaxial cables were thermalized to < 4.2 K, and to which the subsequent pieces of the package were mounted, was attached to the coldhead with an intentionally high thermal resistance in order to make the thermal time constant slow. This slow time constant limited the ~ 1 Hz temperature fluctuations on the coldhead from varying the temperature of the detector package by more than ~ 10 mK.

Mounted onto this block was a detector package composed of a gold-plated copper piece with SMP-type electrical connections to the coaxial and DC lines. Electrical connection between

these connectors and the detector chip was made through coplanar waveguides printed on alumina, which are soldered to the connectors and wirebonded to the detectors. The bias current to the device was provided not through the coaxial cable, as was true in the probing station, but instead through a DC line connected to a 100 kΩ chip resistor on the same alumina piece, which was then wirebonded to the signal line of the coplanar waveguide. The 100 kΩ resistor and parasitic inductance of the DC lines, in combination with a DC-blocking capacitor connected to the coaxial cable outside the cryocooler, acted as a resistive bias-"T." The detector itself was selected based on screening for the highest detection efficiency in the probing station, and was diced to a ~4 mm ×4 mm square size to permit mounting in the small area accessible in the detector package using the process described in section 3.1.1. During dicing, the devices were protected with a ~1.5 μm-thick layer of Microposit S1813 photoresist and the chip was placed photoresist-and-device-side down on dicing tape. After dicing, the pieces were removed from the tape in acetone and cleaned with acetone, methanol, and isopropyl alcohol, rinsed with deionized water and dried with nitrogen. The diced chip was mounted on the detector package with silver paint, along with the alumina pieces with coplanar waveguides for resistor attachment and wirebonding.

Finally, an additional gold-plated copper block with the nanopositioners and the attached fiber + lens assembly was mounted on top of the detector package block. The fiber and lens assembly was manufactured by OZ Optics, identical to the one described in section 4.2.2, except that an appropriate optic and focal distance were used to achieve a ~4 μm $1/e^2$ diameter spot (optimized and measured at room temperature). Two different nanopositioner stacks were used, as described below.

This packaging arrangement allowed the required functions of the package to be assembled separately in order to make switching detectors or nanopositioners simple. The package also provided adequate shielding of the detector from both RF and blackbody radiation, except to the extent unwanted photons were transmitted through the optical fiber. In combination with a solid, well sealed radiation shield attached to the first stage of the cryocooler, this package allowed the detector to consistently be cooled to temperatures below 2.8 K. The only significant alteration made to this package was to the nanopositioner assembly. During

testing of the detector used to collect the data for sections 5.4 and 5.5, the coupling efficiency was 63%, despite expectations for a nearly 100% coupling efficiency. Furthermore, the variation of the count rate as the location of the nanopositioners was stepped through the focus suggested that they were not moving freely, because the count rate did not vary smoothly with the intended positioner location, but instead would alternatively become fixed, change drastically and exhibit non-repeatable hysteresis.

A second detector chip was mounted in a block modified to allow more clearance for the fiber and lens assembly, but during testing it was discovered that the count rate fluctuated considerably when the optical spot was focused on the detector active area, presumably due to vibrations. Vibrations between the detector chip and the fiber and lens assembly were likely the result of a known, ~20 μm vibration of the cold head in combination with the non-rigid nanopositioner assembly. The nanopositioners used in this original design were attocube ANP xyz50 model positioners, which were small in size and relied on a single piezoelectric to support a rod on which the top plate of each positioner moved (Fig. 5.5(b)). Based on the discovery of these vibrations, a modified design was introduced for subsequent work which used attocube ANPxyz101 model positioners (Fig. 5.5(c)). These positioners were far more rigid due to their larger size and the fact that the rod on which the top stage traveled was supported on both ends by a membrane. Finally, the fiber and lens assembly were mounted more rigidly to the final positioner by inverting the stack of positioners, as can be seen by comparing Fig. 5.5(b) to Fig. 5.5 (c).

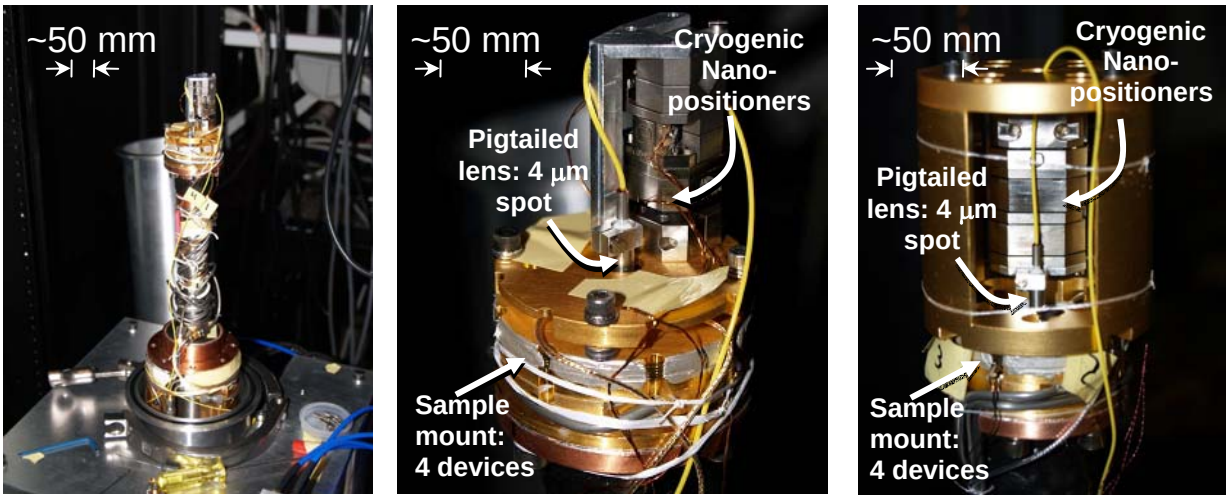

(a) (b) (c)

Figure 5.5: (a, b) Original (using attocube ANPxyz50 nanopositioners) and (c) modified (using attocube ANPxyz101 nanopositioners) package for four-element SNSPDs.

5.3.2 Four-element detector measurement setup

The measurement setup for the four-element detectors was nearly identical to the setup for measuring the two-element SNSPDs described in section 4.2. Once again, the detectors were illuminated with the attenuated 1550 nm-wavelength, mode-locked fiber laser and the data was collected using a 6 GHz oscilloscope, with each of the detector outputs connected to a single input channel (Fig. 4.4).

In addition to using single optical pulses at 10 MHz repetition rate from the fiber laser, pairs of optical pulses spaced by 100 ps in time were generated by splitting output light from the laser into two fibers using a variable-ratio fiber splitter, followed by a 50:50 splitter to recombine the light. Consequently, each of the output fibers from this second splitter had two optical pulses, separated in time from one another because of the difference in the length of the two fibers between the fiber splitters. This delay in path length was set to 100 ps, the variable ratio splitter was used to approximately match the power in each of the optical pulses and all of these components, including the fiber laser, used polarization-maintaining fiber in order to ensure that both optical pulses had the same polarization.

The oscilloscope was set up to record a sequence of 10,000, 5 ns-long traces for each of the four channels while being triggered by the output from a > 40 GHz photodiode. In this way, the simultaneous output from all four detector elements could be recorded and only the electrical output of the detectors within a 5 ns period centered on the timing of the optical pulses had to be stored and analyzed. At each attenuation setting, between 5 and 10 sequences were recorded, for a total of between 50,000 and 100,000 optical-pulse periods. These files were then post-processed in Matlab to extract the times at which each detector-element output crossed a fixed threshold [85].

The simplest measurement to perform using this setup was the system detection efficiency. This required using a relatively high attenuation, 70 - 80 dB, to attenuate the laser pulses to a level at which each detector element would have only a few percent probability of recording a count per optical pulse period. This measurement was repeated in both the probing station and after packaging. In both cases, the system detection efficiency was calculated by dividing the sum of the count rate from all four detector elements (after subtracting background noise counts) by the incident photon flux, which equaled the incident power divided by the energy per photon (1.28×10^{-19} J at 1550 nm wavelength). In the case of the probing station measurement, the device detection efficiency was determined by dividing the sum of the counting rate from all four elements by the incident flux of photons within the 9.4 μm-diameter active-area of the device. The device detection efficiency measured in the probing station for the detector used to take the data described in sections 5.4 and 5.5 was 40% at 95% of I_c at 2.7 K. The system detection efficiency, determined by dividing the sum of the counting rate from all four elements by the number of photons at the fiber input to the setup, was measured under the same conditions in the closed-cycle cryocooler setup to be 25%. Thus, the coupling efficiency, including losses in the fiber, lens assembly and light not focused inside the detector active area, was 63%. Subsequently, using the modified nanopositioning setup described in section 5.4.1 and a detector fabricated on a NbN film deposited at MIT Lincoln Laboratory, a 46% system detection efficiency was measured in the closed-cycle cooler setup (97.5% of I_c at 2.7 K). The fact this same detector was measured to have a 46% device detection efficiency in the probing station indicated that the coupling efficiency is ~ 100% to well within the expected, ~ 10%

fractional uncertainties in measured detection efficiencies (based on uncertainties in the measured beam size in the probing station and the accuracy of the incident power calibration).

5.4 Photon-number-resolution with a four-element SNSPD

We may now compare the photon-number-resolving ability of the 4-element SNSPD to the theory discussed in section 3.2. The output from each of the four detector elements was recorded as the attenuation of the mode-locked fiber laser was varied to produce optical pulses with between ~0.01 and 20 photons per pulse. At each attenuation setting, between 5 and 10 sequences of 10,000 five-nanosecond time periods were recorded on the oscilloscope, and the resulting data files of oscilloscope traces were post-processed in Matlab to extract the times at which each detector-element output crossed a fixed threshold [85]. Using these times, the number of detector elements that fired within ±50 ps of an optical pulse (set independently for each channel to account for differences in the propagation time between the detector element and the oscilloscope) was calculated for each optical pulse period.

The probability of measuring zero, one, two, three or four counts was calculated from the data for each attenuation. These probabilities are plotted as the markers in Figure 5.6(a), with the horizontal axis scaled by the measured, low-flux detection efficiency (i.e. the incident flux was actually 1/(DE = 0.25) = 4 times higher). Additionally, the theory discussed in section 5.1.2 was used to predict the photon statistics, using $N = 4$ elements and assuming the light divided equally between the elements, with each element having the average measured detection efficiency. The small variations between the measured individual-element detection efficiencies and the interleaved geometry justify this assumption. These theory curves are plotted as lines in Figure 5.6(a), and the excellent agreement with the measured count statistics confirm that the detector provided the expected photon-number-resolution. Note that the fit matches the data well both in the regime where the average number of detected photons was less than and greater than 1, which indicates that the detection efficiency of the elements was linear even with a high probability of detecting more than one photon simultaneously.

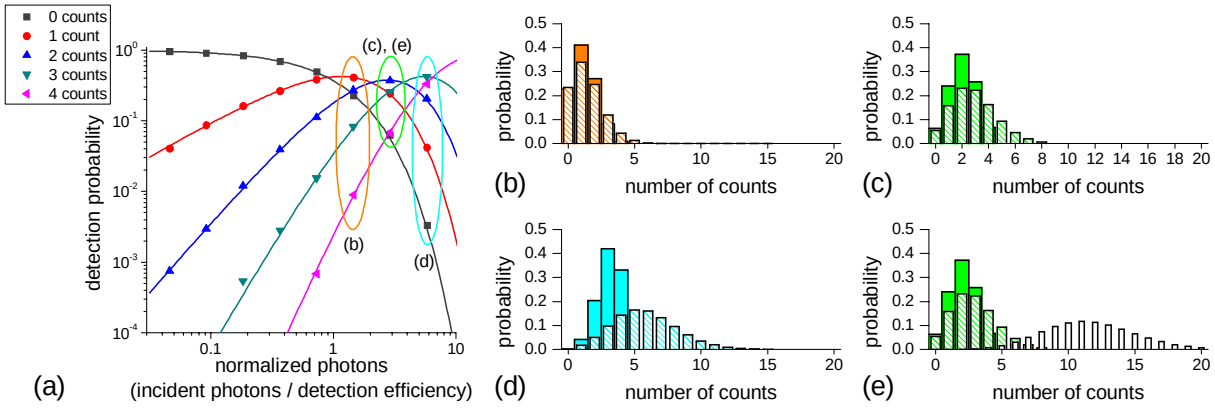

Figure 5.6: (a) Measured (data points) and calculated (lines) detection probabilities for each possible number of counts within a 100 ps timing window as a function of the normalized photon flux. The measured data points are plotted as a function of photon flux normalized by the measured detection efficiency and the calculations are for a four-element detector with unity detection efficiency. The measured detection probabilities (solid filled bars) are also plotted as a function of the number of counts in (b), (c), (d) and (e) for three values of photon flux. Additionally, calculations are shown (hashed bars) assuming $\alpha_N=1$ (no penalty from a finite number of elements) and $\alpha_{DE}=\eta^n$, where η is the measured detection efficiency. The penalty from using 4 elements can be compared to the penalty from the non-unity detection efficiency in (e), where the calculations assuming $\alpha_N=\alpha_{DE}=1$ are also shown (white bars). It is clear that for counting 4 or fewer photons, the fidelity of the photon-number measurement is primarily limited by the detection efficiency and not by the number of elements.

Finally, it is useful to compare the measured count statistics to those that would be expected both for a photon-number-resolving detector without a limited number of elements and for an ideal detector (i.e. also having unity detection efficiency). The comparison to a detector without a limited number of elements is made for the three highest measured photon fluxes in Fig. 5.6(b)-(e) and the comparison to an ideal detector is made in Fig. 5.6(e). It is clear that the effect from having only four elements is smaller than the effect of the non-unity detection efficiency, as we expected for a detector with only 25% system detection efficiency.

5.5 Photon-number-resolution with precise timing resolution

Although the photon-number-resolution of the 4-element SNSPD has now been demonstrated, its primary advantage over other photon-number-resolving detectors is its ability to precisely time

each photon detection event, even for non-pulsed optical signals. This ability makes the multi-element SNSPD useful for measuring the photon-statistics as a function of time for high-speed sources or for mitigating dead-time effects in a variety of applications [16-18, 21].

To investigate these abilities using our four-element detector, the experiment performed in the previous section was repeated, but with two optical pulses spaced by 100 ps in time. The readout and data analysis was carried out in the same way, which provided a time-stamp for every detection event that occurred within the 5 ns-long traces. However, instead counting the number of events within a single 100 ps period, as was done in section 5.4, the number of events in many variable-length time periods were counted, in order to determine the count statistics as a function of time. Figure 5.7(a) shows the probability of measuring different numbers of counts versus time for 100 ps time bins while Fig. 5.7(b) shows the same for 12.5 ps time bins. Virtually all of the detection events resulting from a single optical pulse can be collected in a 100 ps time bin. Additionally, when the time bins are shorter than the ~30 ps-FWHM timing jitter of the detector, the photon statistics can be measured on the time scale of this jitter. However, using short time bins result in the detection events being spread across several bins so that the number of detection event in any given bin is lower (i.e. it acts like an additional loss), so the improved timing resolution comes at the expense of requiring more data be collected. Recording the time stamp of each detection event allows the data to be post-processed in the most appropriate way to obtain the optimal trade-off between precise timing resolution, low uncertainty of the photon-number statistics and short data collection times.

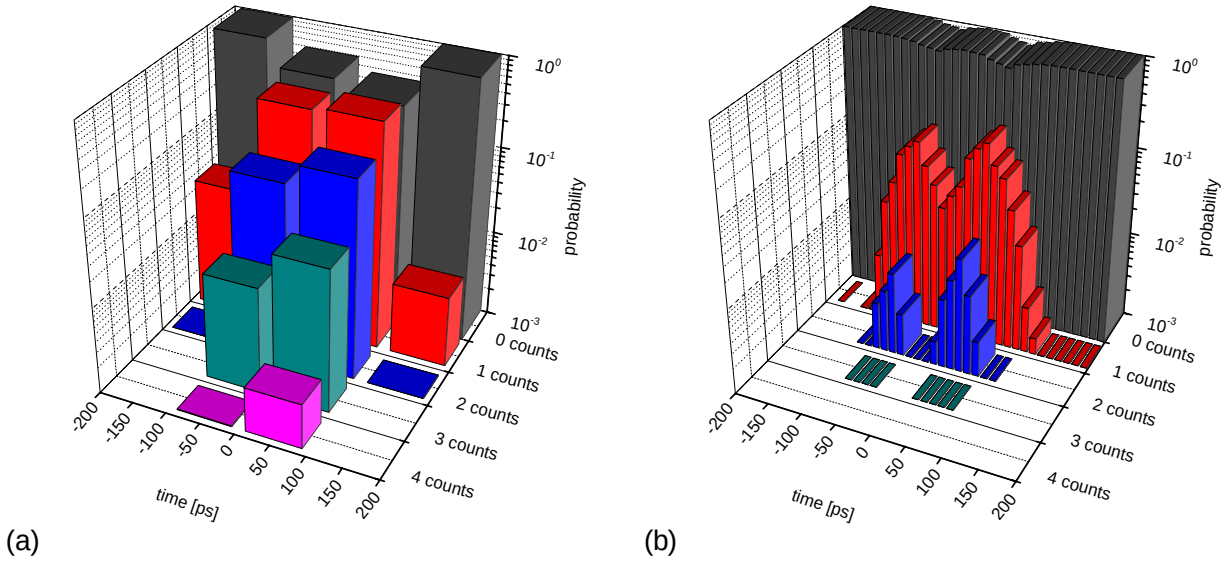

Figure 5.7: Measured photon number statistics (detection probability for measuring each number of counts within the timing window) as a function of time delay for two optical pulses separated by 100 ps in time. The same data is plotted after software analysis is used to determine the statistics for (a) 100 ps time windows and (b) 12.5 ps time windows. The two optical pulses can be clearly resolved in (b) and the photon number statistics for each pulse can be more quickly measured (out to four simultaneous counts) using the wider time windows shown in (a).

5.6 Summary of photon-number-resolution with a four-element SNSPD

Achieving a high-fidelity-photon-number measurement with spatially multiplexed detectors, such as the multi-element SNSPD pursued in this work, relied on obtaining both high detection efficiency and a sufficient number of detector elements. Achievable detection efficiency, as opposed to the number of elements, was found to be the dominant limitation to measurements of four or fewer photons when using four SNSPD elements. The chapter therefore focused on optimizing the *system* detection efficiency of four-element SNSPDs and demonstrating their photon-number-resolving capabilities. A four-element SNSPD with 25% system detection efficiency was used to resolve photon number and independently time photons, showing close agreement with the performance predicted by assuming each element operated independently.

This expected performance was achieved even in cases when the probability of measuring multiple photons was high, without any observed non-linearity in the detection efficiency at high detection probabilities. The precise timing resolution of the 4-element SNSPD permitted counting multiple photons while distinguishing which of two optical pulses 100 ps apart in time was the source of each detected photon, something that no other PNR detector is capable of measuring, including previously-demonstrated temporal [87-88] and spatial multiplexed [89] detectors. Finally, an improved setup for efficiently coupling to the SNSPD and a detector fabricated on a NbN film deposited at MIT Lincoln Laboratory resulted in a 4-element SNSPD with a system detection efficiency of 46%.

Two important questions can and should be answered as an extension of this work. The first is whether small arrays, ideally the four-element SNSPDs demonstrated in this chapter, can be useful for any applications, particularly those taking advantage of their photon-number-resolving capabilities. The second question, which was also raised in the summary to chapter 4, is to what extent the detector elements interact. Fortunately, both of these questions will be answered in chapter 6 using a single experimental setup.

Chapter 6

Crosstalk and Intensity Correlation Measurements with Multi-element SNSPDs

The high sensitivity required to make a detector respond to the absorption of a single photon makes it difficult to eliminate interactions between multiple single-photon detectors. As discussed in section 2.1, virtually all single photon detector arrays exhibit some form of crosstalk between elements. In the case of semiconductor-based detectors such as Geiger-mode avalanche photodiodes, crosstalk can even occur between independent detector modules that are electrically isolated and widely separated in space due to photons that are emitted during the avalanche process. In section 4.3, crosstalk between closely spaced SNSPD elements was measured to be less than ~0.001%, a surprising result given the sensitivity of the detection efficiency to changes in the bias current and the presumed likelihood of crosstalk occurring. However, those measurements were limited by the detector design (side-by-side elements as opposed to interleaved elements), by the way in which the detectors were illuminated (using visible wavelength photons, which made the detectors less sensitive to changes in bias current and nanowire temperature) and by the relatively short data collection times. In this chapter, a more robust measurement of crosstalk was performed to eliminate all of those drawbacks. Using these measurements, an important detector design flaw was identified and corrected. Ultimately, a crosstalk below ~0.00001% was measured without intentional optical illumination, in a regime where the detector was very sensitive to potential electromagnetic and thermal fluctuations.

One application that can make use of this extremely low crosstalk and only a few detector elements is the measurement of intensity correlations. The unique multi-element design, in which the elements are arranged to form a single optical active area, can also simplify and improve the experimental setup required to measure intensity correlations. Finally, intensity correlation measurements are very similar to crosstalk measurements, particularly in terms of the

readout and data analysis. This chapter will discuss second- and third-order intensity correlations that were measured on optical sources including a laser, a pseudo-thermal source and a single quantum dot embedded in a micropillar cavity. These measurements confirmed the unique capabilities and practicality of multi-element SNSPDs.

6.1 Crosstalk Measurements

Although the crosstalk of two-element detectors was considered in section 4.3, additional measurements was required to confirm low levels of interactions between elements under higher-stress conditions. More thorough measurements revealed a source of crosstalk that can be eliminated with a simple detector design change. After the design change, crosstalk between detector elements was virtually eliminated, and was below the measurable ~0.00001% level on short time scales.

6.1.1 Crosstalk measurement setup and detectors

Although there are many potential sources of crosstalk between SNSPD elements, including some related to the packaging and associated electronics, the goal of this section was to evaluate the intrinsic interactions that exist in multi-element SNSPDs. Consequently, sources of crosstalk that are not related to interactions between the detector elements themselves (such as grounding problems, or exposure to electromagnetic noise from the environment) were minimized through careful design of the packaging and readout electronics. Additionally, an interleaved detector design was used to maximize the length of the nanowire over which interactions were likely to occur.

The package used for operating the detector was built at the National Institute of Standards and Technology in Boulder and is described in Ref. 19. Similar to the setup used in Chapter 5 [38, 39], the detector was operated at a stable, ~3 K temperature in a closed-cycle cryocooler. However, the chip was packaged with an optical fiber aligned just above the detector surface, without the use of lens to refocus the light or nanopositioners to optimize the

fiber location. The fiber was aligned to the detector at room temperature using an optical microscope to observe the fiber and detector through the sapphire substrate. The detector mount was sufficiently stable, and the fiber sufficiently well-centered in the mount, so that alignment of the fiber to the detector was maintained during cool-down and vibrations were negligible. The detector mount also included four coaxial electrical connectors, wirebonded to the four SNSPD elements of the detector. Biasing and readout of each detector element used the same setup described in section 4.2.1: a 50 Ω transmission line connected to a bias "T" that was used to split the AC signal to a chain of amplifiers and to supply the DC current bias from an isolated voltage source and a 100 kΩ resistor. Well-shielded coaxial cables, RF attenuators and DC blocks were used to limit noise, reflections and ground loops. The electrical components were properly grounded and the SMA connectors used throughout the system were carefully tightened in order to minimize crosstalk between the detectors due to the electronics.

The detectors used for the crosstalk measurements were 4-element interleaved detectors. All of the detectors were fabricated on superconducting films deposited at MIT Lincoln Laboratory by Dr. Richard Molnar. Two different detector designs were used, which will be described in section 6.1.2. The detectors were fabricated using the process described in section 5.2.2, without the addition of optical cavities, because of the optical coupling technique used in the detector package described above. A dielectric spacer, without the metal reflector, was fabricated using the process for making an optical cavity described in section 3.1.4 on the surface of the detector used to obtain the low-crosstalk results described in section 6.1.2. This dielectric spacer improved the optical absorption of light coupled from the front (non-substrate) side slightly and served to create an environment for thermal interactions between nanowires that was similar to the environment with a full cavity structure, which is critical to demonstrating that low crosstalk and high detection efficiency can be achieved simultaneously.

Finally, the detection events were recorded using time-correlated-single-photon-counting (TCSPC) hardware. The output of each detector element following the amplifiers was connected to an input channel on a field programmable gate array (FPGA; Xylo FPGA development board with an Altera FPGA EP1C3T100) or a HydraHarp 400 TCSPC instrument (Picoquant GmbH). In the case of the FPGA, discrete pulse generators were needed on each channel in order to

convert the detector output signal into a pulse that would be recognized by the FPGA. In the case of the HydraHarp 400, the threshold level for constant-fraction discriminators in the instrument were set to appropriately count the pulses from each detector element. Both TCSPC instruments recorded the channel number and timing of each detection event, with the FPGA providing ~ 7 ns timing resolution and the HydraHarp 400 providing ~ 1 ps resolution. Both instruments recorded this information continuously (the HydraHarp 400 was limited by a ~ 100 ns deadtime following a detection event on the channel in which the event occurred). In both instruments, the channels operated independently, so that simultaneous detection events in different detector elements could be recorded. Using the recorded time stamps from each detection event, software extracted the cross-correlations for any pair of channels over a user-defined range of time delays [90].

6.1.2 Crosstalk measurement results

Crosstalk between detector elements was measured by looking at the cross-correlations between pairs of detectors without any intentional optical illumination. In these experiments, the cross-correlations were defined, without normalization, as the number of times a count in detector *B* occurred after a count in detector *A* within a time delay between $\tau - \Delta\tau_0/2$ and $\tau + \Delta\tau_0/2$:

$$R_{AB}(\tau, \Delta\tau_0) = \int_{\tau-\Delta\tau_0/2}^{\tau+\Delta\tau_0/2} R_{AB}(\delta)d\delta = \int_{\tau-\Delta\tau_0/2}^{\tau+\Delta\tau_0/2} \int_0^T \frac{dN_A(t)}{dt} \frac{dN_B(t+\delta)}{dt} dt d\delta \qquad (6\text{-}1)$$

where T is the total measurement time, τ is the time delay at which the cross-correlation is being measured, $\Delta\tau_0$ is the width of the time bins, and $N_A(t)$ and $N_B(t)$ are the number of counts that have accumulated since $t = 0$ in detector *A* and detector *B* respectively (and their time derivatives are delta functions at each time a count occurs). If the cross-correlation between any two detectors varies as a function of time delay τ, this indicates a correlation between detection events. As discussed in section 4.3, the potential detector-related sources of correlations occur on very short time scales, ≤ 1 ns, so we are most interested in looking at cross-correlations near $\tau = 0$. However, it is also of interest to look at longer time scales to see how well other sources of

potential correlations (interactions in the electrical readout; 60 Hz, radio or microwave frequency noise; ~1 Hz thermal fluctuations in the cryocooler; etc.) have been eliminated from the system.

The second issue to consider is whether to optically illuminate the detectors while performing these measurements. There are several reasons optical illumination would make it more difficult to study intrinsic detector crosstalk. The first problem is that the optical source could have temporal intensity correlations that would result in unavoidable, but not detector-crosstalk-related, cross-correlation between detectors. These types of cross-correlations will be used to study optical intensity correlations in sections 6.2 and 6.3, but would complicate an investigation of crosstalk because the cross-correlations due to crosstalk and due to optical intensity correlations would need to be distinguished. Second, the level of crosstalk between detectors is likely to depend on the sensitivity of the detectors to electromagnetic or thermal fluctuations. The background noise counts are very sensitive to changes in both bias current and device temperature, while the detection efficiency at wavelengths of 1550 nm or shorter is not as sensitive. Consequently, crosstalk should be more easily observed when all of the counts are from background noise, rather than mostly from near-infrared or visible-wavelength photons.

We must also consider whether the lower noise count rate, compared to the higher count rates possible with optical illumination, will degrade the signal-to-noise ratio (SNR) of the crosstalk measurements. The SNR of the crosstalk measurements will be defined as the expected number of crosstalk events divided by the noise in the cross-correlation measurement. The crosstalk will be described in terms of two random variables, C_A and C_B, representing the number of crosstalk events induced by a count in detector A and B respectively. It is assumed, and will be confirmed experimentally, that the detector counts are well-approximated by Poisson processes, that the contribution from crosstalk is small, and that the primary source of noise in the cross-correlation measurements is statistical noise. We can therefore define the SNR of the crosstalk measurement as:

$$\mathrm{SNR} = \frac{\mathrm{E}[C_A] + \mathrm{E}[C_B]}{\sqrt{\mathrm{Var}[R_{AB}(\tau, \Delta\tau_0)]}} \tag{6-2}$$

The probability of a count in detector *A* (and similarly in detector *B*) resulting in a crosstalk event in detector *B* (*A*) will be described by the variable c_A (c_B). Assuming the crosstalk counts are uncorrelated to one another, the expected number of crosstalk events is:

$$\mathrm{E}[C_A]+\mathrm{E}[C_B]=\sum_{k=0}^{\infty}k\frac{e^{-c_A\lambda_A T}\left(c_A\lambda_A T\right)^k}{k!}+\sum_{k=0}^{\infty}k\frac{e^{-c_B\lambda_B T}\left(c_B\lambda_B T\right)^k}{k!}$$

$$=\left(c_A\lambda_A+c_B\lambda_B\right)T \tag{6-3}$$

where λ_A and λ_B are the non-crosstalk-induced count rates in detectors *A* and *B*, respectively.

The noise is assumed to be due primarily to statistical noise in the number of cross-correlation events. Furthermore, it will be assumed that the dominant source of cross-correlation events at zero time delay are due to two noise counts randomly and independently occurring in two elements. This assumption was initially justified by the results in section 4.3.3, in which the crosstalk events were not measurable compared to the random coincidence events, and it will be justified again by the data in this section. Using these assumptions, and given that the probability of measuring a correlation count in any single time period $\Delta\tau_0$ is small, the variance in the cross-correlation measurements is:

$$\mathrm{Var}\left[R_{AB}(\tau,\Delta\tau_0)\right]\approx\mathrm{E}\left[R_{AB}(\tau,\Delta\tau_0)\right]=\lambda_A\lambda_B T\Delta\tau_0 \tag{6-4}$$

Thus, the measurement SNR is:

$$\mathrm{SNR}=\frac{\mathrm{E}[C_A]+\mathrm{E}[C_B]}{\sqrt{\mathrm{Var}\left[R_{AB}(\tau,\Delta\tau_0)\right]}}\approx\frac{\left(c_A\lambda_A+c_B\lambda_B\right)T}{\sqrt{\lambda_A\lambda_B T\Delta\tau_0}} \tag{6-5}$$

Given that λ_A and λ_B are both proportional to the optical power, the crosstalk measurement SNR is independent of this power. Consequently, crosstalk should be measured using the detector noise counts alone based on all of the advantages of measuring detector crosstalk without optical illumination described above.

Initial cross-correlation measurements were performed on two different 4-element SNSPDs of the same design as the detector used in chapter 5 (shown in Fig. 6.1(a)). Two

similar, but distinct, detector packages were used for comparison, one described in section 6.1.1 and the other described in section 5.3.1, in order to check the reproducibility of the results. The noise count events in both detectors were recorded using the FPGA. In both cases, two pairs of detector elements (the same pairs of detector elements in both setups) exhibited considerable crosstalk. Furthermore, this crosstalk varied as expected when a laser source (which has τ-independent intensity correlations) was used to illuminate the detector elements. Specifically, the cross-correlation at $\tau \approx 0$ (from crosstalk) was much larger at low optical intensities than at high intensities when the cross-correlation counts were normalized by their expected value (Eq. 6.4). A careful review of the detector design revealed the source of this crosstalk: pairs of elements were connected to ground through a single NbN nanowire with a non-negligible (~ 4.1 nH) kinetic inductance. This inductance prevented the detectors from being operated independently – when one element became resistive and current was shunted into the transmission line to which it was connected, some of that current was also forced into the neighboring nanowire because of the high-impedance between the elements and ground. This circuit is shown in Figure 6.2 and has been modeled in Pspice, confirming that the current in the

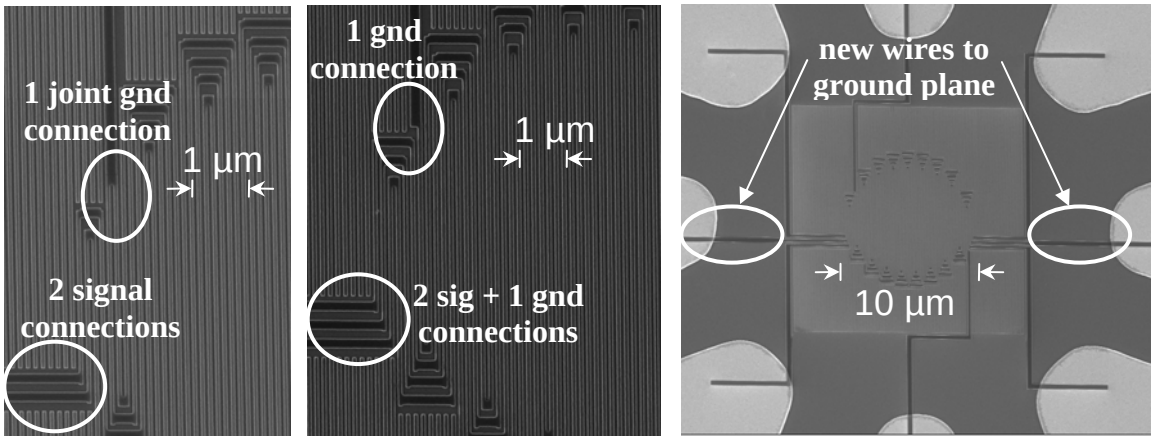

(a) (b) (c)

Figure 6.1: Scanning-electron microscope micrographs of 4-element SNSPDs. (a) 4-element SNSPD with a single NbN nanowire connecting two of the elements to the ground pad (surrounded by upper white ellipse) and the remaining two elements (surrounded by lower white ellipse) connected to ground through a single NbN nanowire on the opposite side of the detector (not shown). (b), (c) Revised 4-element SNSPD with no elements shorted together (surrounded by white ellipses in (b)) before the ground plane (c). This design required two additional NbN nanowires to ground (surrounded by white ellipses in (c)).

paired element was likely to increase to a peak value ~0.8% higher than the DC level. The strong dependence of the nanowire detection efficiency and noise count rate on the bias current made even this small increase in the adjacent-nanowire-bias current a very likely source of the observed crosstalk.

Next, a new detector, shown in Fig. 6.1(b, c), in which each detector element was independently connected to the gold ground plane was designed, fabricated and tested. Cross-correlation measurements were performed on this detector using the HydraHarp 400 to record the timing of the detector counts. The fiber input to the detector was blocked and the bias

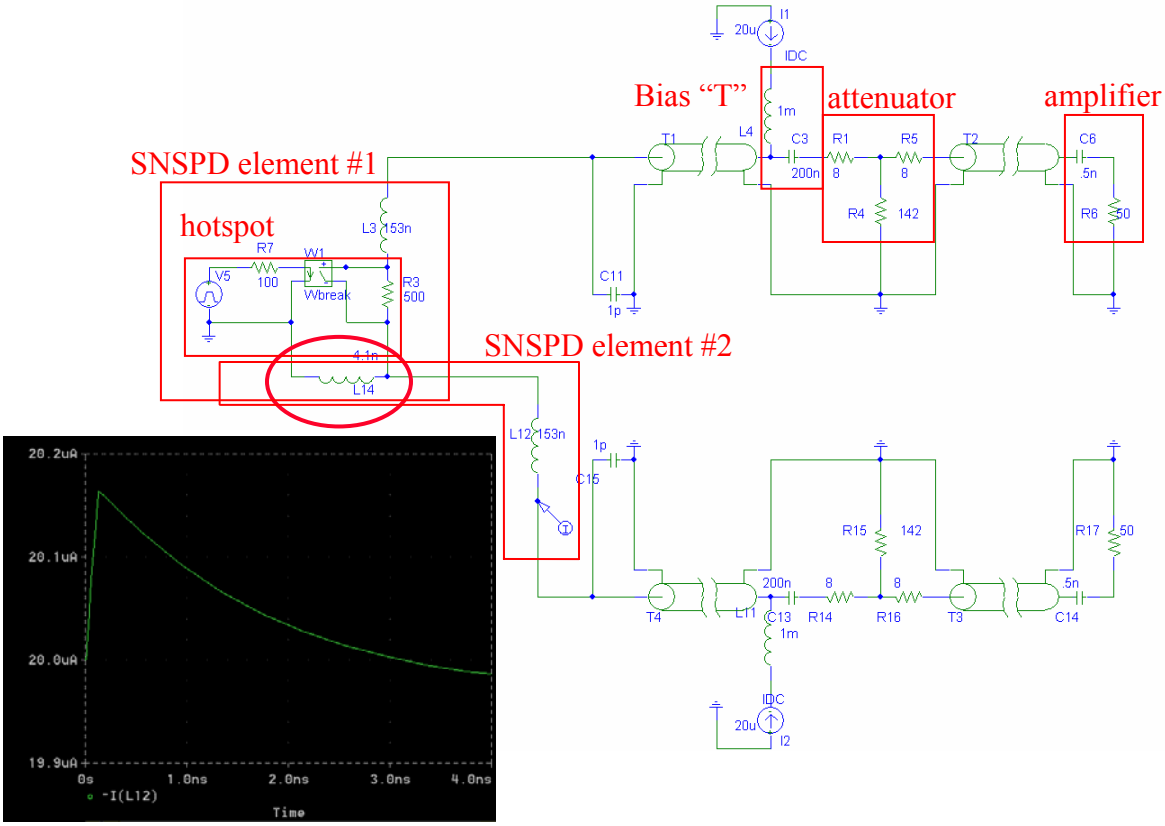

Figure 6.2: Pspice model of two of the four elements from the original four-element SNSPD design in which both elements were grounded through the same NbN nanowire. This NbN segment had ~4.1 nH of inductance (surrounded by red ellipse in circuit diagram). Consequently, when a detection occurred in the adjacent nanowire (top half of the circuit diagram), some current was shunted into the element that did not fire (bottom half of the circuit diagram). The current in the detector that did not fire, assuming a 20 μA bias current for both detector elements, is shown in the inset following a detection event at time=0 in the adjacent nanowire.

current in each detector element was set to 90−95% of its critical current, such that the noise count rate was ~85 Hz in each channel. This operating point was chosen because the detector was typically operated at these currents during experiments, the noise counts were very sensitive to environmental changes and the SNR of the crosstalk measurement was independent of the detector count rate. Data was collected for 16.6 hours, corresponding to ~5 million counts from each detector element. The timing information was then analyzed in order to extract the cross-correlations for each pair of detector elements, which are shown in Fig. 6.3(a) for 10 ns time bins over time delays between -2 μs and 2 μs. Visually, there is no indication of crosstalk in the central 10 ns bin, and this can also be verified mathematically: the crosstalk, using the sum of the cross-correlation counts from all six detector element pairs, was found to be 0.000007% ±0.000017%. This indicates that the level of interaction between nanowire elements was very

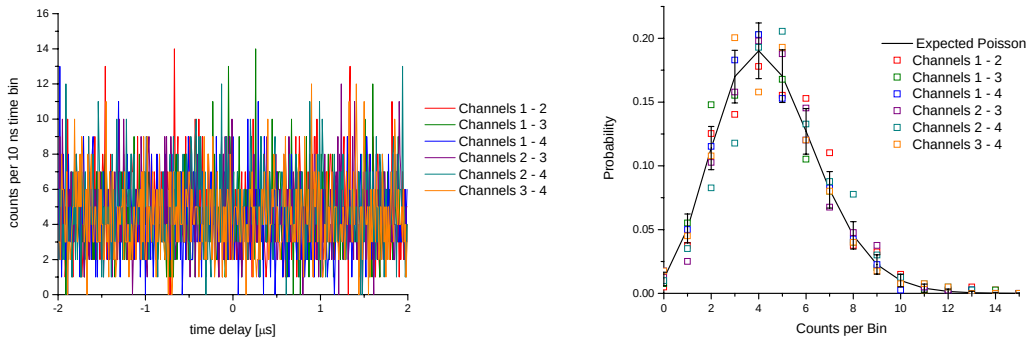

(a) (b)

Figure 6.3: (a) Cross-correlation counts for the revised 4-element SNSPD design. The cross-correlation counts were calculated within -2 μs≤τ≤2 μs for time bins of $\Delta\tau_0$=10 ns. The cross-correlation counts for all 6 pairs of detector elements (4 choose 2) are plotted, with no pairs of elements visibly exhibiting cross-correlations at zero time delay (corresponding to intrinsic crosstalk between the elements). (b) Histogram of the occurrence probability of different numbers of cross-correlation counts within a $\Delta\tau_0$=10 ns time bin, over the time delay span of -2 μs≤τ≤2 μs. The measured number of counts per time bin are plotted as open squares for each of the 6 pairs of detector elements and the expected distribution is plotted as a solid line with error bars. The solid line was calculated assuming the distribution is Poisson, with an expected value determined from Eq. 6.4 (i.e. expected cross-correlations assuming the data was uncorrelated, not fitted to the mean of the measured values). The error bars were calculated based on the expected statistical noise from the 200 time bins from which the data points on the histogram were derived. The close fit between the data and calculation indicate that the detector outputs were indeed uncorrelated and well-described by Poisson statistics.

low, and was not measurable after 16 hours of noise count correlations, which are more sensitive to crosstalk than light count correlations, were recorded.

The extent to which the noise counts in the detector elements were independent over longer time scales was also considered. First, the distribution of the number of cross-correlations counts per time bin was compared to the distribution calculated assuming these correlation events were random. This comparison is made in Fig. 6.3(b), with the data points corresponding to the actual frequency with which a certain number of correlation counts was measured, and the black line corresponding to the expected frequency (with error bars corresponding to the expected statistical variation based on the limited number of time bins). It is clear that the cross-correlation data from all six pairs of elements followed the expected distribution. Consequently, as assumed in the derivation of the measurement SNR, the detector noise counts were well approximated by Poisson processes.

Next, if the noise counts from a pair of detector elements are correlated over times longer than a few nanoseconds, perhaps due to environmental electromagnetic noise or fluctuations of the detector chip temperature, the cross-correlation data should be modulated at this frequency. Fourier transforms of the normalized cross-correlation data are plotted in Fig 6.4 using the detector noise count data analyzed on two different time scales ($\pm 2\,\mu s$ in Fig 6.4(a) and $\pm 0.2\,s$ in Fig 6.4(b,c)). The cross-correlation data was normalized by dividing the correlation counts in each time bin by the expected correlation counts (see Eq. 6.4) and subtracting 1, so that the cross correlations were expected to be centered around zero. There does appear to be a statistically-significant modulation of the cross-correlations at 60 Hz (AC power frequency) between channels 1 and 2, although the magnitude of the modulation was small (negligible for most detector element pairs) and could probably be further reduced by improving the electrical isolation of the detector readout. Finally, the random nature and negligible magnitude of deviations of the measured cross-correlations from the expected values were demonstrated by calculating the average values of these deviations. The average, measured cross-correlation deviated from its expected value by $0.011\% \pm 0.007\%$. This suggests there was a small positive cross-correlation that extended over long time periods, but the effect was almost in the noise. The statistical noise within a single time bin was typically more than an order of magnitude

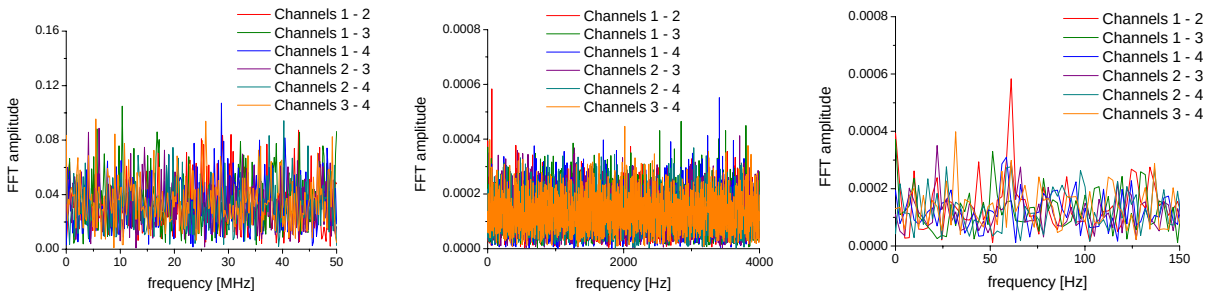

Figure 6.4: Fourier transform of the normalized cross-correlation counts (cross power spectral densities) for each of the 6 pairs of detector elements. The cross power spectral densities are plotted over three different frequency ranges: (a) 0 to 50 MHz, (b) 0 to 4 kHz and (c) 0 to 150 Hz. The variation in the magnitude of the cross power spectral densities in (a) compared to (b, c) are due to the higher statistical noise in the $\Delta\tau_0 = 10$ ns time bins used to calculate the data shown in (a) compared to the $\Delta\tau_0 = 100$ μs time bins used to calculate the data in (b, c). The highest cross power spectral density is observed at 60 Hz frequency, although this is barely above the statistical noise and appears to be most problematic for the cross-correlation counts between channels 1 and 2.

higher than this deviation, and this deviation was the worst-case value determined from cross-correlating noise counts that were highly sensitive to external fluctuations. Consequently, crosstalk between nanowire detector elements separated from one another by just 60 nm over tens of micrometers length was reduced to levels within the expected statistically noise for virtually all potential measurements.

6.2 Second-order Intensity Correlation Measurements

Intensity correlation measurements are one of the key techniques for characterizing photon statistics and identifying effects such as bunching [91] and anti-bunching [92], which can reveal important information about the physics governing emission. Instead of directly measuring the photon statistics, which are affected by loss and detector imperfections, intensity correlations can be measured using a Hanbury Brown-Twiss (HBT) interferometer geometry, which consists of a beamsplitter and two discrete single-photon detectors [91]. The beamsplitter serves to split the light into each of its output modes, so that both detectors sample light from the spatial modes of

interest, and intensity correlations for a stationary source are a function only of time delay (τ) [93]:

$$g^{(2)}(\tau) = \frac{\left\langle :\hat{I}(t)\hat{I}(t+\tau): \right\rangle}{\left\langle \hat{I}(t) \right\rangle^2}, \tag{6-6}$$

where :: denotes normal ordering of the creation and annihilation operators contained in the intensity operator, $\hat{I}$.

Alternatively, a single detector can be used to measure temporal intensity correlations [94], eliminating possible artifacts with the HBT including discrete detectors aligned to different spatial modes or spurious reflections off the beamsplitter. However, using a single detector typically prevents or complicates correlation measurements at small time delays. The finite recovery time of the analog-output signal from a photon-number-resolving (PNR) detector makes it difficult to independently resolve and accurately time all closely spaced detection events. With a single non-PNR detector, correlation measurements are limited to time delays longer than the deadtime of the detector and electronics.

A two-element SNSPD combines the advantages of both the two-detector HBT interferometer and the single detector approaches. These advantages were demonstrated by measuring intensity correlations of a laser and a quantum-dot-single-photon source.

6.2.1 Second-order intensity correlation measurement setup and detectors

The desirable features of discrete SNSPDs for measuring intensity correlation functions have been previously demonstrated [19, 95-98]. The precise timing resolution, fast reset time and low dark count rate provided by SNSPDs has enabled measurements of fast photoluminescence (PL) [97-99] and second-order intensity correlation functions [19, 95-98] over a range of near-IR wavelengths.

A multi-element SNSPD can be used to make intensity correlation measurements without the need for a beamsplitter or the disadvantages of using an analog-output PNR detector.

Temporal intensity correlations can be measured between independent elements of the multi-element SNSPD in the same way as with discrete detectors. The independent elements prevent extra correlations that would be introduced by a PNR detector if the detection efficiency or ability to correctly resolve detection events varied when photons were nearly simultaneous, which can be a problem for PNR detectors with low signal-to-noise ratios or for photons incident during the detector recovery. Furthermore, the output signal from each multi-element SNSPD detector can be analyzed using standard time-correlated single photon counting (TCSPC) hardware, and the photon timing can be precisely resolved independent of the time delay between photons. Finally, using a single active area eliminates the need for a beamsplitter, simplifying the optical setup and eliminating artifacts such as discrete detectors aligned to different spatial modes or spurious reflections off the beamsplitter.

In order to demonstrate the validity and advantages of the multi-element SNSPD, this approach was compared to a conventional HBT interferometer using the experimental setup shown in Fig. 6.5 [100]. The single-photon source consisted of a self-assembled InGaAs quantum dot buried in a vertical micropillar cavity [95] that was cooled to ~5 K in a liquid-helium flow cryostat. The quantum dot was excited using a mode-locked Ti:Sapphire laser producing ~1 ps pulses at 82 MHz repetition frequency and 779 nm center wavelength. This light was attenuated to ~200 nW average power and focused using a long-working-distance objective to a spot size of ~5 μm so that it excited only a single micropillar. The same objective collected the PL emitted at 959.7 nm from the quantum dot, which was filtered using a monochromator and sent into either the free-space HBT with two silicon single-photon avalanche diodes (Perkin-Elmer SPCM-AQR SPADs [46]) (Fig. 6.5(b)) or collected in a single-mode (at 1550 nm wavelength) fiber for delivery to the two-element SNSPD (Fig. 6.5(c)).

The two-element SNSPD was designed as a linear array of four SNSPDs, each with a 5 μm-by-10 μm area such that any two adjacent SNSPDs formed a 10 μm-by-10 μm active area (Fig. 6.5(d)). NbN films were deposited at MIT Lincoln Laboratory and the devices were fabricated, without optical cavities, using the process described in section 5.2.2. Each element was connected to the gold ground plane through a separate NbN nanowire to avoid the crosstalk issues described in section 6.1.2. The chip was packaged in the same way as the 4-element

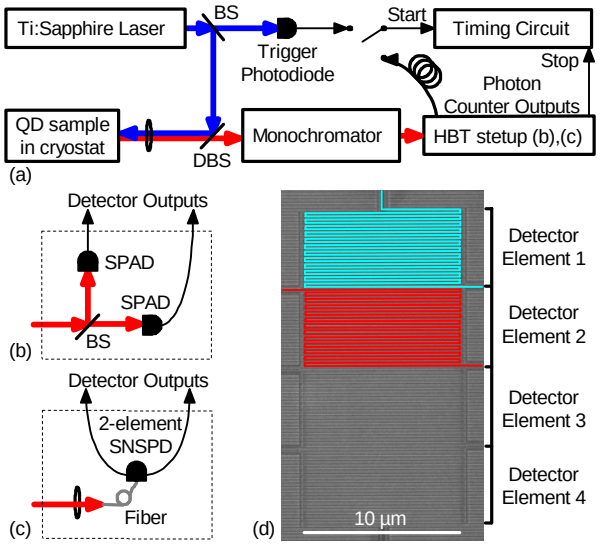

Figure 6.5: (a) Experimental schematic for the instrument response function and photoluminescene lifetime measurements (start input connected to the trigger photodiode) and the $g^{(2)}(\tau)$ measurements (start input connected to the photon counter). BS = beamsplitter; DBS = dichroic beamsplitter. Schematic of the Hanbury Brown-Twiss setup using (b) a free-space beamsplitter and two discrete single-photon avalanche diodes (SPADs) and (c) a fiber-coupled two-element SNSPD. A scanning-electron micrograph of the SNSPD is shown in (d) with two of the elements highlighted for clarity. The fiber is aligned to the best two adjacent elements.

SNSPD in section 6.1.1 with an optical fiber aligned just above the detector [19], in a mount modified to include two coaxial electrical connectors, wirebonded to the two elements on which the fiber was centered. The detector package was installed and operated at a stable, ~3 K temperature in a closed-cycle cryocooler.

6.2.2 Second-order intensity correlation measurement results

The instrument response function (IRF) of each of the detectors and the PL lifetime of the quantum dot were first measured. To measure the IRFs, the detectors were illuminated with Ti:Sapphire laser pulses (monochromator tuned to 779 nm) and for the PL measurements, the 959.7 nm monochromator-filtered output from the quantum dot sample was used (Fig. 6.5(a)). The output from an illuminated detector was then connected to the start channel of the Picoquant

PicoHarp 300 TCSPC hardware, and a portion of the light from the Ti:Sapphire laser was focused onto a fast photodiode connected to the stop channel.

The results for one SPAD and one SNSPD are shown in Fig. 6.6; nearly identical results were achieved using the other SPAD and the other SNPSD (not shown). The SNSPD has a narrower IRF than the SPAD, with no measurable tail, and consequently can resolve the PL lifetime of the quantum dot easily without deconvolution techniques. Although deconvolution may allow PL lifetimes equal to or even shorter than the detector IRF to be accurately measured, and SPADs with narrower IRF full-width half maximum (FWHM) than the ones used in these experiments are available, the SNSPD's narrow, Gaussian-shaped IRF is ideally suited to PL lifetime measurements [99].

Second-order temporal intensity correlations were also measured using either the two-element SNSPD or the two SPADs. The same setup (Fig. 6.5) was used in this case, except the start channel of the timing circuit was connected to the output from the second SPAD or the

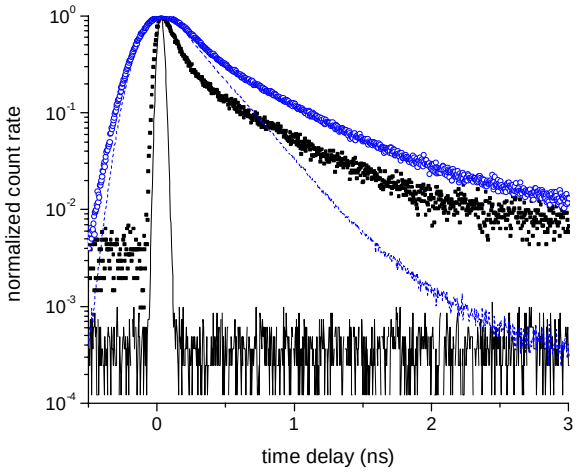

Figure 6.6: Measurements of IRFs (SNSPD: black solid line; SPAD: blue dotted line) and PL lifetimes (SNSPD: black solid squares; SPAD: blue open circles). The 50 ps-FWHM, Gaussian-shaped SNSPD IRF allows the quantum dot lifetime to be measured more accurately.

second element of the SNSPD, rather than the trigger photodiode, and a ~100 ns-long coaxial cable was used to delay the stop, to permit measuring correlations with both positive and negative time delays. A truly single-mode fiber (at 780 and 960 nm wavelength) would have ensured that both detector elements were illuminated with the same spatial mode, but the fiber used (single-mode at 1550 nm wavelength) could support more than one spatial mode at the wavelengths of interest. Instead, the lack of spatial correlations in the sources investigated here helped ensure that only temporal correlations were measured. An interleaved detector design is preferable in the future to ensure that both elements sample the same spatial mode(s).

The measured intensity correlations for the quantum dot single-photon source are shown in Fig. 6.7(a)-(b), and the intensity correlations of the Ti:Sapphire laser are shown in Fig. 6.7(c)-(d), with the monochromator tuned to the same wavelengths used for the PL and IRF measurements. The pulsed (non-stationary) source resulted in peaks in the intensity correlation histogram at time delays corresponding to the pulse repetition period. The widths of the

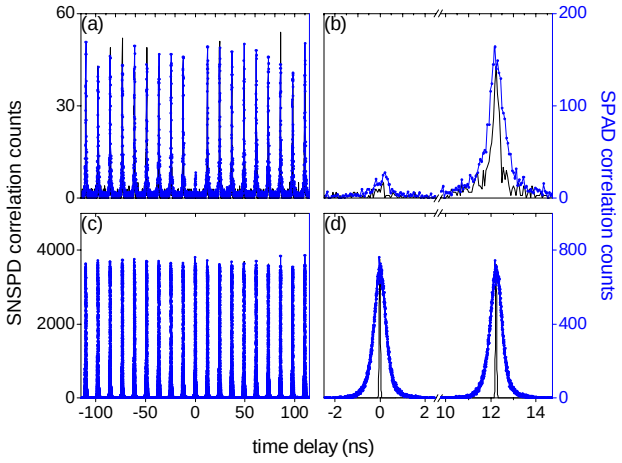

Figure 6.7: Measured intensity-correlation histograms for the quantum dot single-photon source (a),(b) and the Ti:Sapphire laser (c),(d). The measurements were made with the two-element SNSPD (solid black lines) and, subsequently, with the SPAD-based HBT setup (blue lines with filled circles). The shape and width of the peaks demonstrate that the two-element SNSPD may be used to achieve improved timing resolution, while the setup-independent ratio of counts in the zero-time-delay peak relative to the counts in the other peaks demonstrates that both detector setups can be used to accurately measure $g^{(2)}(0)$.

correlation peaks measured with the SNSPD are limited by the IRF for the pulsed laser (Fig. 6.7(b)) and by the PL lifetime for the quantum dot (Fig. 6.7(d)). The narrow IRF of the SNSPD provides a high-resolution measurement of the photon correlations from the quantum dot, and allows correlations with time delays less than the PL lifetime to be examined, which cannot be resolved with the SPAD due to its long IRF.

The pulsed nature of the source also requires $g^{(2)}(0)$ to be calculated differently than in a stationary source: here, $g^{(2)}(0)$ is calculated by dividing the total number of counts in the peak at zero time delay by the average number of counts in peaks at nonzero time delays. The data for nine peaks on each side of zero delay are plotted (Fig. 6.7(a),(c)) and used to calculate $g^{(2)}(0)$, since this was a reasonable compromise between minimizing statistical variations and minimizing the systematic decrease in coincidences at later time delays (some long-delay coincidence events were blocked due to the single-stop TCSPC hardware). To test the long-term stability of the measurement, data sets were taken with the SPADs both before and after acquiring data with the two-element SNSPD. Integrating the number of counts in a 2.4 ns window centered on the quantum dot intensity correlation peaks, we calculated $g^{(2)}(0)$ values (no background subtraction) using the SPADs of 0.10 ± 0.01 before and 0.15 ± 0.01 after the value of 0.12 ± 0.02 that was measured with the two-element SNSPD. Ideally, all three measurements would yield an identical value of $g^{(2)}(0)$; however, the two different results with SPADs indicated that $g^{(2)}(0)$ of the quantum dot source increased slightly over the course of the measurements. This increase was most likely due to small drifts in quantum dot temperature and alignment with respect to the pump beam. Such drift can lead to small changes in the fraction of light incident on the detectors originating from the desired quantum dot emission line, relative to light from other emission lines from this or another quantum dot in the same micropillar. Even with this drift, the SNSPD result agreed with both results using SPADs, within the experimental uncertainties. Our inability to completely remove light from other emission lines was responsible for the measured nonzero values of $g^{(2)}(0)$.

Similarly, integrating the counts in a 1.6 ns window for the Ti:Sapphire laser data resulted in $g^{(2)}(0)$ values of 1.003 ± 0.003 using the SPADs and 0.995 ± 0.004 using the two-element SNSPD. In all cases, the uncertainties accounted only for predicted statistical variations due to

the finite number of measured correlation counts (see Ref. 96) and not any systematic errors such as drift or detector and electronic dead times. Nevertheless, both of the laser measurements were in agreement with the expected $g^{(2)}(0) = 1$, roughly within the expected statistical variation, and all the quantum dot measurements were consistent with a slow drift in the setup.

This agreement in measured $g^{(2)}(0)$ for the two techniques demonstrated that the two-element SNSPD did not exhibit measurable crosstalk or introduce other measurement artifacts, which would have altered the correlation counts at short time delays by increasing (or decreasing, depending on the mechanism) the probability of a nearly simultaneous switching event in the adjacent element. Furthermore, the agreement in $g^{(2)}(0)$, along with the lack of significant counts between peaks in the correlation histograms, indicated that the SNSPD dark count rates were sufficiently low to permit measurements without background subtraction, as shown previously for single-element SNSPDs [96, 98]. Finally, it should be noted that the low crosstalk demonstrated in section 6.1 was critical to accurately measuring the intensity correlations. Even a $\sim 0.0002\%$ crosstalk probability would have resulted in approximately doubling the measured $g^{(2)}(0)$ of the quantum dot.

6.3 Third-order Intensity Correlation Measurements

While a two-element SNSPD provides some advantages relative to a conventional Hanbury Brown-Twiss interferometer with a beamsplitter for measuring second-order intensity correlations, the multi-element SNSPD approach becomes even more advantageous for measuring higher-order intensity correlations. Higher-order intensity correlations are typically not measured because of their added complexity, even though they can provide additional information that cannot be derived, or is difficult to accurately measure, using second-order intensity correlations alone [100]. In fact, there is believed to be no published report of higher-order intensity correlations measured at zero-time delay with photon-counting detectors because published intensity correlation measurements have been performed with only one or two detectors that have non-zero deadtimes. The added complexity of using more than two detectors to make higher-order intensity correlation measurements is reduced, and the potential artifacts

and alignment difficulties associated with a network of optical beamsplitters are eliminated, by using multi-element SNSPDs. Consequently, higher-order intensity correlation measurements may be more widely measured if the multi-element SNSPD approach is demonstrated. In this section, third-order intensity correlations of a laser above threshold and a pseudo-thermal source will be investigated using a 4-element SNSPD.

6.3.1 Third-order intensity correlation measurement setup and detectors

The 4-element SNSPD used to perform these measurements was the same detector and package used in section 6.1.2 to demonstrate the negligible crosstalk. The fiber that had been previously blocked was instead illuminated with light from the optical sources that will be described below. The output from each of the four elements was amplified and connected to the inputs of the HydraHarp 400, although in this instance the software only analyzed the cross correlations between three of the four channels to measure third-order correlations [90].

The two optical sources considered in the work were a continuous-wave, 1060 nm wavelength, external-cavity laser and a pseudo-thermal source made using the same laser and a spinning piece of ground glass [101]. The laser was operated well above threshold, attenuated and coupled into an optical fiber (single mode at 1550 nm, but not at 1060 nm). The attenuation of the laser was adjusted so that each element detected ~10^5 photons per second. The pseudo-thermal source was generated by reflecting this laser light off of a piece of ground glass (the rough surface of the quartz from the back of a mirror) attached to a spinning fan, and then coupling the light into a fiber. The scattered light from the rough surface was not efficiently coupled into the fiber and no lens was used to improve this coupling – it was important to collect light from only a single speckle of the granular interference pattern. This large fiber coupling loss was used in place of attenuation to obtain the low, ~10^5 photons per second, count rate desired in each detector element.

6.3.2 Third-order intensity correlation measurement results

The third order intensity correlation is defined as:

$$g^{(3)}(\tau_1,\tau_2)=\frac{\left\langle :\hat{I}(t)\hat{I}(t+\tau_1)\hat{I}(t+\tau_2):\right\rangle}{\left\langle \hat{I}(t)\right\rangle^3} \tag{6-7}$$

where τ_1 and τ_2 are two independent time delays, which will require that we plot $g^{(3)}(\tau_2, \tau_1)$ in three dimensions. Since $g^{(3)}(\tau_1, \tau_2) = g^{(3)}(\tau_2, \tau_1) = g^{(3)}(\pm\tau_1, \pm\tau_2)$, we should expect to see these symmetries in the measured third-order correlations (results that are not symmetric in this way are not due to intensity correlations in the source, and must be due to noise or differences in the optical modes coupled into each detector).

The third-order correlations were calculated using software similar to that used for measuring the crosstalk in the detectors [90]. However, in the case of a third-order correlation, the number of correlation counts were defined as the number of times that both a count in detector *C* occurred after a count in detector *B* within a time delay between $\tau_1 - \Delta\tau_0/2$ and $\tau_1 + \Delta\tau_0/2$ and a count in detector *B* occurred after a count in detector *A* within a time delay between $\tau_2 - \Delta\tau_0/2$ and $\tau_2 + \Delta\tau_0/2$. These correlation counts were then normalized by the expected number of correlation counts assuming the count events were independent Poisson processes (i.e. the product of $(\Delta\tau_0)^3$ and the count rate from each of three detector elements).

The normalized third-order correlations are plotted for the laser in Fig. 6.8. As expected [93], the intensity correlations for the laser were relatively flat and the observed variations in the intensity correlations are dominated by statistical noise. However, if it were assumed that the intensity correlations were perfectly flat and the measured variation of $g^{(3)}$ between the time bins ($\sigma = 0.011$) was due to statistical noise alone, we would conclude that the average $g^{(3)}(\tau_1, \tau_2) = 1.00524 \pm 0.00005$, which is greater than one by many standard deviations. Consequently, it is clear that there is some correlation in the source, perhaps due to slow variations in the intensity of the laser, which could be further investigated by widening the time window over which $g^{(3)}$ is examined.

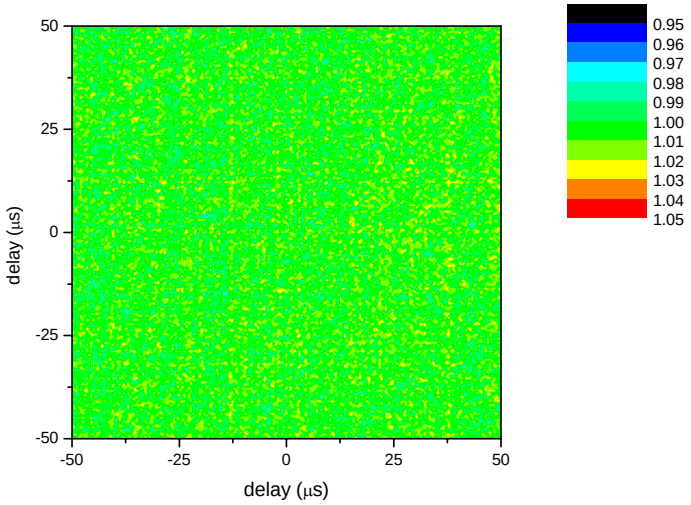

Figure 6.8: Measured $g^{(3)}(\tau_1, \tau_2)$ for a continuous-wave laser well above threshold. As expected [93], the distribution is very flat, with $g^{(3)}(\tau_1, \tau_2) \approx 1$. The primary features in the measured $g^{(3)}(\tau_1, \tau_2)$ are due to statistically noise as they are not in general symmetric across $\tau_1 = 0$, $\tau_2 = 0$, and $\tau_1 = \tau_2$. The visible patterning (the faint vertical, horizontal and diagonal stripes of higher or lower $g^{(3)}$) are likely features of the statistical noise (once a statistically high or low number of second-order cross-correlation counts occur at some delay, this will affect the probability of third-order correlations at all values of the second time delay), and are not due to correlations in the laser source or detectors.

Additionally, the measured third-order intensity correlations from the pseudo-thermal source are shown in Fig. 6.9(a), which closely match the calculations shown in Fig. 6.9(b) [100, 102]. Away from the three stripes of higher correlation (which occur along $\tau_1 = 0$, $\tau_2 = 0$ and $\tau_1 = \tau_2$), theory predicts that $g^{(3)}(\tau_1, \tau_2; \text{given } |\tau_1| >> \tau_c \text{ and } |\tau_2| >> \tau_c) = 1$ because the source should be uncorrelated at times much longer than the source coherence time, τ_c. Along the three stripes of higher correlation, but away from the point of intersection, we would expect $g^{(3)}(\tau_1, 0; \text{given} |\tau_1| >> \tau_c) = g^{(3)}(0, \tau_2; \text{given} |\tau_2| >> \tau_c) = g^{(3)}(\tau_1, \tau_2; \text{given} |\tau_1| >> \tau_c \text{ and } \tau_2 = \tau_1) = g^{(2)}(0) = 2$, because of the bunching inherent to the chaotic source. More precisely, we can extract $g^{(2)}(\tau)$ from $g^{(3)}(\tau_1, \tau_2)$ by integrating along τ_1, τ_2 or $\tau_1 = \tau_2$. At the point of intersection, we would expect $g^{(3)}(0, 0) = 6$, or in general, $g^{(n)}(0, \ldots 0) = n!$ [100]. Based on a subset of data, assuming that the only variations between measurements are due to statistical noise, the measurements suggest $g^{(3)}(\tau_1, \tau_2; \text{given} |\tau_1| >> \tau_c \text{ and } |\tau_2| >> \tau_c) = 1.0264 \pm 0.0002$, $g^{(2)}(0) = 1.991 \pm 0.001$ and $g^{(3)}(0, 0) = 5.65 \pm 0.03$. The variations between the theoretical and measured values are likely due to a combination of correlations in the laser source (which tend to increase the cross-correlations)

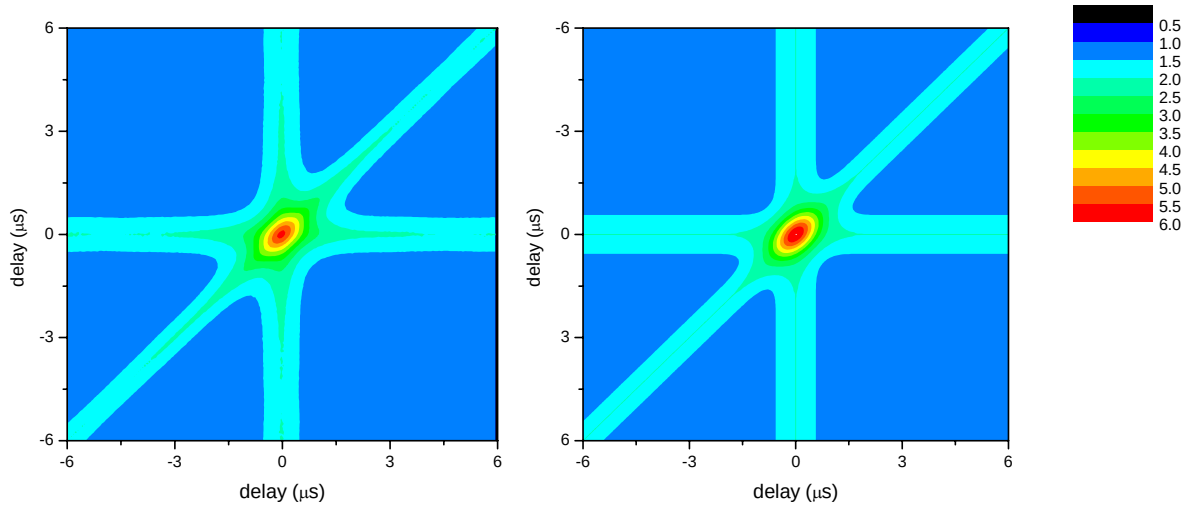

(a) (b)

Figure 6.9: The (a) measured and (b) calculated [100,102] $g^{(3)}(\tau_1, \tau_2)$ for a pseudo-thermal source. Although the agreement between the measurement and predictions is excellent, the dominant residual differences do not appear to be the result of statistical noise or detector non-idealities, but are instead inherent to the pseudo-thermal source, as operated in the measurement (i.e. scattering material, rotation speed, illumination and fiber collection conditions, etc.)

and averaging over multiple polarization or spatial modes from the pseudo-thermal source (which tend to reduce the peaks in the cross-correlations).

6.4 Summary

In summary, multi-element SNSPDs exhibited extremely low crosstalk and cross-correlations, making them useful for accurate intensity correlation measurements. The crosstalk and cross-correlations between detector elements were examined without optical illumination in order to provide the most-sensitive possible measurement of their potential interactions. After finding and correcting a design issue, the cross-correlation between interleaved detector elements was measured to be roughly within the statistical noise of the measurements, with an unmeasurable level of crosstalk below 0.00001%. This result is quite surprising at first glance given that alternative single-photon detector arrays all exhibit higher levels of crosstalk, even though their elements are spaced much more widely than tens of nanometers apart. The low level of crosstalk

in SNSPDs is likely due to a unique combination of attributes, including (1) the small bandgap in the superconductor (preventing the emission of secondary photons, which are a problem in GM-APD arrays [56-57]), (2) the relatively low voltage levels (hundreds of microvolts, as opposed to volts in GM-APDs or kilovolts in PMTs and MCPs [65]), (3) the strong confinement of the electrons to the wires (due to the difference in resistivity between the wires and the surrounding medium, and the low voltages), (4) the nature of potential interactions due to phonons and (5) the digital mode of operation. Phonon interactions are restricted by their relatively low energy (at most tens of milli-electron volts, compared to electron volts for optical photons), their ballistic motion in the substrate and the digital operation of the detectors. Consequently, it is very unlikely that enough phonons will be absorbed in a sufficiently confined volume and short amount of time by an adjacent nanowire to result in a switching event, in the same way that the detectors are very insensitive to low-energy photons. The digital operation of the detectors also makes them relatively immune to small amounts of crosstalk in the readout, unlike analog superconducting single-photon detectors [66-67].

The multi-element SNSPDs were then used to measure intensity correlations without the need for an optical beamsplitter, which offers several advantages over a free-space HBT interferometer. The first advantage is the multi-element approach simplifies varying the measurement wavelength over a wide range by requiring only a simple adjustment to the monochromator and the single necessary fiber. In the case of a standard HBT interferometer, it is important to ensure both detectors are sampling the same spatial mode(s), which can be challenging with multi-mode sources, and it is also important to consider the range of wavelengths over which the beamsplitter and optical coatings are suitable, in order to prevent artifacts from backreflected photons in the interferometer. Furthermore, the broadband spectral response of SNSPDs and the lack of wavelength-dependent components make it easy to measure wavelengths throughout the visible and near-infrared. Second, measurements of sources at telecommunication wavelengths could benefit from the low dark count rate, short reset time and continuous mode of detector operation. The smaller, low-inductance SNSPDs inherent to the multi-element design enable precise timing resolution and fast reset times that will be critical for measuring high-rate, non-classical sources such as parametric downconversion sources. Finally,

measurements of higher-order correlation functions were possible using a detector with four elements. Third-order intensity correlation measurements were discussed in section 6.3 and fourth-order intensity correlations have also been measured recently using the 4-element SNSPD. In summary, multi-element SNSPDs were demonstrated that enable intensity-correlation measurements over a wide spectral and temporal range with high-speed, precise timing, and minimal potential for measurement artifacts because of their extremely low crosstalk.

Chapter 7

Summary and Future Directions

This thesis investigated one approach to increasing the performance of superconducting nanowire single photon detectors. The multi-element approach developed in this work combined the advantages of small arrays with the advantages of a single optical active area to produce a detector that outperforms either of the approaches independently. This multi-element approach permitted (1) faster reset times, with reduced deadtime effects, (2) photon-number-resolution, with independent 30 ps timing resolution of each detected photon, and (3) reduced detrimental effects from constrictions (defects) in the detector active area. Crosstalk between detector elements typically limits how closely single-photon-detector elements can be spaced, but this work demonstrated that nanowires can be arranged with gaps as small as 60 nm along long interaction lengths with negligible crosstalk. This level of performance allowed multi-element SNSPDs to be used to measure second- and third-order intensity correlations without measurement artifacts due to the detectors.

In addition to the work on demonstrating, investigating and optimizing multi-element SNSPDs that were the primary focus of this thesis, several efforts were also pursued to progress SNSPD technology in general. Many of these efforts were focused on improving the fabrication and providing feedback to improve the superconducting film deposition processes. Several techniques, including continuous ground planes, dynamic focus correction of the electron-beam lithography tool and improved techniques for dicing and cleaning detector chips for fabrication were introduced. Furthermore, the fabrication methods were tested on several alternative superconducting materials, including TaN and VN, as well as alternative substrates, including various orientations of sapphire, magnesium oxide, gallium nitride, oxidized silicon, and dielectric mirrors on quartz. Although NbN on r-plane sapphire remains the material of choice for most applications, several interesting new directions have been discovered. Finally, and perhaps most importantly, a film deposition process, material characterization and fabrication

process were established that permit the fabrication of SNSPDs with high yield due to drastically lower densities of defects.

One of the most important future directions for SNSPD research is the development of larger arrays. This thesis resolved many of the potential detector limitations to building such arrays, including obtaining sufficiently high yield and reducing crosstalk between detector elements to acceptable levels. The primary remaining challenge to scaling to larger array sizes is to build a readout-integrated circuit capable of multiplexing the output from the array elements onto a limited number of readout lines. This will be a very challenging problem, particularly as this readout is pushed to preserve the high SNSPD performance, scaled to large array sizes, and optimized to work at high count rates. The required bandwidth to achieve 30 ps timing resolution suggests that a time-multiplexed, as opposed to a frequency-multiplexed, approach would be more suitable. Furthermore, the digital nature of the output signal from the SNSPDs can be best matched with digital logic capable of operating at cryogenic temperatures, such as superconducting rapid single-flux-quantum (RSFQ) logic or cryogenic-compatible complementary metal-oxide-semiconductor (CMOS) logic. Limiting the heat dissipation from such circuits, transforming or amplifying the relatively small output signals from the SNSPDs and providing the high bandwidths desired will be just a few of the difficult problems that must be addressed to make a high-performance readout for SNSPD arrays. Fortunately, the work in this thesis demonstrates that the detectors will perform well in an array format if a suitable readout can be demonstrated. With an ideal readout, SNSPD arrays would far exceed any competing single-photon-detector arrays.

In addition to increasing the number of elements, improving the performance of multi-element detectors with only a few elements and discrete readout is another path to continue pursuing. The work with alterative materials suggests that by changing the substrate, improved optical absorption and improved thermal conductivity can be obtained. Improving the optical absorption would permit higher detection efficiencies, and with proper design of the nanowire elements, could permit polarization-insensitive detectors without sacrificing detection efficiency. Improving the thermal conductivity would permit faster detectors, by allowing higher series resistors or lower-inductance nanowires to be employed without latching. This could scale the

count rates from hundreds of millions per second to billions per second. However, more work will be required to reduce the defect densities that can be obtained on these alternative substrates. Furthermore, the extent to which changing the substrate negatively affects other performance parameters must also be investigated. Some applications, however, will not require that all of the performance parameters be maintained, nor is high yield necessarily required for few-element SNSPDs, so even the demonstrated instances of improved performance from alternative materials warrant further consideration.

Finally, even before larger arrays or higher-performance multi-element SNSPDs are developed, the multi-element SNSPDs demonstrated in this work can be used in new applications. A two-element SNSPD has already been used to demonstrate > 1 Gbit/s photon-counting optical communications [70], and multi-element SNSPDs are being pursued as the primary receiver for the Lunar Laser Communications Demonstration program at MIT Lincoln Laboratory. Multi-element SNSPDs should permit improved performance of quantum-key-distribution systems and could benefit many quantum optics experiments. Quantum optics experiments that require detecting multi-photon states may particularly benefit from the photon-number resolution provided by multi-element SNSPDs. Finally, laser ranging, optical-time-domain reflectometry and VLSI testing are also likely to benefit from the improved performance available from multi-element SNSPDs. The 4-element SNSPDs demonstrated in this thesis are the fastest, and among the highest detection efficiency, photon-counting detectors available. This level of performance may benefit not only existing photon-counting applications, but encourage new applications that make use of the unique high-speed, photon-number-resolution and infrared sensitivity provided by multi-element SNSPDs.

Bibliography

[1] G. Gol'tsman, O. Okunev, G. Chulkova, A. Lipatov, A. Dzardanov, K. Smirnov, A. Semenov, B. Voronov, C. Williams, and Roman Sobolewski, "Fabrication and Properties of an Ultrafast NbN Hot-Electron Single-Photon Detector, " *IEEE Transaction on Applied Superconductivity* **11**, 574-577 (2001).

[2] G. N. Gol'tsman, O. Okunev, G. Chulkova, A. Lipatov, A. Semenov, K. Smirnov, B. Voronov, A. Dzardanov, C. Williams, and R. Sobolewski, "Picosecond superconducting single-photon optical detector," *Applied Physics Letters* **79**, 705-707 (2001).

[3] A. Engel, A. Semenov, H. W. Hubers, K. Il'in, and M. Siegel, "Superconducting single-photon detector for the visible and infrared spectral range," *Journal of Modern Optics* **51**, 1459-1466 (2004).

[4] B. Delaet, J. C. Villegier, W. Escoffier, J. L. Thomassin, P. Feautrier, I. Wang, P. Renaud-Goud, and J. P. Poizat, "Fabrication and characterization of ultra-thin NbN hot electron bolorneter for near infrared single photon detection," *Nuclear Instruments & Methods in Physics Research Section A – Accelerators, Spectrometers, Detectors and Associated Equipment* **520**, 541-543 (2004).

[5] J. K. W. Yang, E. Dauler, A. Ferri, A. Pearlman, A. Verevkin, G. Gol'tsman, B. Voronov, R. Sobolewski, W. E. Keicher, and K. K. Berggren, "Fabrication development for nanowire GHz-counting-rate single-photon detectors," *IEEE Transactions on Applied Superconductivity* **15**, 626-630 (2005).

[6] A. J. Kerman, E. A. Dauler, W. E. Keicher, J. K. W. Yang, K. K. Berggren, G. Gol'tsman, and B. Voronov, "Kinetic-inductance-limited reset time of superconducting nanowire photon counters," *Applied Physics Letters* **88**, 111116 (2006).

[7] K. M. Rosfjord, J. K. W. Yang, E. A. Dauler, A. J. Kerman, V. Anant, B. M. Voronov, G. N. Gol'tsman, and K. K. Berggren, "Nanowire Single-photon detector with an integrated optical cavity and anti- reflection coating," *Optics Express* **14** 527-534, (2006).

[8] E. A. Dauler, B. S. Robinson, A. J. Kerman, J. K. W. Yang, K. M. Rosfjord, V. Anant, B. Voronov, G. Gol'tsman, and K. K. Berggren, "Multi-element superconducting nanowire single-photon detector," *IEEE Transactions on Applied Superconductivity* **17**, 279-284 (2007).

[9] S. Miki, M. Fujiwara, M. Sasaki, and Z. Wang, "NbN superconducting single-photon detectors prepared on single-crystal MgO substrates," *IEEE Transactions on Applied Superconductivity* **17**, 285-288 (2007).

[10] J. A. Stern, and W. H. Farr, "Fabrication and characterization of superconducting NbN nanowire single photon detectors," *IEEE Transactions on Applied Superconductivity* **17**, 206-309 (2007), pp. 306-309.

[11] F. Marsili, D. Bitauld, A. Fiore, A. Gaggero, F. Mattioli, R. Leoni, M. Benkahoul, and F. Levy, "High efficiency NbN nanowire superconducting single photon detectors fabricated on MgO substrates from a low temperature process," *Optics Express* **16**, 3191-3196 (2008).

[12] S. N. Dorenbos, E. M. Reiger, U. Perinetti, V. Zwiller, T. Zijlstra, and T. M. Klapwijk, *Applied Physics Letters* **93**, 131101 (2008).

[13] W. Slysz, M. W. Grzecki, J. Bar, P. Grabiec, M. Gorska, V. Zwiller, C. Latta, P. Bohi, A. J. Pearlman, A. S. Cross, D. Pan, J. Kitaygorsky, I. Komissarov, A. Verevkin, I. Milostnaya, A. Korneev, O. Minayeva, G. Chulkova, K. Smirnov, B. Voronov, G. N. Gol'tsman, and R. Sobolewski, "Fibre-coupled, single photon detector based on NbN superconducting nanostructures for quantum communications," *Journal of Modern Optics* **54**, 315-326 (2007).

[14] A. Korneev, O. Minaeva, I. Rubtsova, I. Milostnaya, G. Chulkova, B. Voronov, K. Smirnov, V. Seleznev, G. Gol'tsman, A. Pearlman, W. Slysz, A. Cross, P. Alvarez, A. Verevkin, and R. Sobolewski, "Superconducting single-photon ultrathin NbN film detector," *Quantum Electronics* **35**, 698-700 (2005).

[15] I. Milostnaya, A. Korneev, M. Tarkhov, A. Divochiy, O. Minaeva, V. Seleznev, N. Kaurova, B. Voronov, O. Okunev, G. Chulkova, K. Smirnov, and G. Gol'tsman, "Superconducting single photon nanowire detectors development for IR and THz applications," *Journal of Low Temperature Physics* 151, 591-596 (2008).

[16] J. Zhang, N. Boiadjieva, G. Chulkova, H. Deslandes, G. N. Gol'tsman, A. Korneev, P. Kouminov, A. Leibowitz, W. Lo, R. Malinsky, O. Okunev, A. Pearlman, W. Slysz, K. Smirnov, C. Tsao, A. Verevkin, B. Voronov, K. Wilsher, and R. Sobolewski, "Noninvasive CMOS circuit testing with NbN superconducting single-photon detectors," *Electronics Letters* **39**, 1086-1088 (2003).

[17] B. S. Robinson, A. J. Kerman, E. A. Dauler, R. O. Barron, D. O. Caplan, M. L. Stevens, J. J. Carney, S. A. Hamilton, J. K. W. Yang, and K. K. Berggren, "781 Mbit/s photon-counting optical communications using a superconducting nanowire detector," *Optics Letters* **31**, 444-446 (2006).

[18] H. Takesue, S. W. Nam, Q. Zhang, R. H. Hadfield, T. Honjo, K. Tamaki, and Y. Yamamoto, "Quantum key distribution over a 40-dB channel loss using superconducting single-photon detectors," *Nature Photonics* **1**, 343-348 (2007).

[19] R. H. Hadfield, M. J. Stevens, S. S. Gruber, A. J. Miller, R. E. Schwall, R. P. Mirin, and S. W. Nam, "Single photon source characterization with a superconducting single photon detector," *Optics Express* **13**, 10846-10853 (2005).

[20] M. Halder, A. Beveratos, N. Gisin, V. Scarani, C. Simon, and H. Zbinden, "Entangling

independent photons by time measurement," *Nature Physics* **3**, 692-695 (2007).

[21] R. E. Warburton, A. McCarthy, A. M. Wallace, S. Hernandez-Marin, R. H. Hadfield, S. W. Nam, and G. S. Buller, "Subcentimeter depth resolution using a single-photon counting time-of-flight laser ranging system at 1550 nm wavelength," *Optics Letters* **32**, 2266-2268 (2007).

[22] A. M. Kadin, and M. W. Johnson, "Nonequilibrium photon-induced hotspot: A new mechanism for photodetection in ultrathin metallic films," *Applied Physics Letters* **69**, 3938-3940 (1996).

[23] J. K. W. Yang, A. J. Kerman, E. A. Dauler, V. Anant, K. M. Rosfjord, and K. K. Berggren, "Modeling the electrical and thermal response of superconducting nanowire single-photon detectors," *IEEE Transactions on Applied Superconductivity* **17**, 581-585 (2007).

[24] A. J. Kerman, J. K.W. Yang, R. J. Molnar, E. A. Dauler, and K. K. Berggren, unpublished.

[25] A. J. Annunziata, D. F. Santavicca, J. Chudow, L. Frunzio, D. E. Prober, M. J. Rooks, and A. Frydman, "Niobium Nanowire Single-Photon Detectors, " presented at the *Applied Superconductivity Conference*, Chicago, IL USA (2008).

[26] A. Pearlman, A. Cross, W. Slysz, J. Zhang, A. Verevkin, M. Currie, A. Korneev, P. Kouminov, K. Smirnov, B. Voronov, G. Gol'tsman, and R. Sobolewski, "Gigahertz counting rates of NbN single-photon detectors for quantum communications," *IEEE Transactions on Applied Superconductivity* **15**, 579-582 (2005).

[27] J. Zhang, W. Slysz, A. Pearlman, A. Verevkin, R. Sobolewski, O. Okunev, G. Chulkova, and G. N. Gol'tsman, "Time delay of resistive-state formation in superconducting stripes excited by single optical photons," *Physical Review B* **67** (2003).

[28] A. D. Semenov, G. N. Gol'tsman, and A. A. Korneev, "Quantum detection by current carrying superconducting film," *Physica C* **351**, 349-356 (2001).

[29] A. D. Semenov, P. Haas, H. W. Huebers, K. Ilin, M. Siegel, A. Kirste, T. Schurig, and A. Engel, "Vortex-based single-photon response in nanostructured superconducting detectors," *Physica C* **468,** 627-630 (2008).

[30] A. Andronov, I. Gordion, V. Kurin, I. Nefedov, and I. Shereshevsky, "Kinematic vortices and phase-slip lines in the dynamics of the resistive state of narrow superconductive thin-film channels," *Physica C* **213**, 193-199 (1993).

[31] A. Korneev, P. Kouminov, V. Matvienko, G. Chulkova, K. Smirnov, B. Voronov, G. N. Gol'tsman, M. Currie, W. Lo, K. Wilsher, J. Zhang, W. Slysz, A. Pearlman, A. Verevkin, and R. Sobolewski, "Sensitivity and gigahertz counting performance of NbN superconducting single-photon detectors," *Applied Physics Letters* **84**, 5338-5340 (2004).

[32] G. Gol'tsman, O. Minaeva, A. Korneev, M. Tarkhov, I. Rubtsova, A. Divochiy, I. Milostnaya, G. Chulkova, N. Kaurova, B. Voronov, D. Pan, J. Kitaygorsky, A. Cross, A. Pearlman, I. Komissarov, W. Slysz, M. Wegrzecki, P. Grabiec, and R. Sobolewski, "Middle-

infrared to visible-light ultrafast superconducting single-photon detectors," *IEEE Transactions on Applied Superconductivity* **17**, 246-251 (2007).

[33] A. J. Kerman, E. A. Dauler, J. K. W. Yang, K. M. Rosfjord, V. Anant, K. K. Berggren, G. N. Gol'tsman, and B. M. Voronov, "Constriction-limited detection efficiency of superconducting nanowire single-photon detectors," *Applied Physics Letters* **90,** 101110 (2007).

[34] R. H. Hadfield, P. A. Dalgarno, J. A. O'Connor, E. Ramsay, R. J. Warburton, E. J. Gansen, B. Baek, M. J. Stevens, R. P. Mirin, and S. W. Nam, "Submicrometer photoresponse mapping of nanowire superconducting single-photon detectors," *Applied Physics Letters* **91,** 241108 (2007).

[35] V. Anant, A. J. Kerman, E. A. Dauler, J. K.W. Yang, K. M. Rosfjord, and K. K. Berggren, "Optical properties of superconducting nanowire single-photon detectors, " *Optics Express* **16**, 10750 (2008).

[36] V. Anant. "Engineering the optical properties of subwavelength devices and materials," Ph.D. thesis, Massachusetts Institute of Technology (2007).

[37] A. J. Kerman designed and assembled the closed-cycle cryocooler setup for operating SNSPDs with optical illumination from a nanopositioner-controlled fiber and lens assembly.

[38] E. A. Dauler, A. J. Kerman, B. S. Robinson, J. K. W. Yang, B. Voronov, G. Gol'tsman, S. A. Hamilton, and K. K. Berggren, "Photon-number-resolution with sub-30-ps timing using multi-element superconducting nanowire single photon detectors, " *Journal of Modern Optics*, in press.

[39] V. K. Zworykin, G. A. Morton, and L. Malter, "The secondary-emission multiplier-a new electronic device," *Proc. IRE* 2**4**, 351-375 (1936).

[40] Wiza, Joseph, "Microchannel plate detectors," *Nuclear Instruments and Methods* **162**, 587-601 (1979).

[41] Ultra Fast Photomultipiers Data Sheet, Photek Ltd., East Sussex, United Kingdom; http://www.photek.co.uk

[42] E. Hergert, "Near-infrared photodetectors enable new applications," *Laser Focus World* **40**, 131-133 (2004).

[43] R. A. LaRue, K. A. Costello, G. A. Davis, J. P. Edgecumbe, and V. W. Aebi, "Photon counting III-V hybrid photomultipliers using transmission mode photocathodes," *IEEE Transactions on Electron Devices* **44**, 672-678 (1997).

[44] M. Ghioni, A. Gulinatti, I. Rech, F. Zappa, and S. Cova, "Progress in silicon single-photon avalanche diodes," *IEEE Journal of Selected Topics in Quantum Electronics* **13**, 852-862 (2007).

[45] SPCM-AQR Single Photon Counting Module Data Sheet, Perkin Elmer Optoelectronics Canada Ltd., Vaudreuil, Quebec, Canada; http://optoelectronics.perkinelmer.com

[46] M. A. Itzler, R. Ben-Michael, C. F. Hsu, K. Slomkowski, A. Tosi, S. Cova, F. Zappa, and R. Ispasoiu, "Single photon avalanche diodes (SPADs) for 1.5 mu m photon counting applications," *Journal of Modern Optics* **54**, 283-304 (2007).

[47] J. P. Donnelly, E. K. Duerr, K. A. McIntosh, E. A. Dauler, D. C. Oakley, S. H. Groves, C. J. Vineis, L. J. Mahoney, K. M. Molvar, P. I. Hopman, K. E. Jensen, G. M. Smith, S. Verghese, and D. C. Shaver, "Design considerations for 1.06-mu m InGaAsP-InP Geiger-mode avalanche photodiodes," *IEEE Journal of Quantum Electronics* **42**, 797-809 (2006).

[48] J. Kim, S. Takeuchi, Y. Yamamoto, and H. H. Hogue, "Multiphoton detection using visible light photon counter," *Applied Physics Letters* **74,** 902-904 (1999).

[49] B. Cabrera, R. M. Clarke, P. Colling, A. J. Miller, S. Nam, and R. W. Romani, "Detection of single infrared, optical, and ultraviolet photons using superconducting transition edge sensors," *Applied Physics Letters* **73**, 735-737 (1998).

[50] A. Peacock, P. Verhoeve, N. Rando, A. vanDordrecht, B. G. Taylor, C. Erd, M. A. C. Perryman, R. Venn, J. Howlett, D. J. Goldie, J. Lumley, and M. Wallis, "Single optical photon detection with a superconducting tunnel junction," *Nature* **381**, 135-137 (1996).

[51] B. A. Mazin, M. E. Eckart, B. Bumble, S. Golwala, P. K. Day, J. Gao, and J. Zmuidzinas, "Optical/UV and x-ray microwave kinetic inductance strip detectors," *Journal of Low Temperature Physics* **151**, 537-543 (2008).

[52] D. Rosenberg, A. E. Lita, A. J. Miller, and S. W. Nam, "Noise-free high-efficiency photon-number-resolving detectors," *Physical Review A* **71**, 061803 (2005).

[53] S. T. Hess, S. H. Huang, A. A. Heikal, and W. W. Webb, "Biological and chemical applications of fluorescence correlation spectroscopy: A review," *Biochemistry* **41**, 697-705 (2002).

[54] W. Becker, A. Bergmann, M. A. Hink, K. Konig, K. Benndorf, and C. Biskup, "Fluorescence lifetime imaging by time-correlated single-photon counting," *Microscopy Research and Technique* **63**, 58-66 (2004).

[55] J. C. Mather, "Astronomy - Super photon counters," *Nature* **401**, 654-655 (1999).

[56] A. Rochas, M. Gosch, A. Serov, P. A. Besse, R. S. Popovic, T. Lasser, and R. Rigler, "First fully integrated 2-D array of single-photon detectors in standard CMOS technology," *IEEE Photonics Technology Letters* **15**, 963-965 (2003).

[57] S. Verghese, J. P. Donnelly, E. K. Duerr, K. A. McIntosh, D. C. Chapman, C. J. Vineis, G. M. Smith, J. E. Funk, K. E. Jensen, P. I. Hopman, D. C. Shaver, B. F. Aull, J. C. Aversa, J. P. Frechette, J. B. Glettler, Z. L. Liau, J. M. Mahan, L. J. Mahoney, K. M. Molvar, F. J. O'Donnell, D. C. Oakley, E. J. Ouellette, M. J. Renzi, and B. M. Tyrrell, "Arrays of InP-based avalanche photodiodes for photon counting," *IEEE Journal of Selected Topics in Quantum Electronics* **13**, 870-886 (2007).

[58] J. G. Timothy, and R. L. Bybee, "2-Dimensional photon-couting detector arrays based on microchannel array plates," *Review of Scientific Instruments* **46**, 1615-1623 (1975).

[59] R. Bellazzini, G. Spandre, M. Minuti, A. Brez, L. Baldini, L. Latronico, N. Omodei, C. Sgro, J. Bregeon, M. Razzano, M. Pinchera, A. Tremsin, J. McPhate, J. V. Vallerga, and O. Siegmund, "Single photon imaging at ultra-high resolution," *Nuclear Instruments & Methods in Physics Research Section a-Accelerators Spectrometers Detectors and Associated Equipment* **591**, 125-128 (2008).

[60] J. A. Chervenak, K. D. Irwin, E. N. Grossman, J. M. Martinis, C. D. Reintsema, and M. E. Huber, "Superconducting multiplexer for arrays of transition edge sensors," *Applied Physics Letters* **74**, 4043-4045 (1999).

[61] K. D. Irwin, M. D. Audley, J. A. Beall, J. Beyer, S. Deiker, W. Doriese, W. Duncan, G. C. Hilton, W. Holland, C. D. Reintsema, J. N. Ullom, L. R. Vale, and Y. Z. Xu, "In-focal-plane SQUID multiplexer," *Nuclear Instruments & Methods in Physics Research Section a-Accelerators Spectrometers Detectors and Associated Equipment* **520**, 544-547 (2004).

[62] L. A. Jiang, E. A. Dauler, and J. T. Chang, "Photon-number-resolving detector with 10 bits of resolution," *Physical Review A* **75** 062325 (2007).

[63] A. Sharma, and J. G. Walker, "Paralyzable and nonparalyzable deadtime analysis in spatial photon-counting," *Review of Scientific Instruments* **63**, 5784-5793 (1992).

[64] K. D. Irwin, and K. W. Lehnert, "Microwave SQUID multiplexer," *Applied Physics Letters* **85**, 2107-2109 (2004).

[65] P. P. Manning, N. J. Clague, I. W. Kirkman, F. M. Quinn, and P. J. Hicks, "A fast and flexible multichannel electron detector with parallel readout for photoelectron spectroscopy," *Nuclear Instruments & Methods in Physics Research Section a-Accelerators Spectrometers Detectors and Associated Equipment* **392**, 345-348 (1997).

[66] J. A. Chervenak, E. N. Grossman, K. D. Irwin, J. M. Martinis, C. D. Reintsema, C. A. Allen, D. I. Bergman, S. H. Moseley, and R. Shafer, "Performance of multiplexed SQUID readout for Cryogenic Sensor Arrays," *Nuclear Instruments & Methods in Physics Research Section a-Accelerators Spectrometers Detectors and Associated Equipment* **444**, 107-110 (2000).

[67] A. Bozbey, M. Fardmanesh, J. Schubert, and M. Banzet, "Analytical modelling of the interpixel thermal crosstalk in superconducting edge-transition bolometer arrays," *Superconductor Science & Technology* **19**, 606-611 (2006).

[68] M. A. Albota, R. M. Heinrichs, D. G. Kocher, D. G. Fouche, B. E. Player, M. E. O'Brien, B. F. Aull, J. J. Zayhowski, J. Mooney, B. C. Willard, and R. R. Carlson, "Three-dimensional imaging laser radar with a photon-counting avalanche photodiode array and microchip laser," *Applied Optics* **41**, 7671-7678 (2002).

[69] M. Gosch, A. Serov, T. Anhut, T. Lasser, A. Rochas, P. A. Besse, R. S. Popovic, H. Blom, and R. Rigler, "Parallel single molecule detection with a fully integrated single-photon 2X2

CMOS detector array," *Journal of Biomedical Optics* **9**, 913-921 (2004).

[70] E. A. Dauler, B. S. Robinson, A. J. Kerman, V. Anant, R. J. Barron, K. K. Berggren, D. O. Caplan, J. J. Carney, S. A. Hamilton, K. M. Rosfjord, M. L. Stevens, J. K. Yang, "1.25 Gbit/s photon-counting optical communications using a two-element superconducting nanowire single photon detector, " *Proceedings of the SPIE*, **6372**, Advanced Photon Couhnting Techniques, Ed.: Wolfgang Becker, 637212 (2006).

[71] E. A. Dauler, M. J. Stevens, B. Baek, R. Molnar, S. A. Hamilton, R. P. Mirin, S. W. Nam, and K. K. Berggren, "Measuring intensity correlations with a two-element superconducting nanowire single photon detector, " *Physical Review A*, in press.

[72] D. Bitauld, F. Marsili, A. Fiore, A. Gaggero, F. Mattioli, R. Leoni, M. Benkahoul, F. Levy, "Spatially resolving characterisation of NbN nanowire superconducting single photon detectors fabricated on MgO substrates, " unpublished.

[73] A. D. Semenov, P. Haas, B. Gunther, H. W. Huebers, K. Il'in, M. Siegel, A. Kirste, J. Beyer, D. Drung, T. Schurig, and A. Smirnov, "An energy-resolving superconducting nanowire photon counter," *Superconductor Science & Technology* **20**, 919-924 (2007).

[74] M. Ejrnaes, R. Cristiano, O. Quaranta, S. Pagano, A. Gaggero, F. Mattioli, R. Leoni, B. Voronov, and G. Gol'tsman, "A cascade switching superconducting single photon detector," *Applied Physics Letters* **91**, 262509 (2007).

[75] E. A. Dauler, unpublished

[76] A. Divochiy, F. Marsili, D. Bitauld, A. Gaggero, R. Leoni, F. Mattioli, A. Korneev, V. Seleznev, N. Kaurova, O. Minaeva, G. Gol'tsman, K. G. Lagoudakis, M. Benkhaoul, F. Levy, and A. Fiore, "Superconducting nanowire photon-number-resolving detector at telecommunication wavelengths," *Nature Photonics* 2, 302-306 (2008).

[77] A. J. Kerman, unpublished

[78] J. K. W. Yang, "Fabrication of superconducting nanowire single proton detectors," M.S. thesis, Massachusetts Institute of Technology (2005).

[79] M. Hatzakis, B. J. Canavello, and J. M. Shaw, "Single-step optical lift-off process, " *IBM Journal of Research and Development*, **24**, 452–460 (1980).

[80] J. K. W. Yang, V. Anant, and K. K. Berggren, "Enhancing etch resistance of hydrogen silsesquioxane via postdevelop electron curing," *Journal of Vacuum Science and Technology B*, **24,** 3157-3161 (2006).

[81] S. Cherednichenko, P. Yagoubov, K. Il'in, G. N. Gol'tsman, and E. Gershenzon, "Large bandwidth of NbN phonon cooled hot-electron bolometer mixers on sapphire substrates," *Proceedings of the 8th International Symposium on Space Terahertz Technology*, 245-257 (1997).

[82] L. J. van der Pauw, "A method of measuring the resistivity and Hall coefficient on lamellae of arbitrary shape," *Philips Technical Review*, **20,** 220-224 (1958).

[83] K. S. Il'in, M. Lindgren, M. Currie, A. D. Semenov, G. N. Gol'tsman, R. Sobolewski, S. I. Cherednichenko, and E. M. Gershenzon, "Picosecond hot-electron energy relaxation in NbN superconducting photodetectors," *Applied Physics Letters* **76**, 2752-2754 (2000).

[84] Assuming the dielectric constant for sapphire is ~ 10, the time for electromagnetic radiation to travel across the $\sim 5\,\mu$m detector is: $t_{photon} \approx \frac{5\times10^{-6}\,\mathrm{m}}{3\times10^{8}\,\frac{\mathrm{m}}{\mathrm{s}}\Big/\sqrt{10}} \approx 5\times10^{-14}\,\mathrm{s}$. Similarly, by calculating the speed of sound in NbN using its Young's modulus ($E \approx 400$GPa) and density ($\rho \approx 9\mathrm{g/cm^3}$), the time for phonons to travel across the $\sim 5\,\mu$m detector is:

$$t_{phonon} \approx \frac{5\times10^{-6}\,\mathrm{m}}{\sqrt{4\times10^{11}\,\frac{\mathrm{kg\cdot m}}{s^2}\Big/9\times10^{3}\,\frac{\mathrm{kg}}{\mathrm{m}^3}}} \approx 7\times10^{-10}\,\mathrm{s}.$$

[85] The software for converting the oscilloscope traces into time-stamps was written by Dr. Bryan Robinson at MIT Lincoln Laboratory.

[86] P. Kok and S. L. Braunstein, "Detection devices in entanglement-based optical state preparation," *Physical Review A* **63,** 033812 (2001).

[87] M. J. Fitch, B. C. Jacobs, T. B. Pittman, and J. D. Franson, "Photon-number resolution using time-multiplexed single-photon detectors," *Physical Review A* **68,** 043814 (2003).

[88] D. Achilles, C. Silberhorn, C. Sliwa, K. Banaszek, and I. A. Walmsley, "Fiber-assisted detection with photon number resolution," *Optics Letters* **28,** 2387-2389 (2003).

[89] L. A. Jiang, E. A. Dauler, and J. T. Chang, "Photon-number-resolving detector with 10-bits of resolution," *Physical Review A* **75,** 062325 (2007).

[90] The software for converting the time stamps into cross-correlation data was written by Dr. Burm Baek at NIST, Boulder.

[91] R. Hanbury Brown, and R. Q. Twiss, "Correlation between Photons in two Coherent Beams of Light," *Nature* **177**, 27-29 (1956).

[92] H. J. Kimble, M. Dagenais, and L. Mandel, "Photon Antibunching in Resonance Fluorescence," *Physical Review Letters* **39**, 691-695 (1977).

[93] R. Loudon, *The Quantum Theory of Light*, 3rd edition, Oxford University Press, Oxford, UK (2000).

[94] F. T. Arecchi, E. Gatti, and A. Sona, "Time distribution of photons from coherent and Gaussian sources," *Physics Letters* **20**, 27-29 (1966).

[95] M. J. Stevens, R. H. Hadfield, R. E. Schwall, S. W. Nam, and R. P. Mirin, "Quantum Dot Single Photon Sources Studied with Superconducting Single Photon Detectors," *IEEE Journal of Selected Topics in Quantum Electronics* **12,** 1255-1268 (2006).

[96] R. H. Hadfield, M. J. Stevens, R. P. Mirin and S. W. Nam, "Single-photon source characterization with infra-red sensitive superconducting single-photon detectors," *Journal of Applied Physics* **101,** 103104 (2007).

[97] A. Korneev, Y. Vachtomin, O. Minaeva, A. Divochiy, K. Smirnov, O. Okunev, G. Gol'tsman, C. Zinoni, N. Chauvin, L. Balet, R. Marsili, D. Bitauld, B. Alloing, L. Li, A. Fiore, L. Lunghi, A. Gerardino, M. Halder, C. Jorel, and H. Zbinden, "Single-Photon Detection System for Quantum Optics Applications," *IEEE Journal of Selected Topics in Quantum Electronics* **13**, 944-951 (2007).

[98] C. Zinoni, B. Alloing, L. H. Li, F. Marsili, A. Fiore, L. Lunghi, A. Gerardino, Yu. B. Vakhtomin, K. V. Smirnov, and G. N. Gol'tsman, "Single photonics at telecom wavelengths using nanowire superconducting detectors," *Applied Physics Letters* **91**, 031106 (2007).

[99] M. J. Stevens, R. H. Hadfield, R. E. Schwall, S. W. Nam, R. P. Mirin, and J. A. Gupta, "Fast lifetime measurements of infrared emitters using a low-jitter superconducting single-photon detector, " *Applied Physics Letters* **89**, 031109 (2006).

[100] P. A. Lemieux and D. J. Durian, "Investigating non-Gaussian scattering processes by using nth-order intensity correlation functions," *Journal of the Optical Society of America A* **16**, 1651-1664 (1999).

[101] The experimental setup and optical sources for measuring intensity correlations were set up by Dr. Martin Stevens at NIST, Boulder.

[102] The simulation of $g^{(3)}(\tau_1, \tau_2)$ for a pseudo-thermal source, including extracting the coherence time of the source from the measurement, was performed by Dr. Martin Stevens at NIST, Boulder.